Performance of a Quadrupole Mass Filter and its Application for Ionization Potential Measurements

by

Gang Wang

Department of Physics McGill University, Montreal February, 1991

A thesis submitted to the Faculty of Graduate Studies and Research in partial fulfillment of the requirements for the degree of Master of Science

ABSTRACT

An experimental set-up consisting of an electron-impact induced ionization chamber, a quadrupole mass filter and an ion detector has been constructed. The operating characteristics of the quadrupole mass filter system have been examined and compared to the theoretical predictions. With a moderate mass resolution of 30, an absolute ion transmission efficiency of about 10% has been obtained. This system has been used to investigate the ionization efficiency of noble gases. Charged species up to He²⁺, Ne⁴⁺, Ar⁶⁺, Kr⁵⁺ and Xe⁷⁺ have been studied. The behavior of the ionization efficiency curve near threshold is analyzed using a power law fitting approach. For the first and second degree ionization processes, the fitting power law coefficients k are found to be close to the charge number of the ions produced, in agreement with the theoretical predictions. The extracted ionization potentials also agree with the accepted values. For the third and higher degree of ionization, the k-values are generally much lower than the theoretical predictions. However, the extracted ionization potentials are still consistent with the accepted values.

RÉSUMÉ

Un montage expérimental comprenant une chambre d'ionisation induite par l'impact d'électrons, un filtre quadrupolaire de masse ainsi qu'un détecteur d'ions fut construit. Les caractéristiques d'opération du filtre quadrupolaire de masse furent étudiées et comparées aux prédictions théoriques. Il a été possible d'obtenir une efficacité absolue de transmission des ions de 10% à partir d'une résolution en masse de 30. L'appareillage a été utilisé pour étudier l'efficacité d'ionisation des gaz rares. Des atomes chargés allant jusqu'à He²⁺, Ne⁴⁺, Ar⁶⁺, Kr⁵⁺, Xe⁷⁺ ont été étudiés. Le comportement de la courbe d'efficacité d'ionisation près du seuil est analysé à l'aide d'un ajustement numérique selon une fonction de puissance. Pour les processus d'ionisation de premier et second ordre, la valeur des coefficients k de l'ajustement numérique s'est révélée être semblable à la charge des ions produits; ce qui est en accord avec les prédictions théoriques. Les valeurs déduites des potentiels d'ionisation sont aussi en accord avec celles présentement acceptées. Pour l'ionisation de troisième ordre et plus, les valeurs de k sont généralement beaucoup plus petites que les prédictions théoriques. Cependant, les potentiels d'ionisation trouvés sont encore cohérents avec les valeurs acceptées.

ACKNOWLEDGEMENTS

I wish to express my sincere appreciation and thanks to my thesis supervisor, Professor J. K. P. Lee, for his instruction and guidance throughout this work.

My special thanks go to Mr. Steve Kecani and Mr. Leo Nikkinen for their expert technical assistance in the mechanic and electronic construction of the apparatus, and also for their investing time in reading of the manuscript.

I wish to acknowledge Mr. Dave Lunney. His carefully reading of the whole manuscript and his valuable suggestions deserve much appreciation.

I would also like to thank Miss Catherine Moroney for her valuable contributions to the project.

Many thanks are due to Mr. Sylvain Gilbert for his help with the French translation of the abstract.

Finally, I am grateful to the Department of Physics and Professor Jean Barrette for providing financial assistance and the opportunity to participate in the research activities of the Foster Radiation Laboratory.

CONTENTS

ABSTRACT	i
RESUME	ii
ACKNOWLEDGEMENTS	iii
LIST OF FIGURES	vi
LIST OF TABLES	ix
CHAPTER 1: INTRODUCTION	1
CHAPTER 2: THEORY OF THE QUADRUPOLE	
MASS FILTER	3
2.1 The Quadrupole Field	4
2.2 The Equation of Motion	6
2.3 The Stability Diagram	9
2.4 Mass Range, Resolution and Transmission Efficiency	y 11
CHAPTER 3: CONSTRUCTION AND OPERATION (O F
THE EXPERIMENTAL APPARATUS	14
3.1 General Description	14
3.2 Design and Construction	16
3.2.1 Ionization Chamber	16
3.2.2 Quadrupole Mass Filter	18
3.2.3 Ion Detection and Signal Readout	20
3.3 Operation of the Quadrupole Mass Filter	23
3.3.1 Operating with no DC Voltage	23

	3.3.2 Effect of Applying DC Voltage	25
	3.3.3 Effect of RF Voltage Amplitude	31
	3.3.4 Effect of Ion Injection Energy	32
	3.3.5 Estimate of Absolute Transmission Efficiency	35
CHAPTER	4: IONIZATION POTENTIAL MEASUREMEN	TS
	WITH QUADRUPOLE MASS FILTER	38
4.1	Electron Impact Ionization	38
4.2	Experimental Procedure	42
4.3	Results and Discussion	44
	4.3.1 The First Ionization Potential of Helium	44
	4.3.2 The First Ionization Potentials of Other	
	Noble Gases	49
	4.3.3 The Second Ionization Potentials of Noble Gases	56
	4.3.4 The Third and Higher Degrees of Ionization	
	Potentials of Noble Gases	67
CHAPTER	5: SUMMARY AND CONCLUSIONS	81
REFERENC	FS	81

LIST OF FIGURES

2-1.	A quadrupole mass filter with applied voltages	3
2-2.	Electric potential distribution and electrode configuration of an ideal quadrupole mass filter	5
2-3.	Trajectories of ions in the x-z plane and y-z plane	8
2-4.	The Mathieu stability diagram for the mass filter showing the regions of simultaneous stability	10
2-5.	The first stability region normally used in mass filter operation showing iso- β lines for the x and y directions and a typical operating line	3 11
2-6.	Equipotential contours showing how an ideal hyperbolic rod can be well approximated by a cylindrical rod	13
3-1.	Schematic diagram of the quadrupole mass filter system used for the experiment	15
3-2.	Layout of the ionization chamber	17
3-3.	Assembly of the quadrupole mass filter	19
3-4.	Block diagram of the quadrupole field drive electronics and control	21
3-5.	Schematic diagram for the ion detection and measuring system	22
3-6.	Effect of RF frequency on ion transmission	24
3-7.	Family of double peaks for N^{2+} and O^{2+} at different U/V settings	26
3-8.	Resolution and transmission for mass 28 (N^{2+}) shown as functions of the resolution setting U/V	27
3-9.	Stability diagrams for N ²⁺ and O ²⁺ plotted in V-U space	28
3-10.	A mass spectrum of residual gases	29

3-11	. m/e values of transmitted ions versus scanning RF	
	amplitude V	30
3-12	. Mass spectrum for xenon	31
3-13	. Effect of RF voltage V on mass resolution and peak transmission	33
3-14	. Effect of the ion injection energy Vz on the peak transmission	34
4-1.	Electron impact ionization efficiency curve for ions of He+	39
4-2.	Ionization efficiency curves near threshold for He ⁺ and He ²⁺	40
4-3.	Linear fitting of the kth roots of the experimental data for He ⁺	45
4-4.	Extracted ionization potential V _i varying with both the length of the fitting range above threshold and the fitting power coefficient k.	46
4-5.	V ₁ varying as functions of the length of the fitting range above	
	threshold for He ⁺	47
	Ionization for the formation of Ne ⁺	50
4-7.	Ionization potential of Ar+ extracted from the linear fit of 1.0th and 1.15th root of the experimental data	52
4-8.	Ionization potential of Kr+ extracted from the linear fit of 1.0th and 1.15th root of the experimental data	52
4-9.	Ionization potential of Xe+ extracted from the linear fit of 1.5th and 1.15th root of the experimental data	53
4-10.	Ionization efficiency curve for Ne ²⁺	58
4-11.	Linear fit of the kth roots of the experimental data for Ne ²⁺	59
4-12.	Extracted ionization potential V _i varying with both the length of the fitting range above threshold and the fitting power law	
4 10	coefficient k	60
4-13.	The best fitting power k and the extracted ionization potential V _i varying as functions of the length of the fitting range above threshold for Ne ²⁺	61
4-14.	Ionization potential of He ²⁺ extracted from the linear fit of 2.0th	J.
	and 2.15th root of the experimental data	62

4-15.	Ionization potential of Ar ²⁺ extracted from the linear fit of 1.95th	
	and 2.15th root of the experimental data	63
4-16.	Ionization potential of Kr2+ extracted from the linear fit of 2.0th	
	and 2.15th root of the experimental data	65
4-17.	Ionization potential of Xe ²⁺ extracted from the linear fit of 2.05th	
	and 2.15th root of the experimental data	65
4-18.	Ionization efficiency curves for Ne3+ and Ne4+	68
4-19.	Ionization potential of Ne3+ and Ne4+ extracted from the linear fit	
	of the kth root of the experimental data	69
4-20.	Ionization efficiency curves for Ar3+, Ar4+, Ar5+ and Ar6+	70
4-21.	Ionization potentials of Ar extracted from the linear fit	
	of the kth root of the experimental data	71
4-22.	Ionization efficiency curves for Kr3+, Kr4+ and Kr5+	73
4-23.	Ionization potentials of Kr extracted from the linear fit	
	of the kth root of the experimental data	74
4-24.	Ionization efficiency curves for Xe ³⁺ , Xe ⁴⁺ , Xe ⁵⁺ and Xe ⁶⁺	75
4-25.	Ionization potentials of Xe extracted from the linear fit	
	of the kth root of the experimental data	77

LIST OF TABLES

4-1.	Threshold power law coefficients and ionization potentials	
	for the single ionization of noble gases	55
4-2.	First few energy levels of doubly ionized noble gases	57
4-3.	Threshold power law coefficients and ionization potentials	
	for the double ionization of noble gases	66
4-4.	Threshold power law coefficients for third and higher degrees of	
	ionization of noble gases	79
4-5.	Third and higher degrees of ionization potentials of noble gases	80

CHAPTER 1

INTRODUCTION

The quadrupole mass filter is a very compact device suitable for many mass-selection applications. The discovery of the strong focusing effect in accelerator physics in the early 1950s was embryonic to the birth of the quadrupole mass filter. The use of an electrodynamic quadrupole field was recognized independently by Paul and his colleagues at the University of Bonn [1], and by Post [2] at the University of California Radiation Laboratory in 1953. The promising characteristics of the quadrupole mass filter as a mass analyzer that spurred development were the combination of sensitivity and moderate mass resolution in a compact device, the apparent mechanical simplicity, the light weight because of the absence of a magnet, the linear mass scan manner and the ease of operation. Since the pioneering work of Paul et al., more than thirty years of development in theory, practice and instrumentation have brought the quadrupole mass filter into a stage of widespread applications ([3] - [10] and [23] - [28]). Presently, the quadrupole mass filter is fairly well understood and current developments are mainly in the field of applications.

Although quadrupole mass filters have been commercially available for many years, there are many individualized applications in both science and technology which require the construction of specially designed or modified instruments with particular combination of properties. In this work, a quadrupole mass filter has been designed and constructed. The motivation for it comes from current involvement of the Foster Radiation Laboratory in the study and development of ionization processes applied to laser-desorbed atoms and molecules. In those studies, ionization can be induced either via a group of laser beams through the resonance ionization spectroscopic (RIS) technique, or more directly, via an incident electron beam using the electron-impact reaction. In both cases, ionization takes place in a finite volume element situated between two electrode plates, and the ions thus created can have a substantial energy spread, thereby presents

difficulty in ion mass analysis. In these cases, the quadrupole mass filter is a good choice as a mass spectrometer for its simplicity of construction and operation, its low cost, and in particular, its feature of tolerance of a relatively wide ion energy spread. To test the performance of our quadrupole mass filter, an electron beam has been used to ionized the residual gas in a chamber, the ions produced are injected axially into the quadrupole mass filter. The characteristics of the transmission of the ions through the system is then examined. Finally, the experimental set-up is used to study the threshold behavior of the electron-impact induced ionization of noble gases.

Experimental data concerning the electron-impact ionization of atoms are of great importance in fundamental research in physics and chemistry. The study of the ionization of noble gases via electron impact has proceeded for a long time, however, the behavior of the ionization efficiency curve near the ionization threshold is still not well established. Although some theoretical approaches like the power law model [33]-[40] have been proposed, the experimental data are still not adequate to verify their validity or the conditions for their validity. In the case of multiple ionization of noble gases, the ionization cross-sections are very low, which makes the ionization measurement difficult. Consequently, very few experimental data for high order ionization results have been reported. Despite the numerous papers on the threshold behavior of ionization efficiency, most of the previous studies have been concerned with the investigation of only one or two noble gases and over a limited range of order of ionization. It is therefore difficult to make systematic comparison of the existing results.

Thus, this thesis has two objectives: the first is to design and construct a quadrupole mass filter system, and to examine its operating characteristics; the second objective is to use the quadrupole mass filter system for the measurement of the ionization of noble gases. In Chapter 2, theory based on the Mathieu type equations and some basic considerations of the quadrupole mass filter will be discussed. In Chapter 3, the construction of the quadrupole mass filter system and its performance will be described. Particular attention will be paid to those parameters effecting the mass resolution and ion transmission efficiency. Chapter 4 will focus on the application of this quadrupole mass filter to the ionization potential measurements for the noble gases from helium to xenon. The main emphasis will be laid on the behavior of the ionization curve near the threshold region and the approach to determine the ionization potentials. In Chapter 5, a summary will be given for this work.

CHAPTER 2

THEORY OF THE QUADRUPOLE MASS FILTER

The quadrupole mass filter consists of four parallel rods. The rods opposite one another are electrically connected. Between the two pairs of rods, there is a DC voltage and a superimposed radio-frequency (RF) potential. Figure 2-1 illustrates the configuration of a quadrupole mass filter [15].

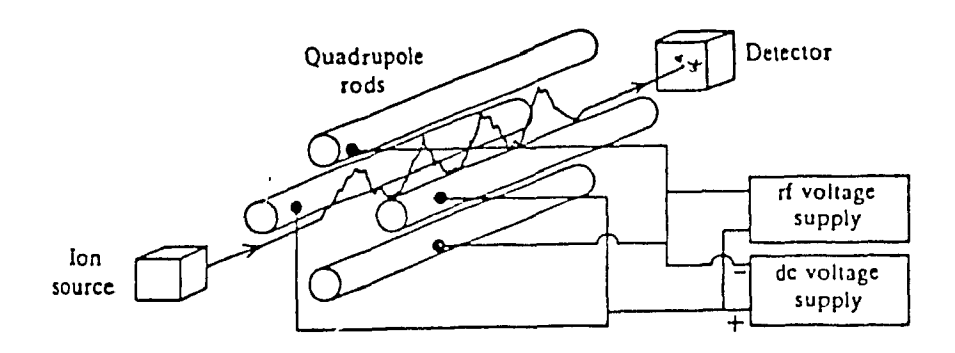


Fig. 2-1. A quadrupole mass filter with applied voltages.

The basic idea of a quadrupole mass filter is to provide an electric field distribution, periodic in time and symmetric with respect to the axis of an ion beam. This field will allow the transmission of ions of a selected mass-to-charge ratio (m/e) range and deflect those of improper ratio from the axis. A brief description of the principles of operation is presented here. Details of the mathematical derivation and discussions can be found in References [10-16].

2.1 THE QUADRUPOLE FIELD

From electrodynamic theory, a quadrupole electric field \vec{E} is expressed by its linear dependence on the coordinate position. In Cartesian coordinates

$$\vec{E} = E_o \left(\lambda x \hat{x} + \sigma y \hat{y} + \gamma z \hat{z} \right)$$
 (2-1)

where λ , σ and γ are weighted constants and E_0 is the scaling factor. Assuming no space charge within the region of interest of the electric field, the application of Laplace's equation

$$\nabla \cdot \vec{E} = 0 \tag{2-2}$$

requires that

$$\lambda + \sigma + \gamma = 0 \tag{2-3}$$

The potential distribution for the mass filter comes from a particular choice of constants in equation (2-3):

$$\lambda = -\sigma; \quad \gamma = 0 \tag{2-4}$$

Other choices for λ , σ , γ yield different configurations, for example,

$$\lambda = \sigma; \quad \gamma = -2\sigma$$
 (2-5)

gives the potential for a quadrupole ion trap. The choices for λ , σ , γ are treated by Dawson ^[10]. For our work, we will concentrate on the quadrupole mass filter, which is deduced from equation (2-4).

With the use of equations (2-1) and (2-4), we can find the potential distribution of the quadrupole field by integrating

$$\vec{\mathbf{E}} = -\nabla \mathbf{\Phi} \tag{2-6}$$

Therefore, we have

$$\Phi = -\frac{1}{2} E_0 \lambda (x^2 - y^2)$$
 (2-7)

The corresponding equipotential lines are shown in Figure 2-2(a). Such potentials are generated by the idealized quadrupole mass filter which consists of four infinitely long hyperbolic cylinders with adjacent electrodes oppositely charged as shown in Figure 2-2(b). If the minimum distance between opposite electrodes is $2r_0$ and the potential difference between adjacent electrodes is Φ_0 , then

$$\lambda = -\frac{1}{r_0^2} \tag{2-8}$$

Therefore, equation (2-7) becomes

$$\Phi = \frac{\Phi_0 (x^2 - y^2)}{2 r_0^2}$$
 (2-9)

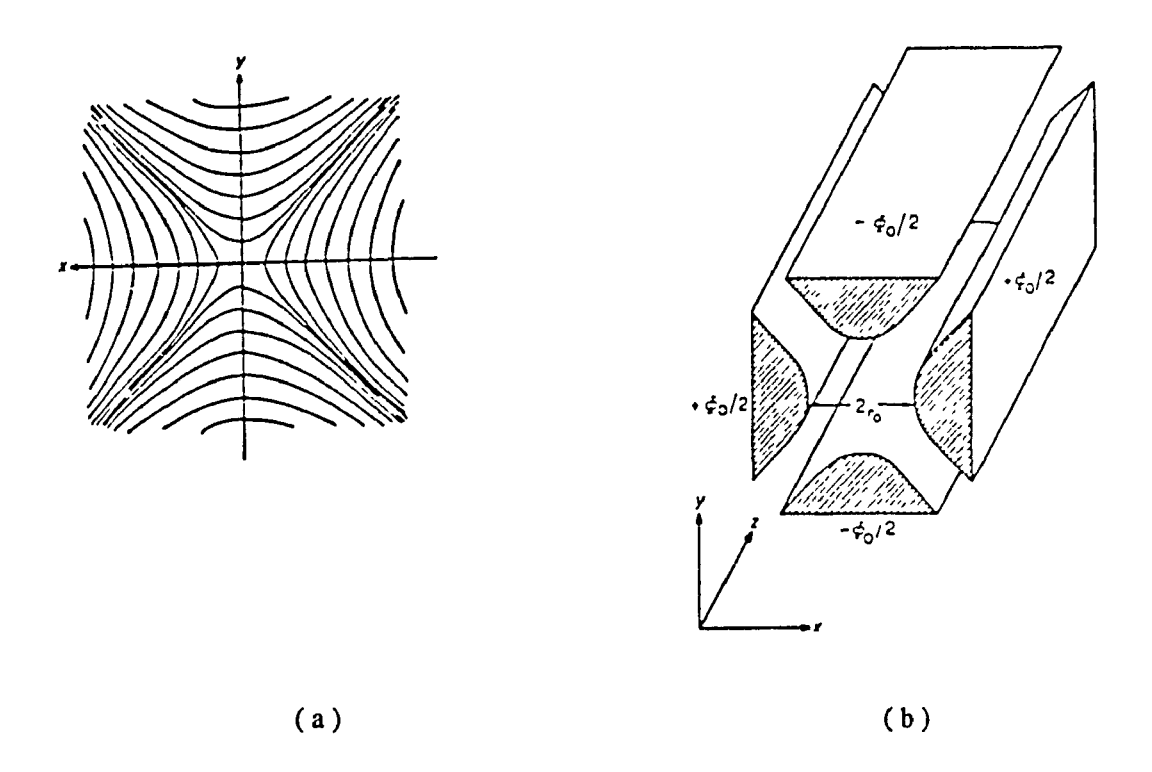


Fig. 2-2. Potential distribution and electrode configuration of an ideal quadrupole mass filter [10]: (a) equipotential lines for a quadrupole field; (b) a hyperbolic electrode configuration which generates the potential shown in (a).

2.2 THE EQUATIONS OF MOTION

In an electric field given by equations (2-1) and (2-4), the equations of motion for a charged particle with mass m and electric charge e can be expressed by:

$$\ddot{x} + (\frac{e}{mr_0^2}) \Phi_0 x = 0$$
 (2-10)

$$\ddot{y} - \left(\frac{e}{mr_0^2}\right) \Phi_0 y = 0 \tag{2-11}$$

and
$$\ddot{z} = 0$$
 (2-12)

When ions are injected into the electric field with a certain velocity in the z direction, the motion of the ions in the x-z and y-z planes will follow equations (2-10) and (2-11). With a positive constant Φ_0 , ions moving along the z axis will always experience a focusing force in the x-z plane and undergo simple harmonic oscillations. However, in the y-z plane the ions will experience a defocusing force and diverge from the z axis. On the other hand, if Φ_0 is chosen to be a periodic function of time, the ion trajectories in both the x-z and y-z planes will be alternately focused and defocused. The ion paths will be stable providing that the transit time of ions in the x and y directions is long compared to the period of the potential, so as to prevent the ions from moving too far away from the z-axis of the mass filter during the defocusing part of the flight. The transit times are, of course, determined by the ion mass.

When a DC potential and a radio-frequency (RF) potential are used , the potential Φ_0 has the form

$$\Phi_{o} = U - V\cos\omega t \tag{2-13}$$

where U is the DC voltage and V the RF amplitude of a sinusoidal voltage with angular frequency ω applied across the pairs of the electrodes. Under the influence of this combination of fields, ions in the quadrupole mass filter undergo complex trajectories ^[10]. For the x direction, the potential established by the DC field alone has some focusing effect toward the z axis in the way of simple harmonic oscillations. The addition of the RF field superimposes a high frequency oscillation. Those ions with lower mass-to-charge ratio are influenced

more by the RF component of Φ_0 and are more likely to strike the x electrodes during their transmission. Therefore, the x direction is the equivalent of a high-pass mass filter. In the y direction, the DC voltage tends to cause some defocusing, but the RF component compensates for this. The paths of heavier ions are unstable due to less correction by the RF potential. Hence, the y direction acts as a low-pass mass filter. By proper selection of the potentials and the frequency, a certain pass-band can be obtained for mass analysis. Typical trajectories in the x-z and y-z plane are sketched in Figure 2-3 [4]. For a given Φ_0 , ions lighter than a particular mass-to-charge ratio tend to have unstable trajectories in the x direction (Figure 2-3(a)), while heavier ions are unstable in the y direction (Figure 2-3(c)). A combination of a low-pass and a high-pass mass filtering enables the selection of ions of a particular charge-to-mass ratio (Figure 2-3(b)).

Now the motion of an ion having a mass-to-charge ratio m/e and moving in the z direction through a quadrupole field can be expressed by the equations

$$\ddot{x} + (\frac{e}{mr_0^2})(U - V \cos \omega t) x = 0$$
 (2-14)

$$\ddot{y} - (\frac{e}{mr_0^2})(U - V \cos \omega t) y = 0$$
 (2-15)

$$\ddot{\mathbf{z}} = \mathbf{0} \tag{2-16}$$

Equations. (2-14) and (2-15) are differential equations of the Mathieu type. By setting

$$\xi = \frac{\omega t}{2} \tag{2-17}$$

and defining

$$a_u = a_x = -a_y = \frac{4eU}{m\omega^2 r_0^2}$$
 (2-18)

$$q_u = q_x = -q_y = \frac{2eV}{m\omega^2 r_o^2}$$
 (2-19)

both equations in x and y have the form

$$\frac{d^2u}{d\xi^2} + (a_u - 2q_u \cos 2\xi) u = 0$$
(2-20)

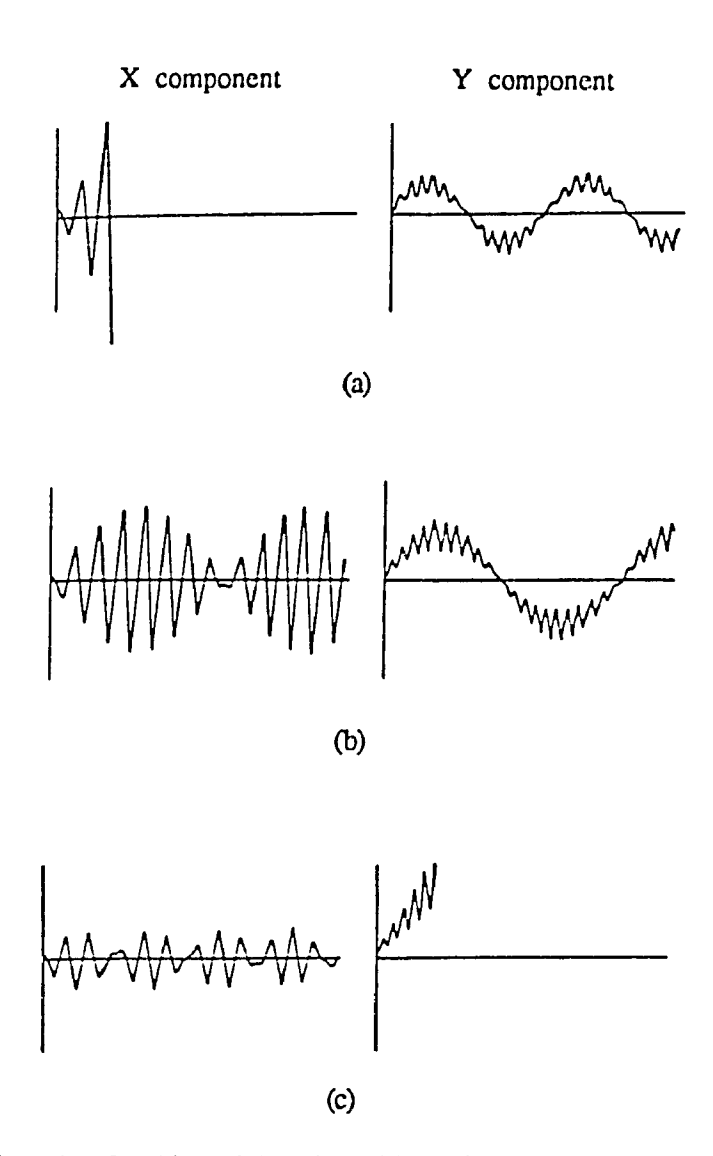


Fig. 2-3. Ions trajectories for (a) a lighter ion, (b) an ion within the mass passing band, and (c) a heavier ion [4].

where u represents either x or y. This is the canonical form of the Mathieu equation. The detailed theory about the Mathieu equations can be found in References [10 - 12].

The general solution to equation (2-20) has finite limits on the range of values of a and q. It is convenient to construct a stability diagram which reveals the range of a and q values that are consistent with the real solution.

2.3 THE STABILITY DIAGRAM

Solutions to equation (2-20) can be expressed as the series expansion

$$u = \alpha_1 e^{\mu \xi} \sum_{n = -\infty}^{\infty} C_{2n} e^{2in\xi} + \alpha_2 e^{-\mu \xi} \sum_{n = -\infty}^{\infty} C_{2n} e^{-2in\xi}$$
(2-21)

where α_1 and α_2 are integration constants which depend on the initial conditions of u, du/d ξ , and the RF phase angle ωt . The constants C_{2n} and μ depend on the values of a and q but not on the initial conditions.

For stable solutions, u remains finite as $\xi \to \infty$. The stability of a particular solution is determined by the form of the exponential parameter μ . Only when μ is purely imaginary, i.e.,

$$\mu = i\beta \tag{2-22}$$

and β is not an integer, the solutions are stable. There are numerous methods for approximating β , and tables of β values for various stability regions can be found in Ref.[17].

Since μ depends only upon a and q, a diagram of stable solutions of the Mathieu equation can be constructed in the a-q plane. Figure 2-4 shows a stability diagram for motion in the x and y dimensions. The coordinates are a and q, which are defined by Equations (2-18) and (2-19). The shaded areas denote stable solutions, and the unshaded areas correspond to unstable solutions. In order for an ion to have a bounded trajectory in the quadrupole field, stable solutions in both x and y must exist. Since $a_x = -a_y$ and $q_x = -q_y$, the x stable region will be the y stable region reflected through the origin. As the stability diagram is symmetrical about the a axis, only positive q values are presented in the figure. The doubly cross-hatched regions correspond to ions with bounded trajectories in both the x and y directions.

The first superimposed stability area near the origin is the normal region of operation of the quadrupole mass filter. Figure 2-5 shows details of mass filter stability diagram of this region. The dashed lines are iso- β_X contours, and the solid lines are iso- β_Y contours. Under normal operating conditions, the parameters

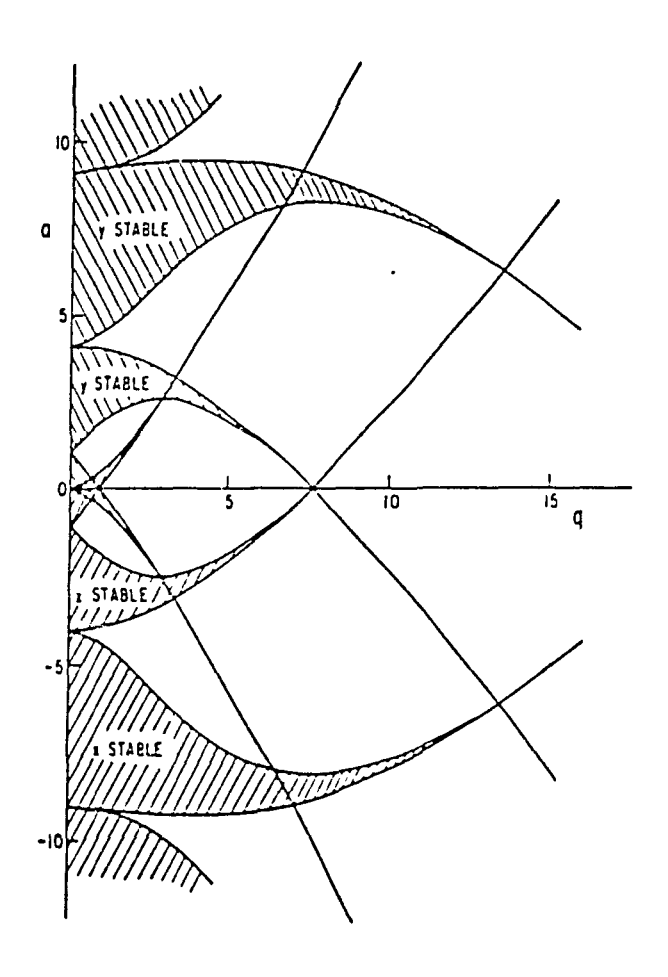


Fig. 2-4. The Mathieu stability diagram for the mass filter showing the regions of simultaneous stability. In the two-dimensional case, stability diagrams for the x and y directions, which differ by the factor -1, are superimposed [3].

 r_0 , ω , U and V all have fixed values. In this case, ions of the same m/e ratio have the same a and q values, and can be represented by the operating point (a, q) in the stability diagram. If the operating point is within the stable zone, the trajectories of these ions lie within the electrodes. Also, From equations (2-18) and (2-19), we have

$$\frac{a}{q} = \frac{2U}{V} \tag{2-23}$$

Therefore, ions with different m/e will lie on the same line of constant a/q, passing through the origin of the stability diagram. This line is also shown in Figure 2-4 and represents the operation of the quadrupole mass filter. Along this operating line, operating points of the heavier ions are situated close to the origin, and those for the lighter ions lie farther away. When $a \neq 0$, i.e., $U \neq 0$, only those ions with operating points lying between the intersections of the operating line with $\beta_y = 0$ and $\beta_x = 1$ will have stable trajectories in both the x and y directions and therefore, will pass through the mass filter. By increasing the U/V ratio, the gradient of the operating line is increased. As the operating line moves closer to the tip of the stability region, only a narrow range of ions will have stable trajectories. The closer the operating line lies to the tip of the stability region, the better the mass resolution will be. The mass spectrum can be scanned by varying the magnitudes of U and V but keeping U/V constant.

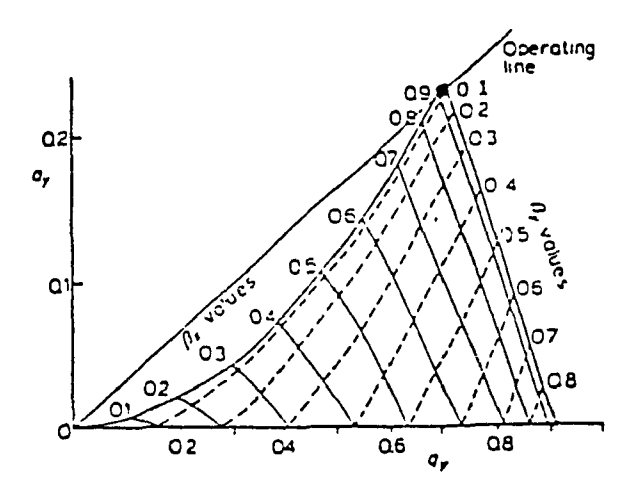


Fig. 2-5. The first stability region normally used in mass filter operation showing iso- β lines for the x and y directions and a typical operating line [10].

2.4 MASS RANGE, RESOLUTION AND ION TRANSMISSION EFFICIENCY

The three important characteristics of a quadrupole mass filter are the mass range, the resolution and the ion transmission efficiency. The maximum mass for

which a quadrupole mass filter can be tuned is dependent upon the positions of the quadrupole rods, maximum available RF voltage and frequency range of the RF supply. According to the stability diagram, when the operating line approaches the stability tip at the point a = 0.237, q = 0.706, the maximum resolution is obtained. Defining the maximum mass M_m as the mass corresponding to the tip of the stability diagram, the following relation can be deduced

$$M_{\rm m} = \frac{7 \times 10^6 \,\mathrm{V}}{\mathrm{f}^2 \,\mathrm{r}_0^2} \tag{2-24}$$

where V is the RF voltage measured in Volts, f the RF frequency in $H_{\text{out}}z$, r_0 the radius of the central axis of the quadrupole field to the surface of the electrodes in meters and M_m the maximum mass measured in atomic mass unit amu.

The resolution of a quadrupole mass filter is related to the time spent by the ions in the focusing field. It is well established that the resolution is governed by the square of the number of RF cycles, and it can be expressed by

$$\frac{M}{\Delta M} = \frac{1}{K} N^2 \tag{2-25}$$

where N is the number of cycles of the RF field to which the ions are exposed, ΔM is the width of the peak at mass M, K is a empirical factor which is about $20^{[10]}$. With the basic operating parameters of the quadrupole length, the RF frequency and the ion injection energy, the number of the RF cycles can easily be determined, and the width of the mass peak can then be expressed by

$$\Delta M = \frac{4 \times 10^9 \, V_z}{f^2 \, L^2} \tag{2-26}$$

where ΔM is the width of the mass peak measured in amu, f the RF frequency in Hertz, L the length of the quadrupole rods in meters and V_z the ion injection energy in eV. Eliminating f by combining Equations (2-24) and (2-26) gives the interrelationship between the mass range and the resolution

$$\frac{M_{\rm m}}{\Delta M} = \frac{L^2 V}{570 V_z r_0^2}$$
 (2-27)

This is the theoretical maximum resolution which does not depend upon the RF frequency.

The ion transmission efficiency is also an important characteristic of a quadrupole mass filter. But the calculation of the ion transmission efficiency is very complicated, and there is no theoretical expression for it. In general, the ion transmission efficiency is dependent upon the mass resolution. At a certain RF frequency, with the increase of the gradient of the operating line, i.e. the increase of the U/V value, the mass resolution will be improved while the ion transmission efficiency reduced. The ion transmission through the quadrupole mass filter requires the ion oscillation amplitudes in both the x direction and the y direction less than r_0 . Therefore, the ion transmission efficiency is also a function of the initial conditions of the position, velocity and RF phase.

In practical designs, cylindrical rods are usually chosen instead of hyperbolic-contoured surfaces because of the ease of machining. However, such imperfections in the quadrupole field will detract from the ideal performance of a mass filter. A detailed comparison between cylindrical and hyperbolic rods has been made by Dawson [10]. His investigation suggests that the cylindrical rod assembly provides well approximated field distributions (as shown in Figure 2-6), provided the radius of the rods r, relative to the value of r_0 is given by $r = 1.148 \ r_0$.

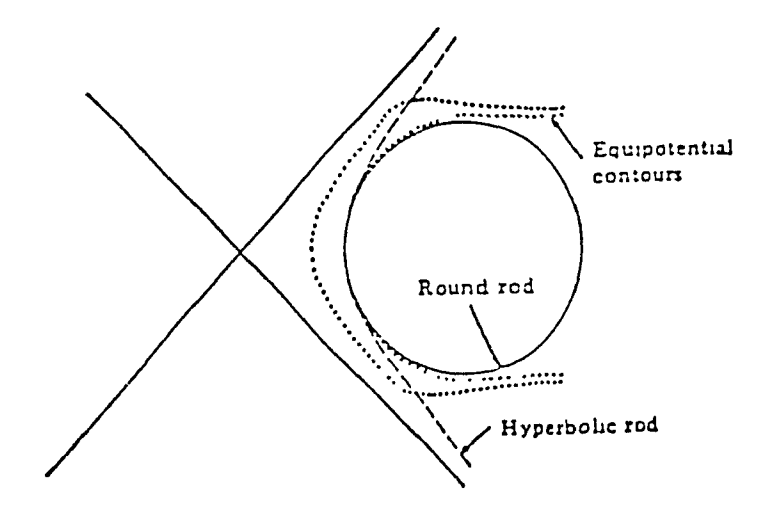


Fig. 2-6. Equipotential contours showing how an ideal hyperbolic rod can be well approximated by a cylindrical rod [10].

CHAPTER 3

CONSTRUCTION AND OPERATION OF THE EXPERIMENTAL APPARATUS

3.1 GENERAL DESCRIPTION

For our experiment, the apparatus schematically shown in Figure 3-1 was designed and constructed. It consists of three major components: the ionization chamber, the quadrupole mass filter and the ion detector. Their main functions are described below.

lonization: Sample gas or vapor molecules inside the ionization chamber are bombarded by electrons from an electron gun and become positively charged ions which are then injected into the mass filter section.

Mass filtering: A quadrupole mass filter system has been constructed for the mass analysis of the injected positive ions. A radio-frequency (RF) potential superimposed onto an electrostatic (DC) voltage is applied to the two pairs of rods. Those injected ions with a specific range of mass-to-charge ratio will have a dynamically stable trajectory within the quadrupole field, while others will be filtered out. By continuously changing the applied voltages, ions with sequential mass-to-charge ratios can then be transmitted through the quadrupole mass filter.

Ion detection: The ions emerging from the mass filter are detected by a channel-plate detector. The output voltage pulses are then amplified and counted. The counting rate is recorded against the scanning RF + DC voltage, thereby producing a spectrum of mass-to-charge ratio peaks, indicating the masses of different kinds of gases inside the ionization chamber.

Fig. 3-1. Schematic diagram of the quadrupole mass filter system used for the experiment.

3.2 DESIGN AND CONSTRUCTION

3.2.1 Ionization Chamber

The ionization chamber is of cubical construction. An electron gun is mounted along the vertical axis above the ionization zone. The electron gun used is a commercial ELG-2, made by Kimball Physics Inc., Wilton, U.S.A. The energy of the electron beam can be adjusted from 10 eV to 1000 eV, with a beam current up to 10⁻⁶ A. The beam energy spread is nominally 0.25 eV. The thermionically emitted electrons from the filament of the gun are accelerated down the ionization chamber and a built-in focusing electrode focuses the beam into the central ionizing region of the chamber. At the bottom of the ionization chamber a Faraday cup with an entrance collimator is used to monitor the electron current. The entrance collimator has a hole 6 mm in diameter, and the electron beam passing through it is stopped by the Faraday cup. During normal operation, the collimator is held at ground potential while the Faraday cup is held at a positive bias of 24 V in order to prevent secondary electrons from leaving the cup surface. A picoammeter (Keithly 614 electrometer) is used to monitor the electron beam current. The collimator can also be in connection with the Faraday cup. In this case, the total electron current hitting both the collimator and the Faraday cup can be measured. In this way, the electron beam alignment can be achieved by maximizing the current ratio of I_f/I_t , where I_f is the electron current collected by the Faraday cup and It is the total electron current collected by both the collimator and the Faraday cup.

Sample gases under investigation are introduced through an adjustable leak valve directly into the ionization chamber where they are bombarded by the electron beam. If sufficient energy is transferred through electron interaction with the sample atoms or molecules inside the ionization chamber, positive ions are formed. With a deflecting plate held at a positive bias and installed on one side of the ionization chamber as shown, the ions created are swept towards the entrance aperture of the mass filter. The injection energy for the ions is controlled by the voltage of the deflecting plate. The voltage is adjustable and normally set at 6 V for reasonable ion transmission and mass resolution.

When the incident electron energy is set below 30 eV, the earth's magnetic field and other induced fields around the ionization chamber can distort the

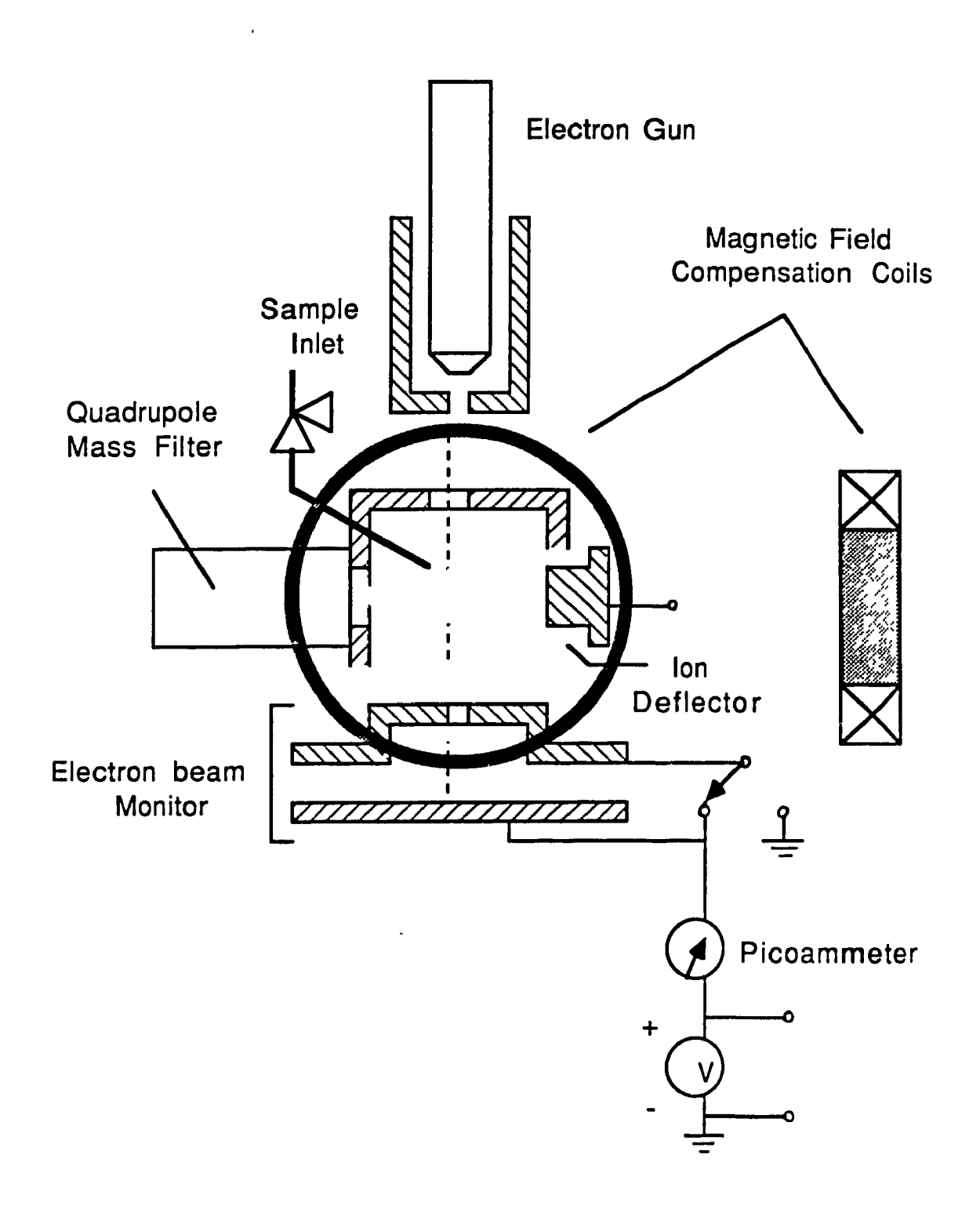


Fig. 3-2. Layout of the ionization chamber.

electron beam significantly from its principal axis, and therefore these stray fields must be eliminated as much as possible. The effect of the induced fields is first minimized by demagnetizing all the ferromagnetic material near the chamber. The remaining residual fields, including the earth's magnetic field, are compensated by mounting two coils with their axes perpendicular to the electron beam direction and also perpendicular to each other. The final resultant net magnetic field is achieved by adjusting the currents through these compensating coils.

When measurements are carried out at an electron energy of less than 15 eV, another effect becomes important. This effect is caused by the accumulation of electric charge on the metallic surface of the ionization chamber. The chamber is constructed of stainless steel and is held at the ground potential. However, after operating the system for a long period of time, the surface of the ionization chamber can be contaminated by a thin film, most likely caused by the vacuum pump oil. In this case, electrostatic charge can accumulate on the surface, and significantly distort the electron beam path. To eliminate this problem, the ionization chamber must be thoroughly cleaned and lightly sprayed with colloidal graphite until a graphite layer on the metal surfaces is formed. After that, stable electron beam can then be maintained at an energy as low as 7 eV over a period of several days of continuous operation.

3.2.2 Quadrupole Mass Filter

The quadrupole mass filter consists of four stainless steel cylindrical rods and two end plates. The rods are held rigidly and precisely at pre-determined positions. The geometrical arrangement of the rod assembly used in the present device is shown in Figure 3-3. The rods are 12.7 mm in diameter and 244 mm in length, with a spacing $(2r_0)$ of 11.1 mm between surface of the opposite rods. This geometrical arrangement satisfies the condition for the cylindrical rods to approximate a field pattern with a hyperbolic cross section, for which the theory was presented in the previous chapter.

The quadrupole rods are placed inside recesses located in the end plates and are held in alignment through the nylon bushings. The end plates also house the entrance and exit collimators, which are 6 mm and 10 mm in diameter respectively. The electron beam passes down the ionization chamber about 20 mm in front of the entrance collimator of the quadrupole mass filter.

As stated in Chapter Two, the mass selection properties of the quadrupole

; }

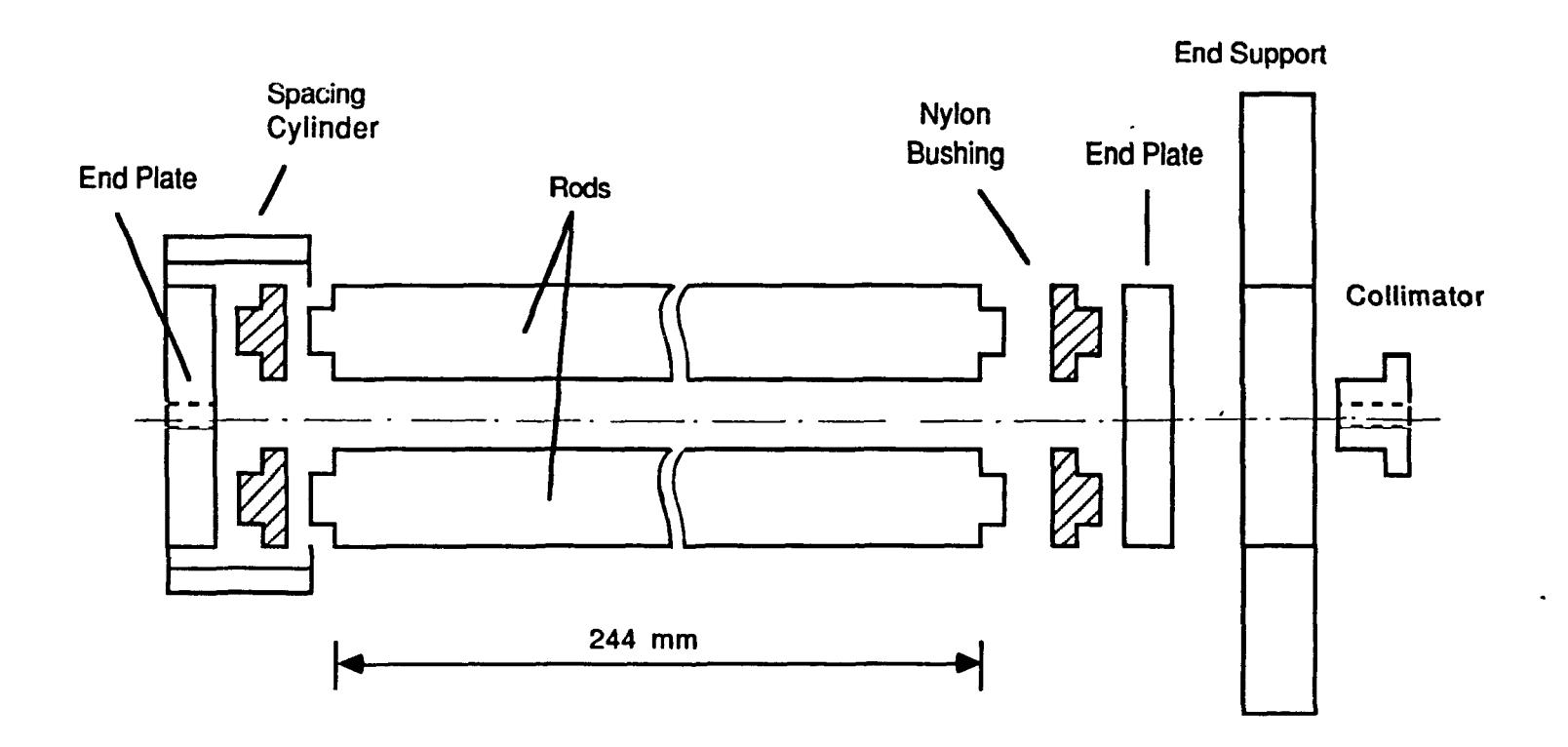


Fig. 3-3. Assembly of the quadrupole mass filter.

field requires the presence of an RF voltage (V cosot) superimposed onto a DC voltage (U) applied to the two pairs of the cylindrical rods. A mass spectrum is obtained by scanning the voltages of U and V while keeping the ratio of U/V constant. We have constructed the circuit that will provide the required voltages U and V cosot. Figure 3-4 represents a block diagram of this control circuit. It is constructed in two parts: a local RF unit which is mounted on the vacuum flange close to the quadrupole rods and a control unit that is located in the instrument rack.

The RF unit receives the signal from the RF power amplifier and steps up its output through an RF voltage transformer (13:1 turns ratio). The output of the transformer is fed to the two pairs of the quadrupole mass filter rods as shown in Figure 3-4. The RF unit also receives the DC bias $\pm U$ from the control unit. These potentials are connected to the rod pairs via the low-pass filters at the RF output terminals of the transformer. At one of the terminals, a capacitive voltage divider of C_1 and C_2 is used to pick up a low amplitude RF signal which is then rectified and filtered. The output is sent to the control unit as a reference of the RF voltage amplitude V.

The control unit is of standard NIM bin construction. Its main function is to generate the appropriate $\pm U$ potentials from the reference signal of the RF amplitude V. This is accomplished by feeding the reference signal to a pair of variable gain operational amplifiers. A small offset voltage δ can be applied to both outputs which then actually have amplitudes of $U + \delta$ and $-U + \delta$. This feature is useful for fine tuning the performance of the quadrupole mass filter. The amplitudes $U + \delta$, $-U + \delta$ and V are digitally displayed on the panel of the control unit.

3.2.3 Ion Detection and Signal Readout

The ion detector used is a multi-channel plate of 25 mm active diameter (type MCP B-25, Galileo Electro-Optics Corp.), with a negative bias voltage at its entrance surface. Ions emerging from the quadrupole mass filter will be accelerated towards the detector plate. To avoid saturation of ions from a localized area on the detector surface, a deflector plate is positioned to vary the ion bombarding area.

Figure 3-5 shows a schematic diagram of the ion detecting and measuring system. Signals from the channel plate detector are amplified and then fed to a fast discriminator. The logic outputs are monitored by a scaler and a rate-meter.

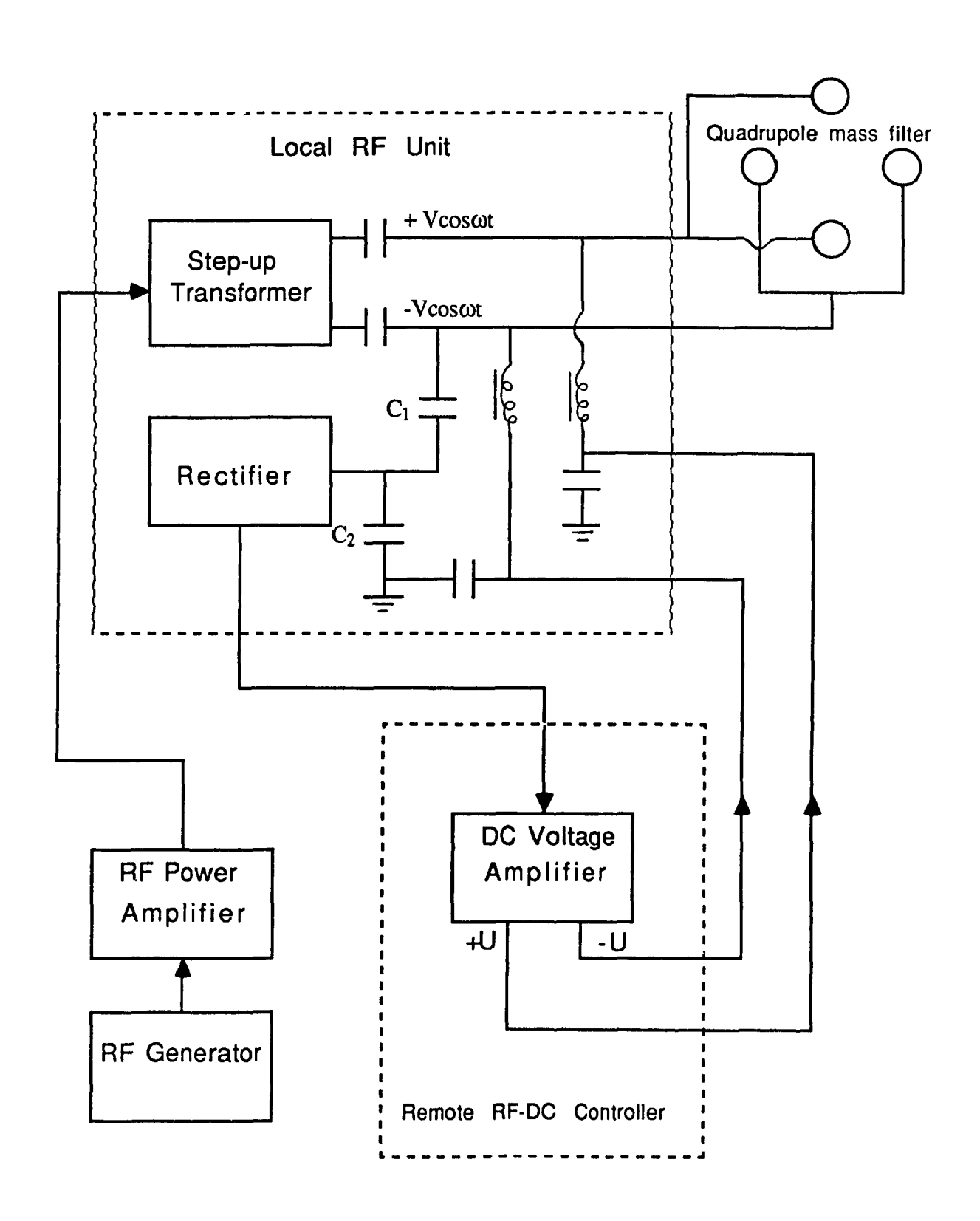


Fig. 3-4. Block diagram of the quadrupole field drive electronics and controls.

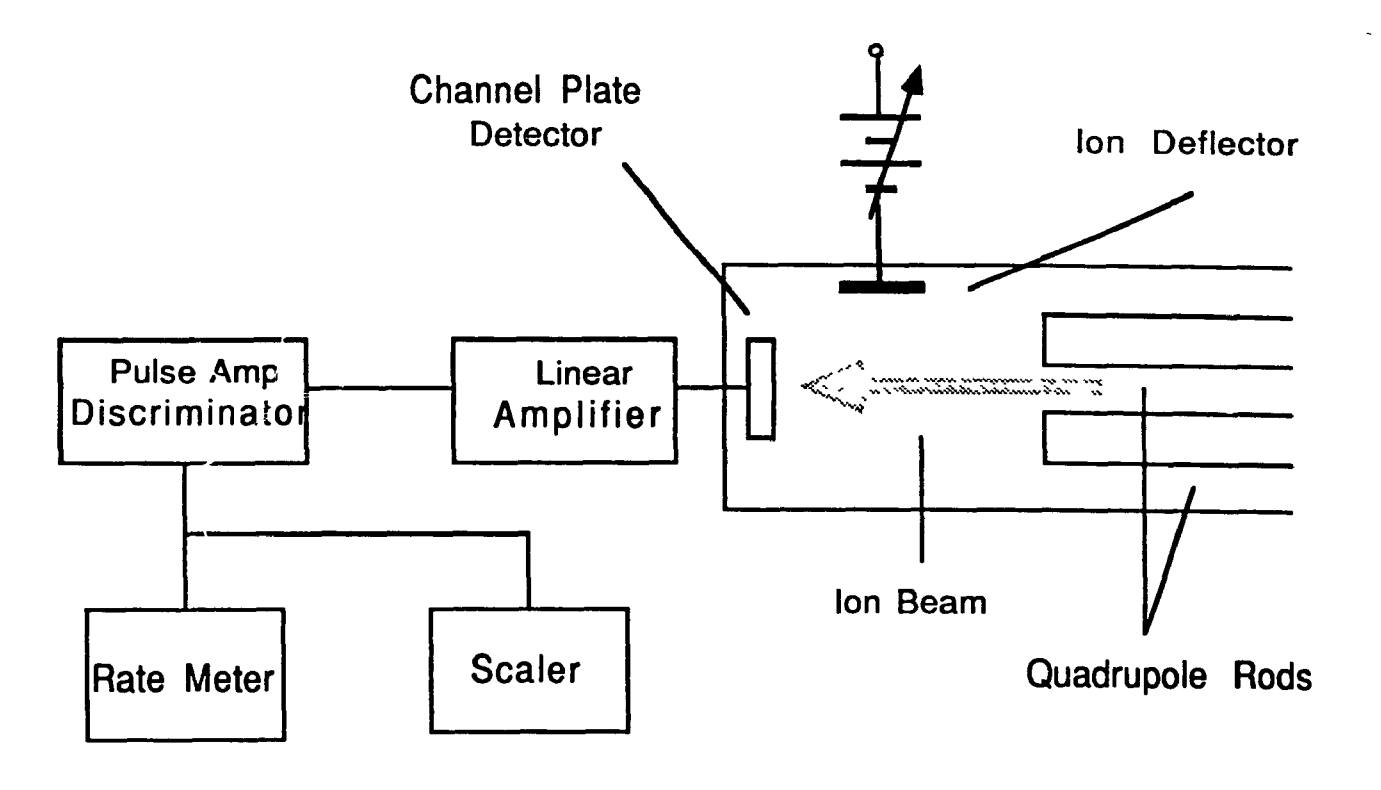


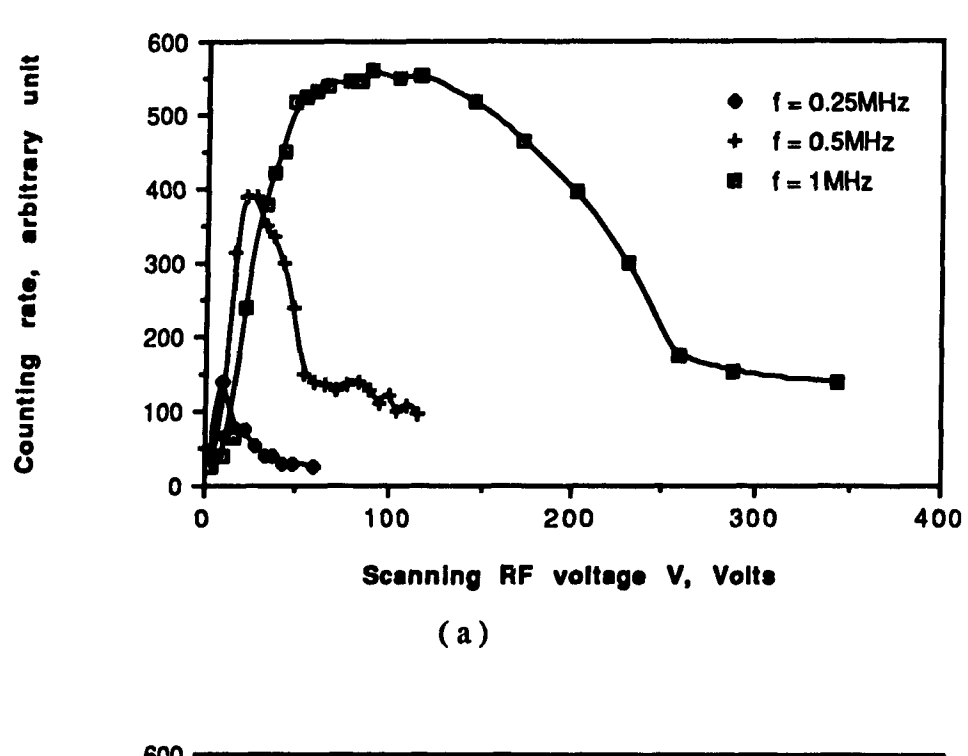
Fig. 3-5. Schematic diagram of the ion detection and measuring System.

3.3 OPERATION OF THE QUADRUPOLE MASS FILTER

3.3.1 Operating with no DC Voltage

Using the quadrupole mass filter system described above, a mass spectrum can be obtained by recording the ion counting rate versus the RF voltage applied to the rods while keeping the DC voltage to RF amplitude ratio U/V constant. The primary adjusting parameters for the mass filter system include the electron energy from the filament, electron beam current, ion injection energy, RF frequency, RF voltage and DC voltage. As mentioned in Chapter 2, if the quadrupole mass filter is operated without any DC voltage (U = 0), ions on the heavy side of the m/e values will be transmitted. Our preliminary transmission test of the quadrupole mass filter is performed using RF voltage scan without any DC component on the electrode rods. These measurements were performed with different RF frequencies in order to observe the effect of the RF frequency on peak transmission.

The measurements were made with the vacuum system containing residual gases at the pressure of 10⁻⁶ torr, a bombarding electron energy of 300 eV, an electron beam current of 10 nA and a deflecting voltage of 10 V. The recorded ion counting rate versus RF voltage (V) is plotted in Figure 3-6 (a) for the RF frequencies (f) of 0.25 MHz, 0.5 MHz and 1 MHz. The plot shows ion transmission characteristics of the quadrupole mass filter when there is no DC voltage on the electrode rods. In the case of 1 MHz RF frequency, when the scanning voltage amplitude V increases, the counting rate increases until it reaches a plateau. Further increase in V results in a decrease in transmission. The initial increase in counting rate corresponds to an increase in the overall ion transmission efficiency. With increasing V, trajectories of ions with progressively higher m/e ratios enter the unstable region and the overall transmission is reduced. However, in the case of ionizing residual gas, there are few low m/e ions. Hence, this effect is not evident at low V. With the given operating parameters, the cut-off voltages for transmitting N₂⁺ and O₂⁺ ions are about 190V and 220V, respectively. When V is increased close to these cut-off voltages, the corresponding counting rates drop quickly. Beyond the cut-off voltages, since no N_2^+ or O_2^+ ions can pass through the mass filter, the counting rate is very low. The curve decreases gradually as V reaches higher mass cut-off points.



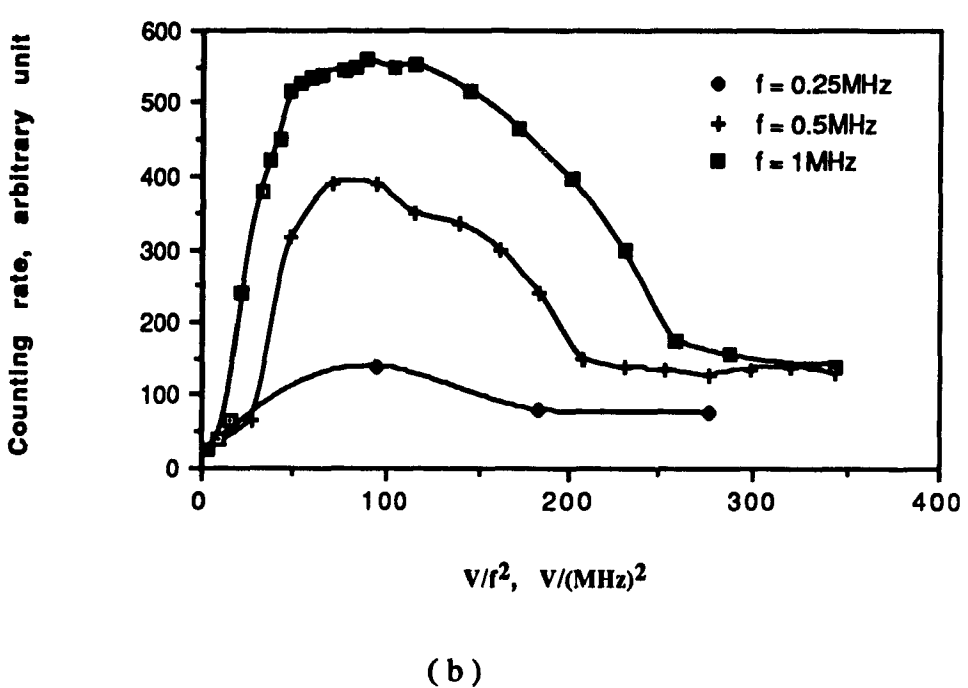


Fig. 3-6. Effect of RF frequency (f) on ion transmission. Counting rate is plotted as a function of (a) scanning RF voltage V, and (b) V/f^2 .

The curves for 0.5 MHz and 0.25 MHz follow the same pattern, but their peak ranges are smaller. In order to make a comparison of the ion transmission for different operating RF frequency in the same ion stability region, i.e. for the same V/f² values [see equation (2-19) in Chapter 2], the transmission curves for frequency 0.5 MHz and 0.25 MHz are normalized to the frequency 1 MHz. V values for 0.5 MHz is multiplied by a factor of 4 and V for 0.25 MHz is multiplied by 16, and three curves are plotted versus V/f² in Figure 3-6 (b). It can be seen that the ion transmission in the quadrupole mass filter improves with increasing the RF frequency. Qualitatively, this effect can be understood as follows. With higher f, higher V is necessary for the same (a, q) operating condition. The higher V means stronger focusing forces on the transverse motion, thereby allowing ions of the same m/e ratio entering the mass filter with higher transverse momentum to be focused. Thus, higher transmission efficiency can be achieved. This increase in V is responsible for the initial increase in counting rate at low V values, and also for the transmission efficiency increase with f for the same operating conditions of (a, q).

3.3.2 Effect of Applying DC Voltage

Our next test is to study the effect of applying a DC voltage (U) on the quadrupole mass filter electrodes. As stated before, the stability of ions transmitted through the quadrupole mass filter is governed by the corresponding operating point on the a-q stability diagram. When U=0, the operating points lie on the q-axis. With a certain U, the (a, q) or (U, V) co-ordinates of a group of m/e values move along the operating line which cuts the stability diagram. In this case, only those ions with operating points lying within the intersected stability diagram will have stable trajectories and pass through the mass filter. With a fixed RF frequency and a certain U/V ratio, the m/e value is basically a linear function of the applied RF voltage (V). A mass spectrum can be obtained by scanning V and the mass resolution can be tuned by varying the DC to RF voltage ratio (U/V).

A measurement to test this prediction is done on the residual gas. The RF frequency is kept constant at 0.5 MHz. The RF amplitude is scanned over the region where N_2 ⁺ and O_2 ⁺ peaks occur. By varying the U/V ratio, a family of four double peaks with different transmission and resolution are obtained. The

results are shown in Figure 3-7. The peaks located at lower V correspond to the ion N_2^+ while the higher peaks correspond to O_2^+ . The four U/V ratio settings 0.135, 0.155, 0.160 and 0.165 yield different heights and widths of the peaks. For each U/V ratio, the mass resolution can be extracted, and the counting rate at the mass peak gives the relative transmission efficiency of the ion. The resolution and transmission for N_2^+ peak as a function of the U/V setting are plotted in Figure 3-8. The initial increase in the U/V ratio causes a slow increase in the ion peak resolution and a gradual decrease in the relative transmission. When U/V is increased further, the resolution increases quickly and the transmission drops correspondingly.

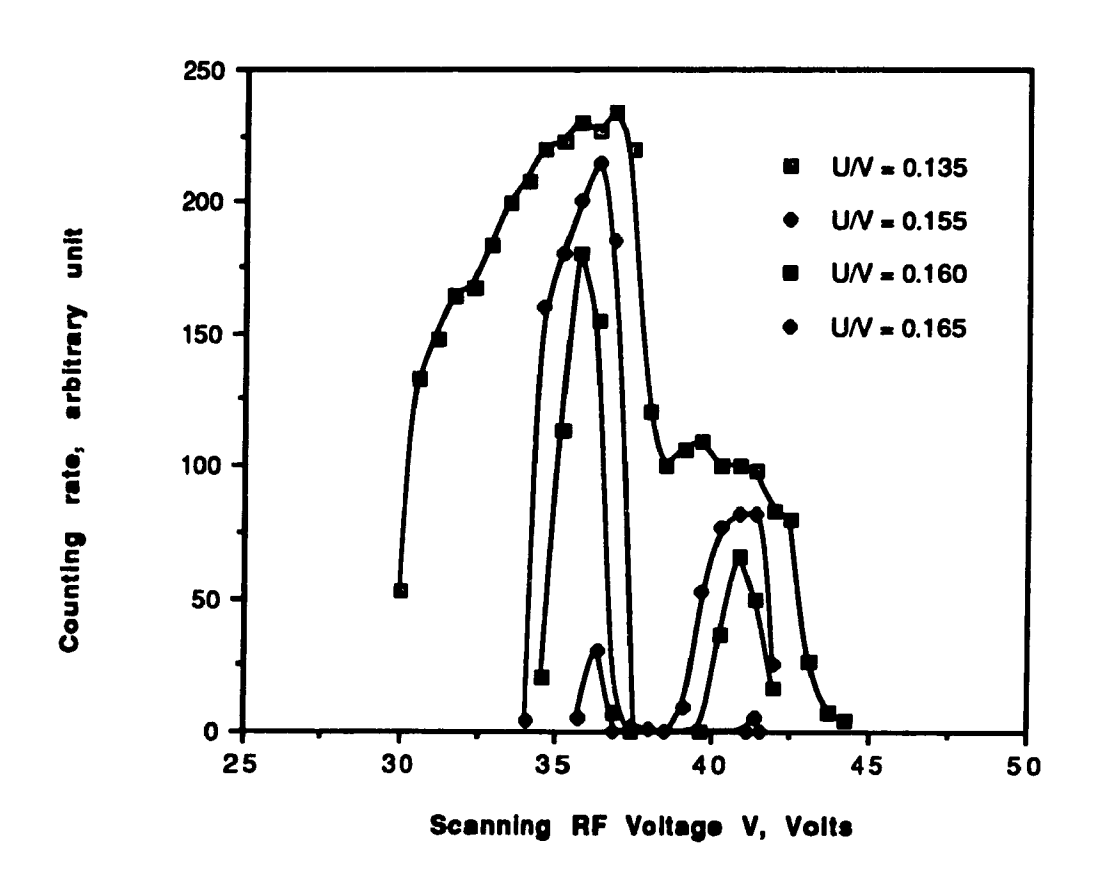


Fig. 3-7. Family of double peaks for N2⁺ and O2⁺ at different U/V settings.

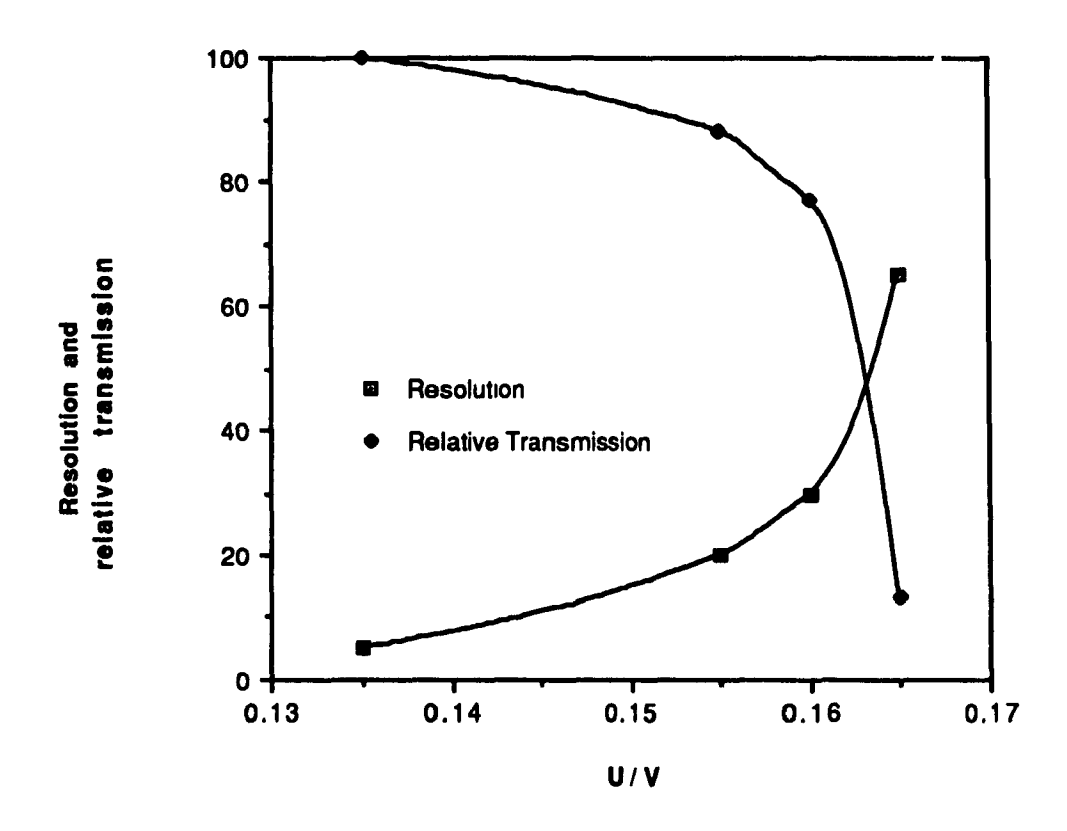


Fig. 3-8. Resolution and transmission for mass 28 (N_2^+) shown as a function of the resolution setting U/V.

The effects of the U/V ratio on the resultant mass resolution can be understood by examining the operating line in the stability diagrams. By observing the cut-off points of the peaks scanned in Figure 3-7, the corresponding boundaries of the stability diagrams have been located and are shown in Figure 3-9. From the quadrupole theory in Ref. [10], the value of the a/q ratio is 0.336 at the tip of the stability region. This theoretical value corresponds to U/V = 0.168 for the solid scan line in Figure 3-9. The experimental operating lines with U/V = 0.135, 0.155, 0.160 and 0.165 are also shown in the figure. The mass resolution, which corresponds to the width of the stable region intersected, can be adjusted by varying the gradient of the operating line, which is determined by the U/V ratio. As U/V is increased to 0.135, two broad maximums which are not well separated begin to show up (Figure 3-7). When the setting of U/V

ratio is increased further to 0.155, 0.160 and 0.165, the mass pass-band of the quadrupole filter is progressively reduced. The ion peaks disappear when U/V reaches 0.170 which is beyond the theoretical limit of 0.168 for the gradient of the operating line. It can be seen that the steeper the gradient of the operating line, the higher the mass resolution, but the lower the ion transmission efficiency. The stability diagrams show that the quadrupole mass filter is working in the predicted manner.

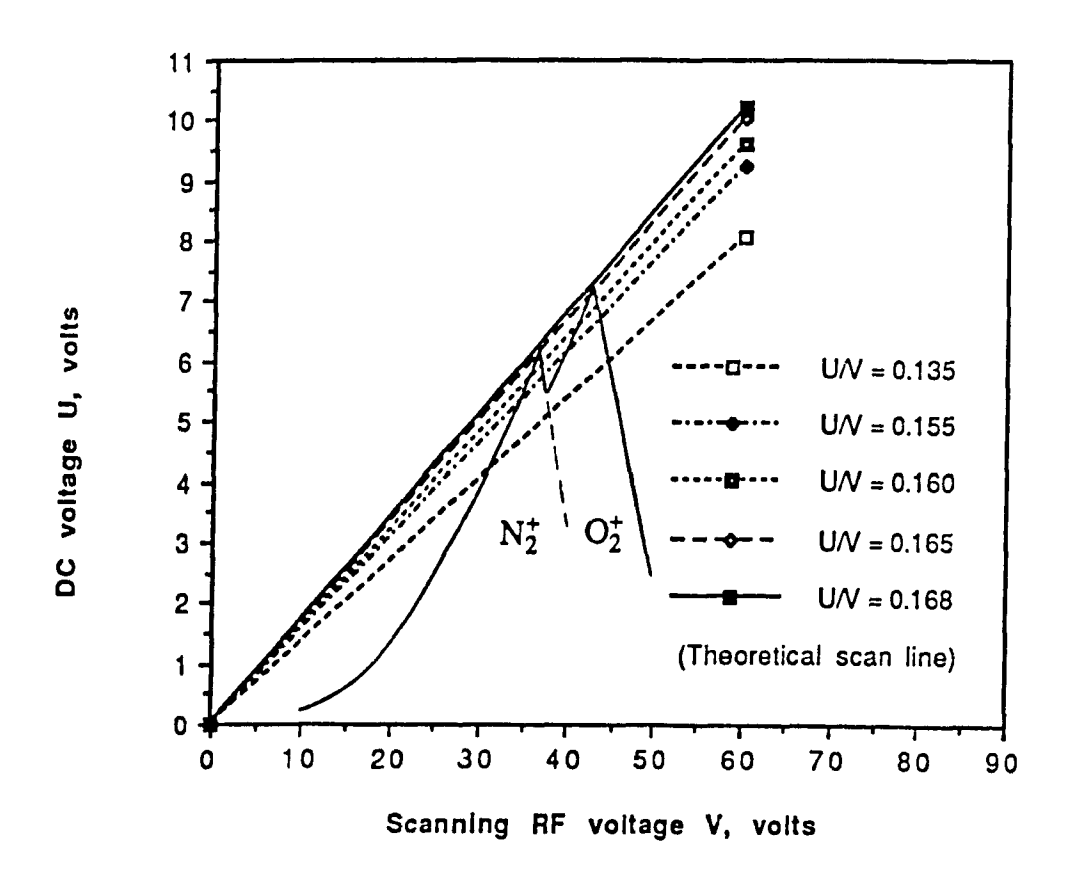


Fig. 3-9. Stability diagrams for N_2^+ and O_2^+ plotted in V-U space.

With the quadrupole mass filter operating line set at a gradient of U/V = 0.160, we have tested the linearity relation of V and m/e at 1.0 MHz. For this measurement, we have added a small amount of neon gas. As the doubly charged Ne^{2+} ion of 20 amu behaves just like the singly charged 10 amu ion in the

quadrupole field, Ne^{2+} and Ne^{+} are two convenient peaks for m/e = 10 and 20 amu. The resultant mass spectrum is shown in Figure 3-10. By varying the residual gas pressure and neon gas partial pressure in the ionization chamber, the relative intensities among the peaks in the spectrum can be changed. In this way, the recorded peaks in the scanning region have been identified as $^{20}Ne^{3+}$, $^{20}Ne^{2+}$, $^{22}Ne^{2+}$, N_2^{2+} and N^+ , O_2^{2+} and O^+ , O_2^{2+} and O_2^{2+} , O_2^{2+}

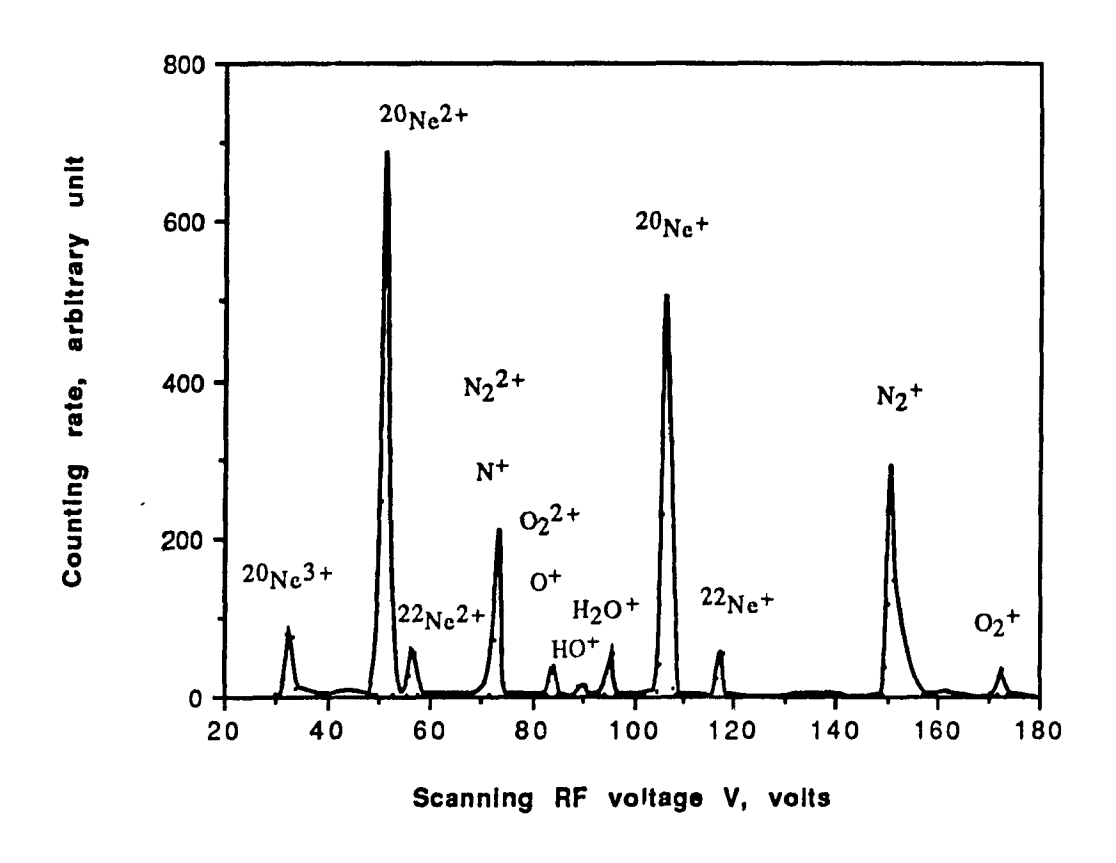


Fig. 3-10. A mass spectrum of residual gases.

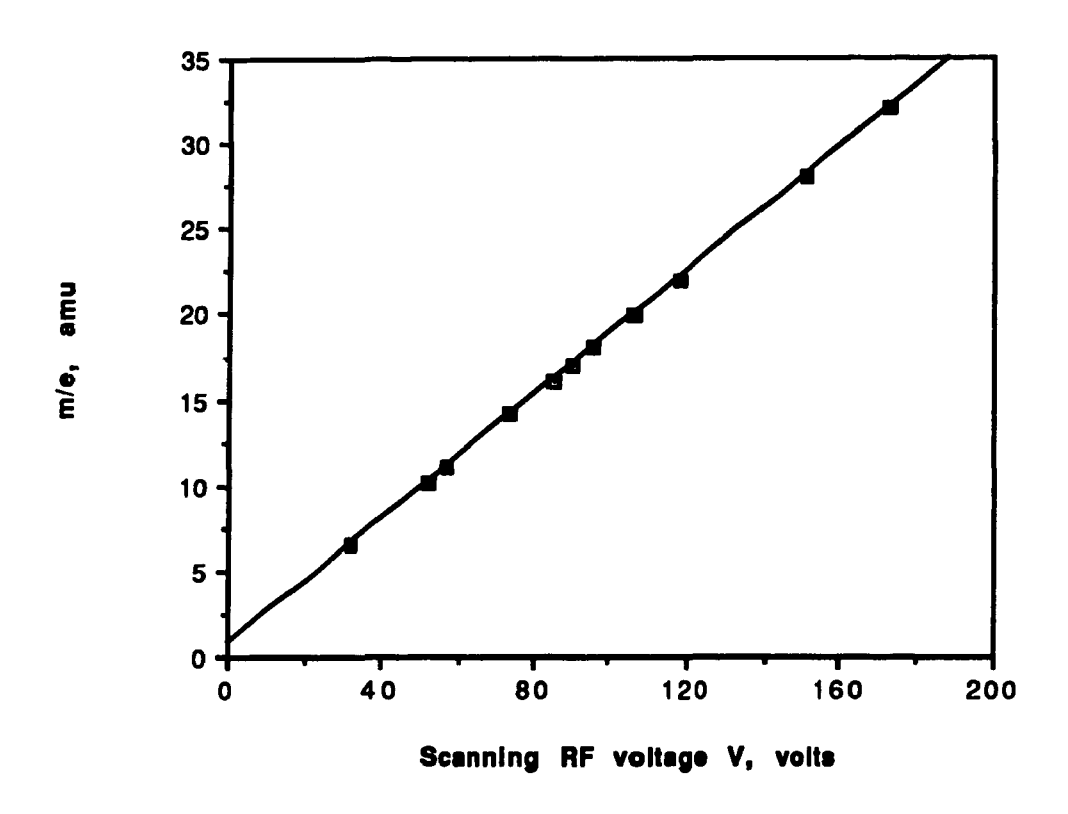


Fig. 11. m/e values of transmitted ions versus the scanning RF amplitude V.

Finally, the resolving power of the quadrupole mass filter was tested with xenon gas. In this case, the RF frequency was kept at 0.6 MHz. The quadrupole mass filter was operated with a U/V ratio approaching 0.168, the theoretical limit. The RF amplitude was scanned around $V \approx 220 \, \text{V}$, which corresponds to the singly charged mass of 132 amu. Figure 3-12 shows the observed mass spectrum for five xenon isotopes. The stable xenon isotope peaks corresponding to the five masses of 129, 131, 132, 134 and 136 have been resolved. The relative peak height is consistent with the isotope abundances in natural xenon. The mass resolution is approximately 130. In principle, the resolution can be further improved by increasing the RF voltage V. Under our experimental conditions: quadrupole length $L = 0.244 \, \text{m}$, $r_0 = 0.00555 \, \text{m}$, ion injection energy $V_z = 3.5 \, \text{eV}$, $V = 220 \, \text{V}$, equation (2-27) gives the theoretical maximum resolution of about 180. Compared to this theoretical resolution limit, our quadrupole mass filter is working reasonably well.

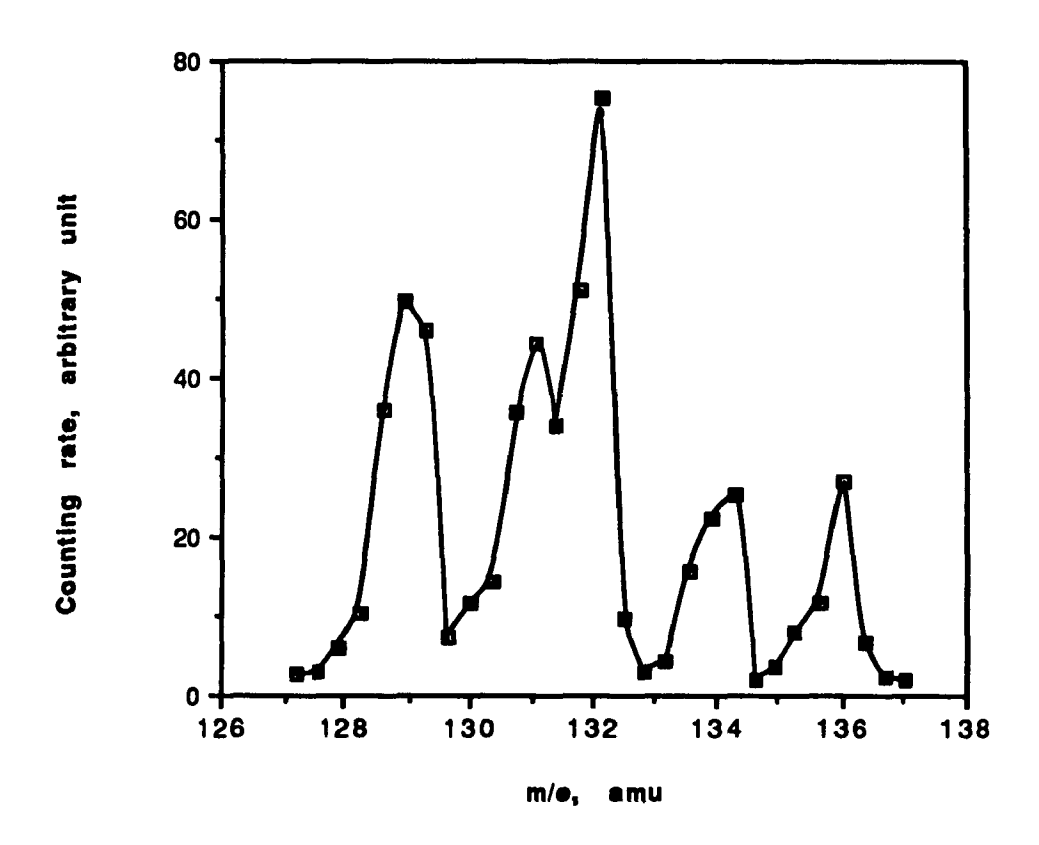


Fig. 3-12. Mass spectrum for xenon. The five stable isotopes of xenon are well resolved.

3.3.3 Effect of RF Voltage Amplitude

The above tests have verified the validity of the a-q stability diagram of the operating conditions of the quadrupole mass filter. However, at any given a-q operating point, it is possible to have different RF frequency f, DC voltage U and RF amplitude V as long as V/f^2 and U/V are kept at fixed values. This characteristic was demonstrated in the case where U=0 (Figure 3-6), corresponding to low resolution condition. It is important that this property is also investigated where moderate mass resolution is achieved.

For this test, argon has been used as the sampling gas. The RF voltage is scanned in the region of the Ar+ peak, and U/V is set at 0.160. By keeping

V/f² constant, the Ar⁺ peak is traced while f is varied from 0.29 MHz to 1 MHz and V from 20 V to 240 V. This test verified the relation of the operating point in the a-q stability diagram and the V/f² value. The resultant mass resolution and peak height of transmitted ions are recorded, which are shown in Figure 3-13.

As seen from Figure 3-13(a), the mass resolution improves when V is increased. The relationship between the mass resolution and V appears to be linear, which also indicates the mass resolution improves proportionally with the square of the RF frequency, for we kept V/f² constant during the test. This result agrees with the theoretical prediction as described by equation (2-27) in Chapter 2. Figure 3-12(b) shows that the counting rate which corresponds to the peak transmission improves with the increase of V. Since V/f² was kept constant, the result can also be interpreted to mean that transmission is improved with the increase of f². This characteristic is consistent with what has been concluded in section 3.3.1 where the quadrupole mass filter was operated without any DC voltage applied on the rods. Therefore, the quadrupole mass filter should be operated at high V and high f values if both good mass resolution and ion transmission are desired. The only limitation in resolution and transmission comes in the capability of the RF system to deliver higher voltage at higher frequency.

3.3.4 Effect of Ion Injection Energy

The resolution of a mass spectrum can be affected by a number of operating parameters, such as the RF frequency, the scanning voltage amplitude, the U/V ratio and the ion injection energy (V_z) . From the results obtained above, for good resolution, the RF frequency, the scanning voltage amplitude and U/V should be tuned high. To investigate the effect of the ion injection energy on the operating characteristics, the amplitude and resolution of the N_2 + peak was examined using different ion injection energies. The results are shown in Figure 3-14, where the mass peaks corresponding to the injection energies of 5 eV and 2.5 eV have been shifted arbitrarily for comparison.

The measurement is taken at a constant RF frequency and U/V ratio. It can be seen that the mass peaks at low ion injection energies (2.5 eV and 5 eV) show a symmetrical distribution. The actual resolution and relative transmission efficiency are not much changed. On the other hand, when an injection energy of

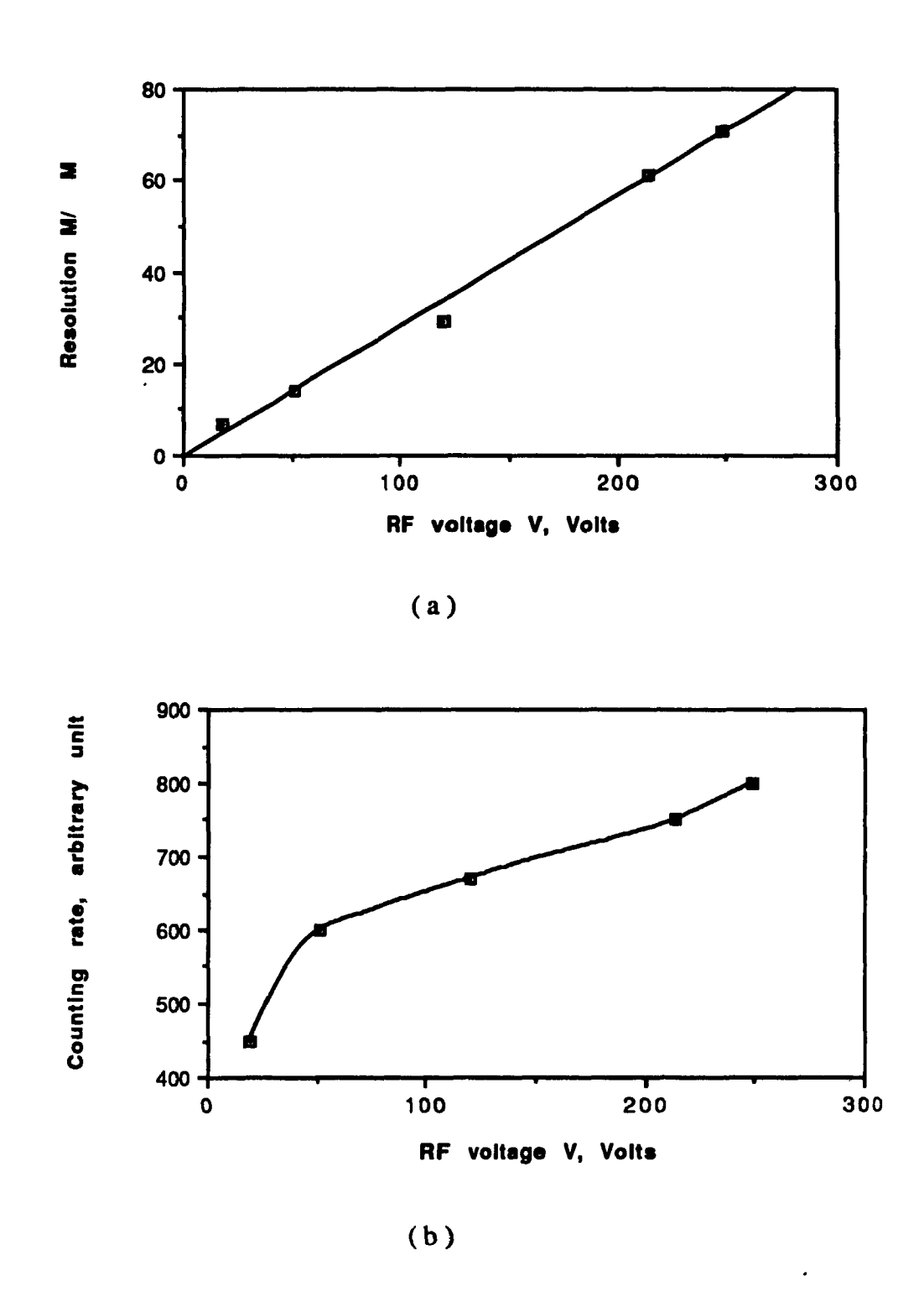


Fig. 3-13. Effect of RF voltage V on (a) mass resolution, and (b) peak transmission.

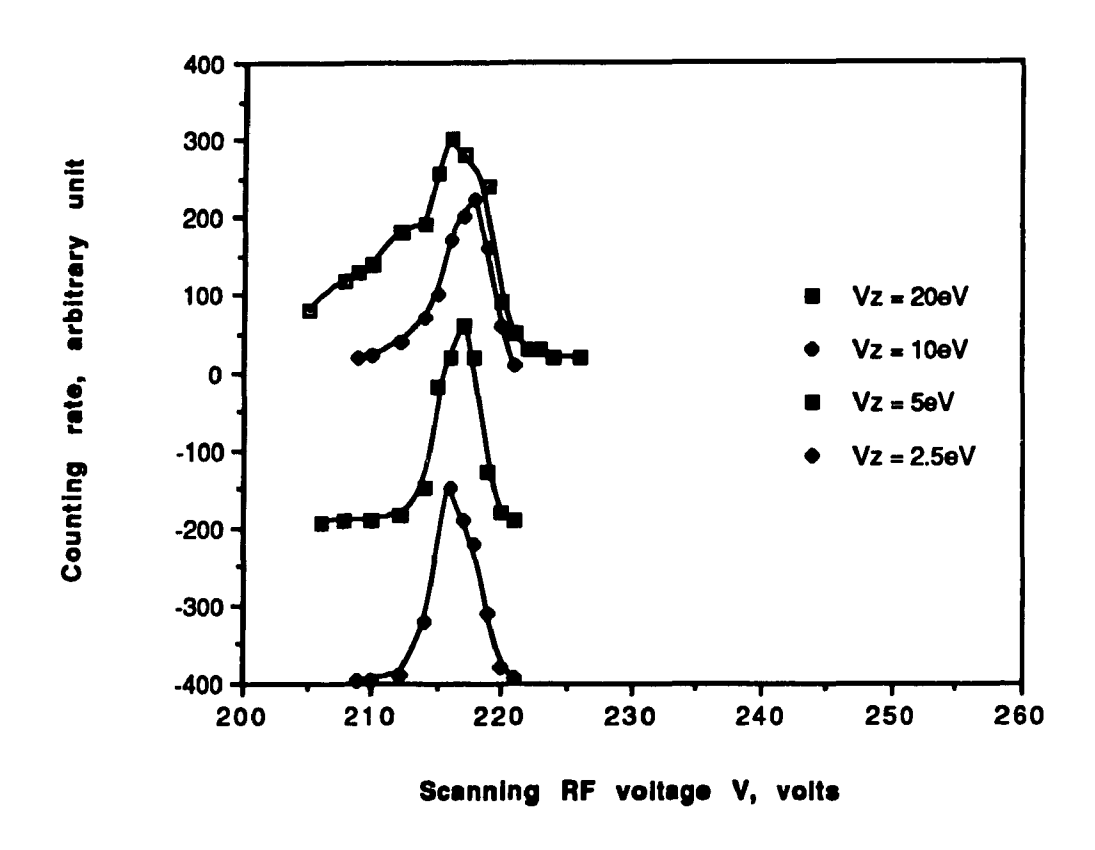


Fig. 3-14. Effect of the ion injection energy Vz on the peak transmission. In this graph the peaks for ion injection energy 5 eV and 2.5 eV have been shifted arbitrarily.

20 eV is used, the peak becomes broader and its amplitude is high. Further decrease of the injection energy reduces the transmission efficiency.

From equation (2-26), the resolution of the quadrupole mass filter is affected by the ion injection energy V_z . In general, the mass resolution is governed by the number of cycles of the RF field to which the ions are exposed. When V_z is low, the transit time for the ions to pass through the quadrupole mass filter will be long and the number of cycles of the RF field that the ions experience will be large. Consequently, more focusing effect is applied to the ions and therefore the mass resolution is improved. With the given dimension of the present quadrupole mass filter, the limit of resolution $M/\Delta M$ is approximately $610/V_z$. At

 $V_z = 20 \text{ eV}$, the best M/ Δ M will then be about 30. For lower V_z , the resolution should increase correspondingly. However, in this test, the operating point is not peaked to the tip of the limit of stability, i.e., U/V < 0.168. Therefore, with lower V_z , the mass resolution actually increases initially, but eventually it is limited by the U/V setting. In the present case, reducing V_z from 10 eV to 2.5 eV doubles the ion transit time, but the relative transmission efficiency and mass resolution attained are the same, indicating good ion optics inside the length of the quadrupole mass filter.

3.3.5 Estimate of Absolute Transmission Efficiency

Finally, it would be of interest to know the actual absolute transmission efficiency of the quadrupole mass filter. As this efficiency depends strongly on the actual operating conditions of a quadrupole mass filter, it is difficult to make comparison among quadrupole mass filters of different design and therefore very few actual numbers have been reported in the literature. However, it will be very interesting to have an estimate on the absolute ion transmission efficiency under a typical operating condition.

We have carried out this estimation using the N_2^+ peak from residual gas. The RF frequency is set at 0.5 MHz, and the U/V ratio 0.160, which leads to a mass resolution of about 30. At the N_2^+ peak location the RF scanning voltage is 36 V. With the residual gas pressure of 1.0×10^{-6} torr, the atomic density in the ionization chamber is

$$\frac{273}{300}$$
 x 78% x $\frac{6.02 \times 10^{23} \text{ molecules}}{2.24 \times 10^4 \text{ cm}^3}$ x $\frac{1}{760}$ x 10^{-6} = 2.5 x 10^{10} N₂ molecules/cm³

(3-1)

The ion injection collimator is a 0.6 cm diameter hole, and we can calculate the effective thickness of the target, which would be 1.5×10^{10} molecule/cm². With an incident electron energy of 300 eV, the ionization cross-section for producing N_2^+ is about 1.1×10^{-16} cm² [20]. Therefore, with an electron beam current of 100 nA in the ionizing zone the ion production rate can be estimated as

$$6.3 \times 10^{11}$$
 (electrons /second) x 1.5 x 10^{10} (molecules /cm²) x 1.1 x 10^{-16} cm²
= 10×10^{5} (ions /second) (3-2)

Ions passing through the quadrupole mass filter are detected by the channel-plate and their total number is estimated in the following manner. Using a terminating resistance of 50Ω , the output pulse for the individual ion has an average height of 2 mV and a width of 20 ns, representing an average charge of about 4×10^{-13} C. This indicates an average gain of 2.5×10^6 for the channel-plate detector, and is consistent with the specification of these detectors.

Under the above mentioned operating condition, a current of 55 nA is collected at the anode of the channel-plate, representing 1.4×10^5 ions/sec reaching the detector. Therefore, the absolute transmission efficiency is estimated to be about 13%.

During the test, the counting rate of the ions is also monitored by direct counting. But, in this case, the rate is very high and dead time correction must be applied. This is carried out by monitoring the counting rate while changing the electron beam current until a linear relation is attained. The ion production rate thus obtained is 1.1×10^5 ions/sec, representing an absolute transmission efficiency of 11%.

It should be stated that the absolute transmission efficiency obtained in this way is quite approximate, and its accuracy could be improved if the residual gas pressure in the chamber is measured by a calibrated gauge. However, in the present system, the absolute transmission efficiency measured includes two other undetermined factors: the injection efficiency of ions into the quadrupole mass filter, and the absolute detection efficiency of the channel-plate detector. Since there is no easy way to isolate these factors, an improved knowledge of the overall efficiency will have little bearing on the performance of the quadrupole mass filter. The overall efficiency of about 10% obtained here compares favorably with that reported in another work [28].

In this chapter, the construction and operation tests of the quadrupole mass filter have been described and good mass resolution and ion transmission efficiency have been achieved. The device has worked very well compared to the theory which is based on a ideal quadrupole field. In particular, the end cap effect, which is caused by the distortion of quadrupole field near the injection and exit ends, seems to be small. Our tests suggest that high operating RF voltage is desirable, and our present electronics should be improved to allow high RF

frequency and voltage operation. It seems that a quadrupole mass filter based on the present design could be adapted for mass selection of the ions produced in a pulsed laser ion source based on resonance ionization spectroscopy (RIS).

CHATPER 4

IONIZATION POTENTIAL MEASUREMENTS WITH THE QUADRUPOLE MASS FILTER

4.1 ELECTRON IMPACT IONIZATON

The quadrupole mass filter system as described in the previous chapters is used for measurements of the electron-impact ionization of noble gases, with particular emphasis placed on the ionization efficiency near the threshold. Studies for the single and multiple ionization processes will be discussed.

The basic process for this electron impact ionization is as follows. An electron beam of known energy passes through the gas being studied. If the kinetic energy of an electron in collision with a neutral gas atom or molecule exceeds the threshold ionization energy of the atom or molecule, ionization can occur; and, in general, a positive ion and two slow electrons will result. Theoretically, the electron impact process can be treated with the technique of classical quantum mechanics. The incident electron approaches the target atom with energy E and interacts with the target electrons through the Coulomb potential. In the partial wave approximation, each free electron with momentum \vec{k} is expressed by an expansion wave-function, $\phi(\vec{k}, \vec{r})$. If the kinetic energy of the impact electron is large enough, an inelastic transition can occur. The free electron is scattered into the energy state E_f and one of the bound target electrons is rejected into the state E_r . In perturbation theory, the matrix element describing this interaction can be determined. Consequently, the ionization cross-section can be deduced.

Experimentally, the ionization potential is determined through the interpretation of ionization efficiency curve near the threshold. An example of an ionization efficiency curve for He⁺, which is taken from our experimental results, is shown

in Figure 4-1. The ionization efficiency is proportional to the ratio of the production rate of the ion to the electron beam current. It is also a function of the ionizing electron energy. The ionization efficiency curve shown in the figure is plotted in arbitrary units.

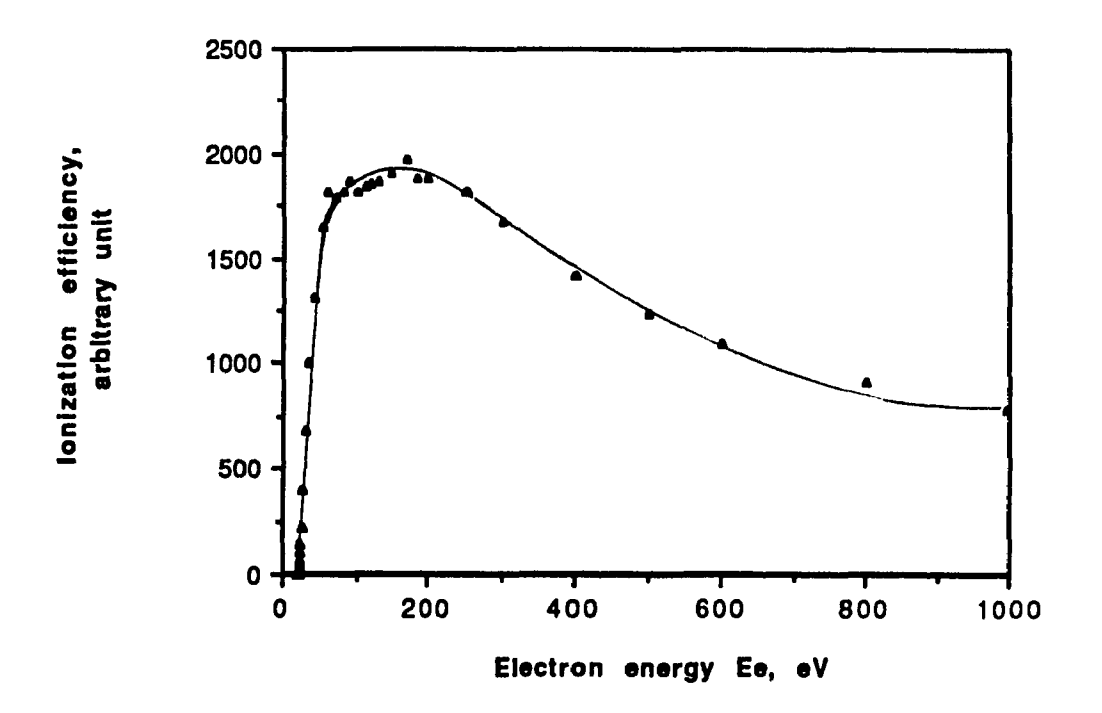


Fig. 4-1. Relative electron-impact ionization efficiency curve for the production of ions of He⁺.

Although the exact form of an ionization efficiency curve depends to a considerable extent upon the element and charge state, the curve generally behaves in the following way: the ionization efficiency increases with the electron energy from zero value at the ionization threshold E_{th} up to a maximum at about 3-5 times of E_{th} , after which it falls off gradually at higher energies. For determining the ionization potentials of noble gases, only the electron energy regions close to the ionization thresholds are of importance. Figure 4-2 shows the expansion of the ionization efficiency curves near threshold for singly and doubly charged ions

of helium.

From these curves it is seen that the threshold behavior is quite different for the two ion species. The ionization efficiency for He⁺ is high, and it almost linearly increases with the electron energy in the region just above the threshold. While for the formation of He²⁺, the ionization efficiency is about two orders of magnitude lower than that for He⁺, and in the threshold region the ionization efficiency curve exhibits a gradually increasing section prior to the steeply rising portion.

In principle, the determination of ionization potential is simply to find the initial break of the ionization efficiency curve from the background. However, this determination becomes quite complicated in practice, particularly in the case of multiple ionization. In the region of the electron energy close to the ionization threshold, the ionization efficiency is very low and the ionization efficiency curve

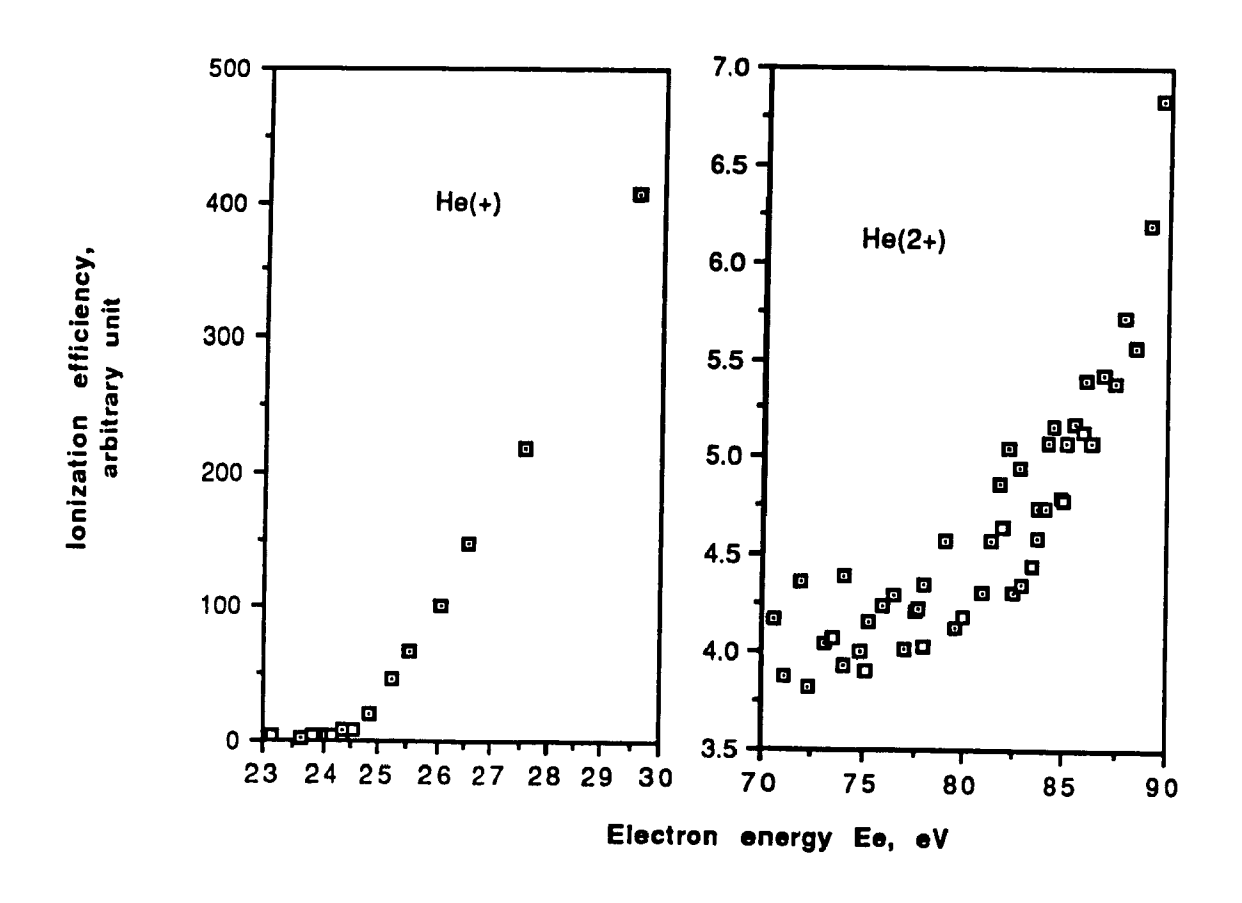


Fig. 4-2. Ionization efficiency curves near threshold for He⁺ and He²⁺.

is approaching the electron energy axis nearly asymptotically, which makes the determination of the threshold energy difficult. For experimentally determining the ionization thresholds a number of extrapolation techniques have been developed.

Almost all the extrapolation techniques are based upon the argument concerning the energy dependence of the electron impact cross-section in the neighboring region above threshold [32]. The earliest and simplest technique used is linear extrapolation. In this method, the ionization efficiency curve close to the threshold is linearly extrapolated back to the zero ionization efficiency. Thus, the intersection on the background is the ionization threshold of the gas under study.

From the theoretical work of E. P. Wigner (1948) [33] and S. Geltman (1956) [34] on cross-sections for multiple ionization, it is concluded that, near threshold, the ionization cross-section σ varies according to the rule $(E_e - E_{th})^k$, where E_e is the impact electron energy, E_{th} the threshold ionization energy and k the degree of ionization. Consequently, this leads to a linear threshold law for single ionization, a quadratic threshold law for double ionization, a cubic law for triple ionization and so on. While there has been widespread development and improvement of ionization models, these models are still based on the above threshold law ([35]-[45]).

From the 1950s to the mid 1960s, the linear threshold law for single ionization was widely accepted. However, for multiple ionization potential measurements most people were still using the linear extrapolation method, in which they fitted the experimental data with two or more intersecting straight lines [22],[47],[48]. Meanwhile, Wannier [35],[36] arrived by a classical phase-space argument at a 1.127 power law:

$$\sigma \sim (E_e - E_{th})^k$$

where the power law coefficient k equals 1.127 for the single ionization process. Wannier's argument was supported by the experimental results of the single ionization of helium from J. W. McGowan in 1968 [52] and P. Marchand in 1969 [45], and it was put on a quantum mechanical basis by A. R. P. Rau in 1971 [51]. Following Wannier's theory, P. Grujic (1982 and 1983) [38] [39] [40] worked on the threshold laws for double and triple ionization. His theoretical work determined the power law coefficient k to be 2.270 and 3.525 for double and triple ionization processes respectively. A recent report was presented

by H. Lebius et al. [44] in 1989. Their experimentally extracted k values are 1.15 and 1.06 for single ionization of helium and neon, 1.97 - 2.14 for double ionization, 2.63 - 3.80 for triple ionization and 2.6 - 4.15 for quadruple ionization for different noble gases from helium to xenon.

In general, most theoretical predictions and experimental results show that the power law coefficient k is approximately equal to the degree of ionization for the case of low-charge-state ionization. Unfortunately, the information about how far above threshold the laws are expected to be valid has not been clearly presented up to now. Furthermore, there are no widely accepted k-values of the threshold power laws that have been reached so far, and in the case of multiple ionization, the information on the threshold extrapolation is still very limited. Therefore, there is definitely a need for further experimental studies on ionization potentials.

4.2 EXPERIMENTAL PROCEDURE

With the quadrupole mass filter system, single and multiple ionizations of all the noble gases by electron impact have been studied. Ionization efficiency curves for the production of the multiply charged ion species up to n=2 for helium, n=4 for neon, n=6 for argon, n=5 for krypton and n=7 for xenon have been obtained. Special attention has been paid to the electron impact energy region near the ionization thresholds and the ionization potentials for all the above ion species have been determined with threshold extrapolation methods.

Most of the measurements are made at a total pressure of about 4×10^{-6} Torr. To ensure adequate purity of the test gas, the background pressure in the system is maintained at about 2×10^{-7} Torr. Spectroscopically pure sample gases are introduced into the system through an adjustable needle valve. By use of the needle valve and the regulator of the gas cylinders, the gas flow rate can be kept constant for a whole day.

The ions produced in the ionization chamber are extracted by a weak electrostatic field (about 6 Volts/2cm), injected into the quadrupole mass filter and selected according to their mass-to-charge ratio. During the experiment, the RF frequency of the quadrupole field is kept constant, usually at about 1 MHz,

and the RF scanning conplitude V is adjusted to stay on the ion peak from the sample gas. By tuning the ratio of U/V, a reasonably good resolution is obtained so as to eliminate tails of the adjacent peaks and to achieve good transmission efficiency as well. The data acquisition is made by scanning the electron impact energy while counting the channel-plate pulses. The bias voltage applied to the channel plate detector was kept at -1650 V throughout the measurements, and the electron gun is usually operated at a current range from 20 nA to 100 nA.

The impact electron energies can be scanned by varying the accelerating voltage on the control unit. The electron beam current passing through the ionization chamber is also monitored for each electron energy setting. The relative ionization efficiency is calculated from the ratio of the ion count rate to the electron beam current. This ratio is then plotted as a function of the energy of the electron beam measured in eV. The ion transmission efficiency for the quadrupole mass filter system depends slightly on the incident electron energy, but within the small energy region near the ionization threshold the ion transmission efficiency can be considered as a constant. The ionization efficiency curves are plotted in arbitrary units.

The data has been fitted with a power law of the form

$$N_0 = B + A (E_e - V_i)^k$$
 (4-1)

where N_0 is the ratio of the ion production rate to the electron beam current, B is the background, A is a proportional constant, E_e is the electron energy ($E_e > V_i$), V_i is the ionization potential, and k is the power law coefficient. Equation (4-1) can also be expressed as

$$N^{1/k} = (N_0 - B)^{1/k} = A(E_e - V_i)$$
 (4-2)

where N is the background subtracted value of the ratio of the ion production rate to the electron beam current. The best fit is obtained by adjusting the coefficient \mathbf{k} and the ionization potential V_i to minimize the least square expression

$$S = \sum_{j=1}^{n} \left[\frac{(N_{j} - N_{j}')}{\sigma_{j}} \right]^{2}$$
 (4-3)

where N_j are the experimental values, N_j are the corresponding values calculated according to equation (4-2), n is the number of experimental points used for the

fitting, and σ_j is the standard deviation at each point N_j . Equation (4-2) shows that the kth root of the ion production rate is a linear function of the impact electron energy.

When the impact electrons are emitted from the hot filament of the electron gun, they may have already possessed some kinetic energy. Therefore, the nominal accelerating energy, i.e. the accelerating voltage reading, could differ from the actual energy of the electron beam. Hence, calibration of the nominal energy scale is necessary. Since the first and second ionization potentials of the noble gases are well known, the electron energy scale is calibrated with these ionization potential values measured in our experiments. In the subsequent discussion, the calibrated electron energies are used.

4.3 RESULTS AND DISCUSSION

4.3.1 The First Ionization Potentials of Helium

As discussed in the previous section, the ionization potentials of the noble gases could be determined by power law fitting of the ionization efficiency curve near the threshold. But how good the power law fitting will be, and what the effects of the fitting range and fitting power on the extrapolation of the ionization potential will be are still unclear. In order to answer these questions, the power law fitting of the ionization efficiency curve of He⁺ near the threshold has been studied in detail. As the ground state of He⁺ is well separated from its nearest excited state by 41 eV, there are no other transitions leading towards excited states on the ionization efficiency curve near the threshold. In addition, with the m/e of 4, He⁺ has little interference from the other background ion species. Hence He⁺ is a suitable ion for our study.

In the first step of this study, we assume certain power law coefficient values (k) and examine the ionization efficiency curve of He $^+$ over a fixed fitting range (about 8 eV) beyond the threshold. The kth roots of the experimental data for the ionization efficiency measured in this region are fitted linearly according to Equation (4-2). By varying k, a group of fitted straight lines have been obtained and they are shown in Figure 4-3 for k = 0.9, 1.0, 1.1, 1.2, 1.3 and 1.4. In this case, the background is low and the statistical uncertainties of the data are

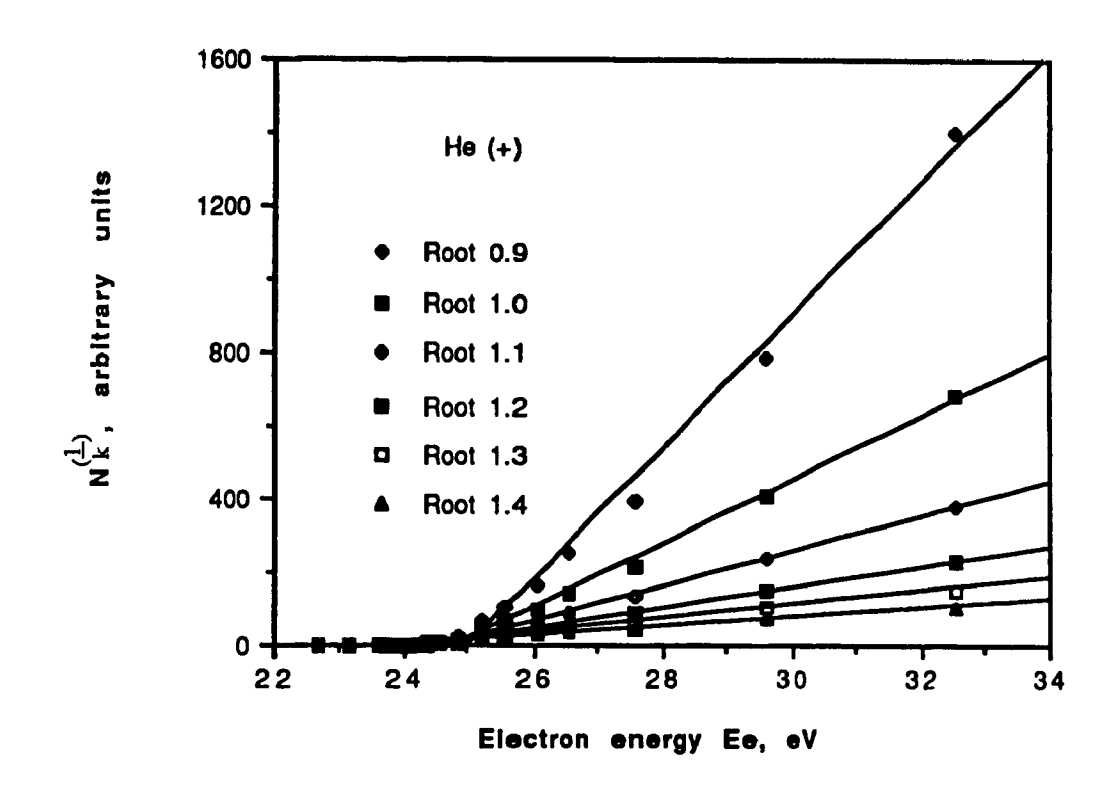


Fig. 4-3. Linear fitting of the kth roots of the experimental data for He^+ , k = 0.9, 1.0, 1.1, 1.2, 1.3 and 1.4.

smaller than the size of the data points in the figure. The ionization potential of He⁺ was obtained by extrapolating the kth root fitting line to the background. The extrapolated ionization potential tends to move towards the lower side when increasing k. The extrapolated ionization potentials vary from 23.9 eV to 24.9 eV for all the k-values used and they are shown in Figure 4-4.

Next we apply the same fitting procedure to different fitting energy ranges above the threshold. For each fitting range, the same group of k-values are assumed and again, a group of extrapolated ionization potentials are obtained. These values are also illustrated in Figure 4-4. The data group obtained over one of the fixed fitting ranges shown in Figure 4-3 have been indicated by two arrows in this figure. From this figure, It can be noted that: (1) when the fitting

range is reduced, the extrapolated ionization potentials with different k converge to about $24.5 \, \text{eV}$; (2) within a fitting range of 8 eV or lower, k values of 1.1 and 1.2 produce nearly constant ionization potentials; (3) although there is an energy spread of about $0.25 \, \text{eV}$ in the impact electron beam, this energy spread does not seem to affect the extrapolation of the ionization potential; and (4) the smaller the fitting range above the threshold, the less k influences on the extrapolated ionization potential. For example, varying k by 0.1 will change the extrapolated ionization potential V_i by about $0.2 \, \text{eV}$ in a fitting range of $8 \, \text{eV}$.

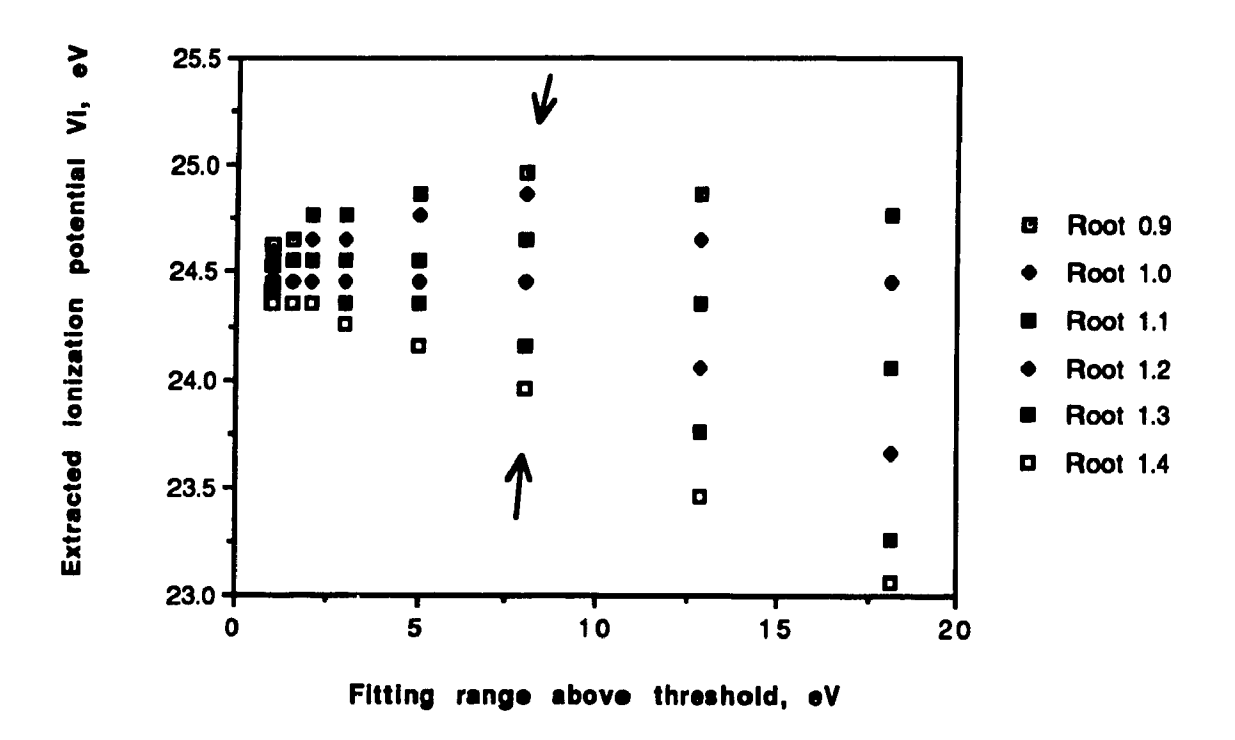


Fig. 4-4. Extracted ionization potential V_i varying with both the length of the fitting range above threshold and the fitting power law coefficient k.

Finally, the data are analyzed using the least square fitting approach by adjusting both the power law coefficient k and the ionization potential V_i . Figure 4-5(a) shows the best fitting power law as a function of the fitting range.

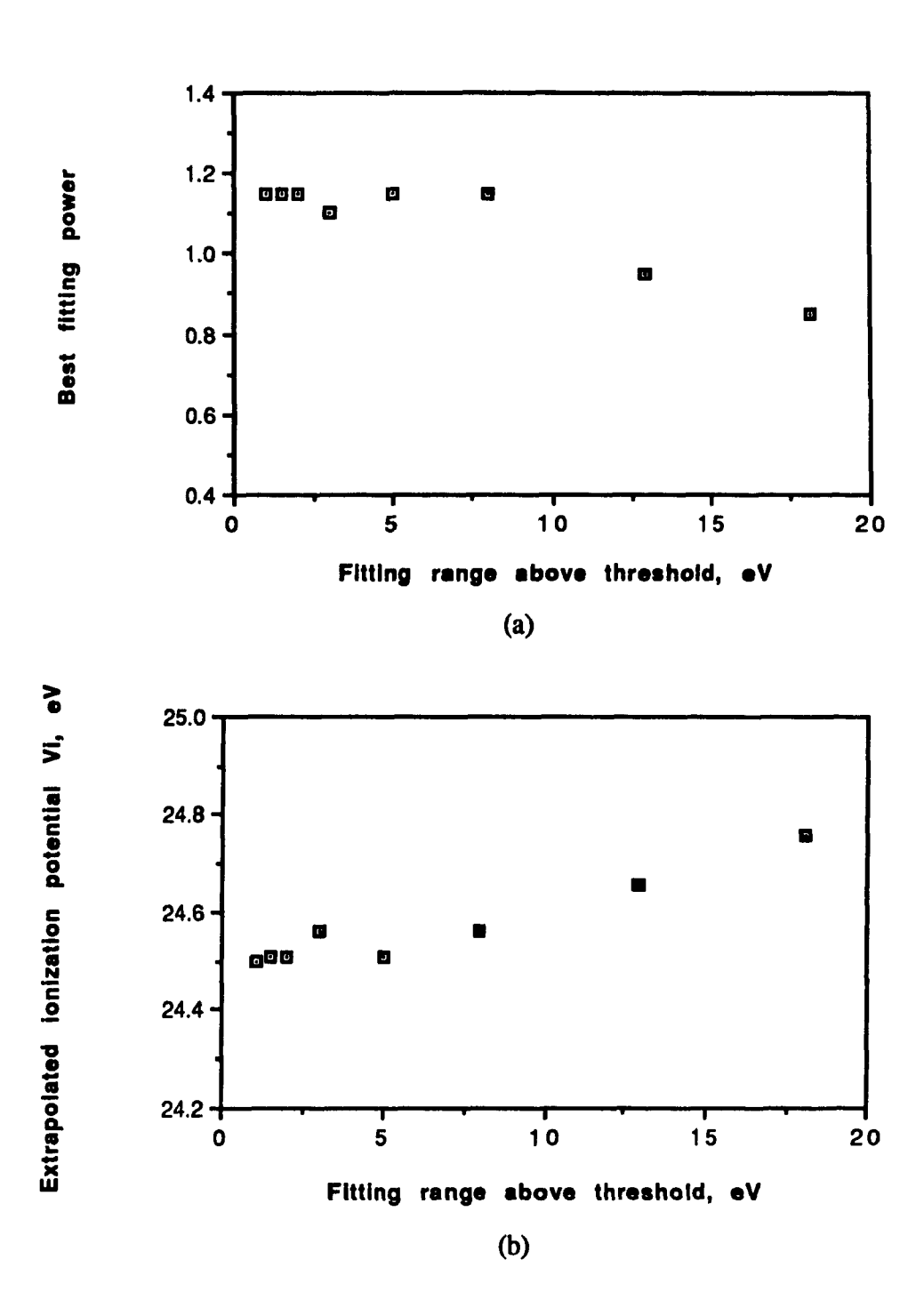


Fig. 4-5. (a) The best fitting power law coefficient k and (b) the extrapolated ionization potential V_i varying as a function of the length of the fitting energy range above threshold for He^+ .

It can be seen that the best fitting power remains approximately constant at 1.15 within the fitting range of 1 - 8 eV beyond the ionization threshold, and it drops with further increase of the fitting range. The best fitting V_i values as a function of the fitting range are shown in Figure 4-5(b). Again within 1 - 8 eV fitting range, the extrapolated V_i remains around 24.5 to 24.6 eV. When the fitting range is increased to 18 eV, a V_i of 24.8 eV is reached, although in this case, k is 0.85 and the fit of the data is obviously quite poor (see Figure 4-3).

It can be concluded that the ionization potential of He⁺ can be determined by the best fitting of the data with a power law. Within a fitting range about 8 eV beyond the threshold, the best fitting power remains at a constant value of 1.15, which leads to a constant extrapolated V_i of about 24.55 eV. Varying k by 0.1 in this fitting range causes a change in V_i of only 0.2 eV. When a smaller fitting range is used, the extracted V_i value is not affected, but its dependence on k is reduced.

Our value of k = 1.15 for the case of He⁺ is close to the theoretical value of 1.127 ^[35]. H. Lebius ^[44] and P. Marchand ^[45] also found a fitting power of 1.15 for the first ionization of helium, but their fitting ranges are much smaller, about 1 eV beyond the threshold. Although the theoretical treatments have not given any information about how far above the threshold the power laws are expected to be valid, our experimental results show that the power law can be fitted in a range as large as about 8 eV for the case of He⁺. It should be mentioned that earlier experiments in the 1950s and 1960s ^{[22],[47],[48]} have reported a linear law for the first ionization potential. Their analyses were carried out over a wider energy range and are consistent with our test results showing that the best fitting power generally decreases with the increase of the fitting range above the threshold.

As described in the previous section (4.2), the extracted V_i values are first expressed as the accelerating voltage of the electron beam and later calibrated with the accepted first and second ionization potentials of the noble gases. The energies expressed here (and the later cases too) are these calibrated ones, and the extracted V_i of 24.55 ± 0.05 eV for He⁺ compares very favorably with the accepted value of 24.58 eV ^[29]. However, this agreement alone has little meaning, and the validity of this power law fitting approach can only be judged by the overall agreement when the power law is applied to the data obtained for other target gases.

4.3.2 The First Ionization Potentials of Other Noble Gases

Neutral atoms of the noble gases Ne, Ar, Kr and Xe all have closed outer s- and p-shells as their ground states. The first ionization process leads to the loss of one electron and the lowest configuration corresponds to the ejection of a p-electron. This leads to a closely spaced doublet of $P_{3/2}$ ground states and an excited state of $P_{1/2}$. The separation of this doublet varies from 0.1 eV for Ne⁺ to 1.3 eV for Xe⁺. The next excited state corresponds to the ejection of the outer s-shell electron and its excitation energies are much higher, varying from 27 eV for Ne⁺ to 11 eV for Xe⁺. In our analysis, we shall apply the least square fitting approach to an energy range of about 10 eV above the threshold, and the ionization processes leading towards both $P_{1/2}$ and $P_{3/2}$ are combined. The analysis is therefore applied to the ionization process for the ejection of a p-electron, which is different from the ionization of He, where a s-electron is ejected. Theoretically, this should not affect the power law coefficient value [20],[35],[38]. For comparison the data are also analyzed assuming k = 1.15, as for helium.

The first ionization of neon is carried out in similar experimental conditions to He⁺. A moderate mass resolution is used to ensure good ion transmission efficiency. The ionization efficiency curve for Ne⁺ is shown in Figure 4-6(a). The general shape of the curve is similar to the that for He⁺ with the normal features of arriving at a maximum and then decreasing monotonously as described in section 4.1. The ionization efficiency near the threshold is analyzed using the same least square fitting procedure as used for He⁺. Figure 4-6(b) shows the resultant fit carried out over a 10 eV range above the threshold, yielding a k of 1.1 and V_i of 21.8 \pm 0.2 eV. The k-value thus obtained is consistent with the value of 1.06 reported by Lebius [44] in 1989, and the extrapolated ionization potential V_i is in good agreement with the spectroscopic value 21.6 eV [29]. In the same diagram, a fit using the same k-value of 1.15 as for He⁺ is also shown. The resultant V_i of 21.7 \pm 0.2 eV is slightly lower than the least square fitted value, which indicates the same dependence of V_i on k as in the case of He⁺. In the case of Ne⁺, the split of $P_{3/2}$ and $P_{1/2}$ is

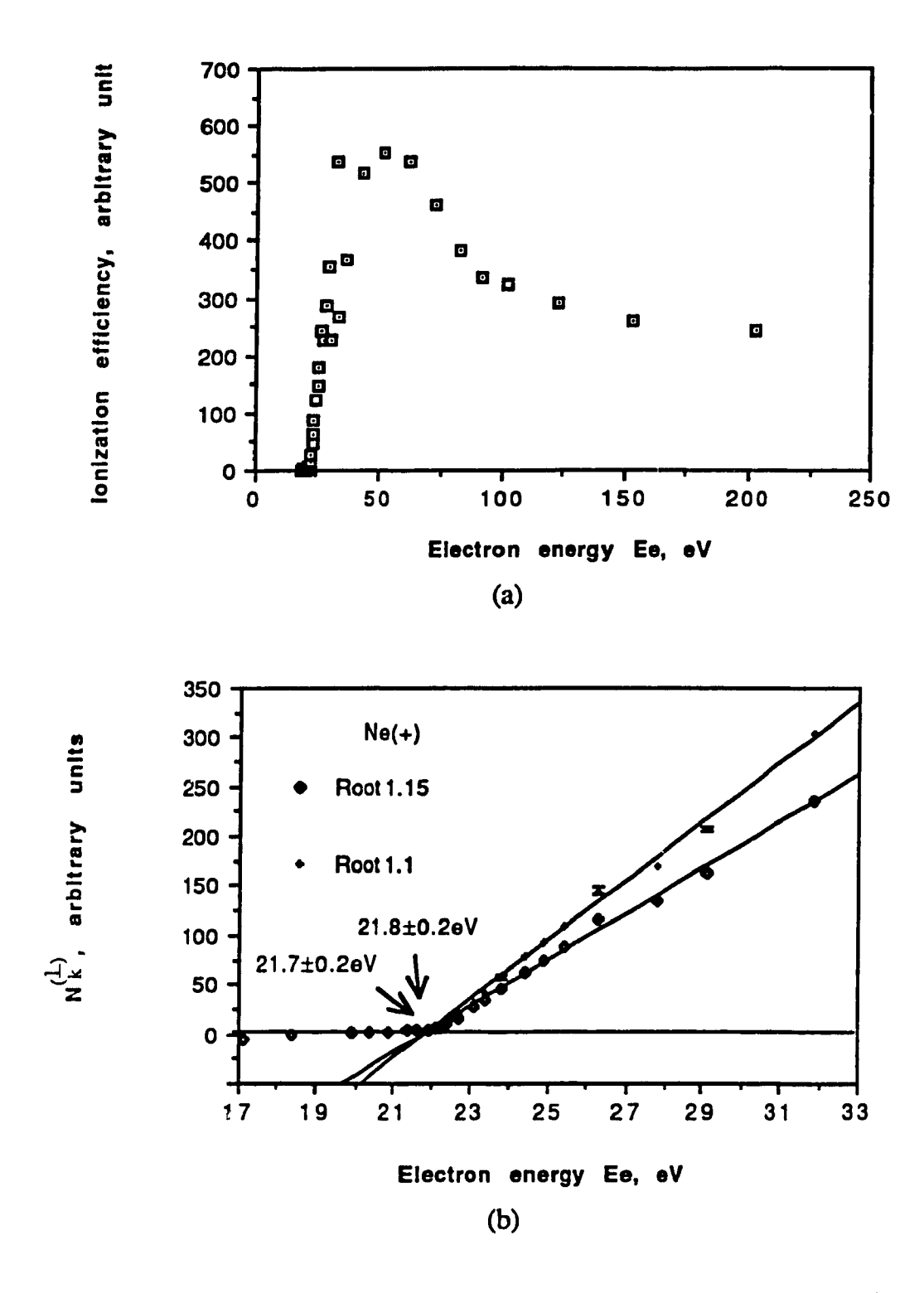


Fig.4-6. Ionization for the formation of Ne⁺; (a) ionization efficiency curve for Ne⁺; (b) ionization potential extrapolated by linear fit of the 1.1th and 1.15th root of the experimental data.

782 cm⁻¹ (about 0.1 eV), and experimentally, it is not possible to separate the two processes. The results of the analysis support the assumption that the ejection of a p-shell electron in the ionization process does not appreciably change the behavior of the ionization efficiency curve near the threshold.

The first excited state $3P_{1/2}$ of Ar⁺ is located at 1432 cm^{-1} (about 0.2 eV) above the $3P_{3/2}$ ground state. The next excited state $3s_{1/2}$ is situated at an excitation energy of 13.4 eV. The same least square fit approach is applied to the data over the first 10 eV range above the threshold, leading to a k of 1.0 and a V_i of 16.0 ± 0.2 eV. Again, as a comparison, when k is fixed at 1.15, a V_i of $15.8 \pm 0.2 \,\mathrm{eV}$ is obtained. Both the fitting lines are shown in Figure 4-7. The V_i values thus obtained are within the uncertainty range and compare well with the accepted ionization potential of 15.8 eV from the spectroscopic data of Ar+ [29]. Earlier work by Marchand [45] in 1969 resulted in a k of 1.3, quite different from the value of 1.0 obtained from the current work. This is particularly puzzling since their work with the first ionization of helium yielded the same k of 1.15 as our result. The difference in the two studies is that in their work k is obtained from the fitting of data over only a 1 eV energy range above the threshold. In the case of He+, there is no excited state within the fitting range at all. While in the case of Ar+, the 3P_{3/2} and 3P_{1/2} levels are situated 0.2 eV apart. The ionization efficiency curve obtained near the threshold would correspond to the sum of the two processes leading towards the two states. Therefore, when the least square fit of the data is performed over a restricted energy range, as in their situation, the energy difference of the two states could affect the resultant k value. In our work, the least square fit is carried out over a much wider energy range, thus reducing the effect due to the small energy split of the $P_{3/2}$ - $P_{1/2}$ doublet.

The least square fitting to the ionization efficiency curve of Kr⁺ is performed over a 10 eV range above the threshold, yielding a k value of 1.0 and a V_i value of 14.1 ± 0.3 eV. The V_i value is in good agreement with the spectroscopic ionization potential of 14.0 eV [29]. For k=1.15, the derived V_i is $13.8 \pm 0.3 \text{ eV}$. Both the fitting lines are shown in Figure 4-8. The spectroscopic analysis of Kr⁺ shows that the $4P_{1/2}$ excited state is located at 5371 cm⁻¹ or 0.7 eV above the $4P_{3/2}$ ground state. Earlier work of the study of the electron-impact ionization efficiency curve near threshold reported the separation of the excitation curves leading to the ground and first excited states [9]. A linear relationship between the ionization efficiency and the excitation energy was observed, and at

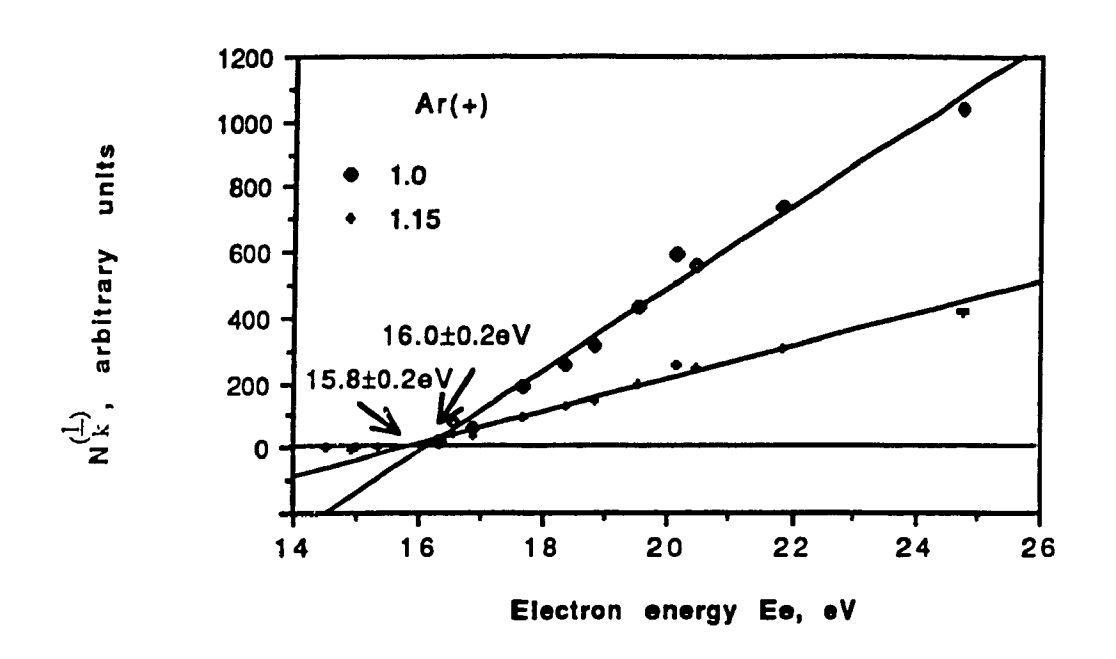


Fig. 4-7. Ionization potential of Ar⁺ extracted from the linear fit of the 1.0th and 1.15th root of the experimental data.

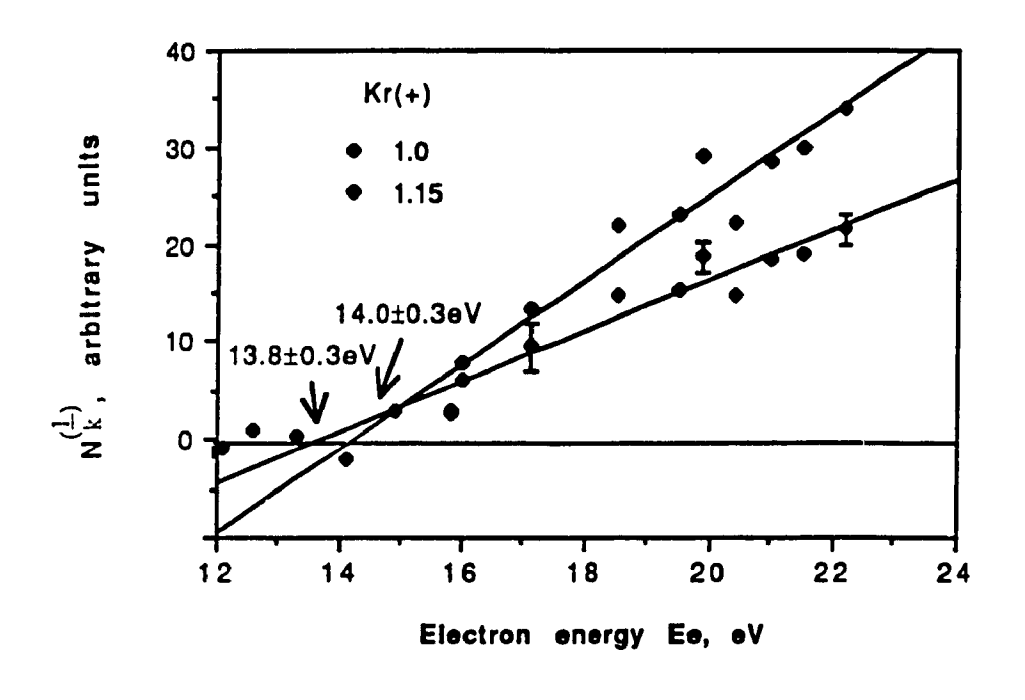


Fig. 4-8. Ionization potential of Kr⁺ extracted from the linear fit of the 1.0th and 1.15th root of the experimental data.

the appropriate excitation energy of $0.7 \, \text{eV}$, a distinctive deviation from the linear fitting was observed, which was attributed to the population of the $P_{1/2}$ excited state. However, this result was disputed as later studies using a similar technique failed to reproduce this break. In the present work, no such break can be inferred from the data. The nominal energy resolution of the electron gun we have used is rated at $0.25 \, \text{eV}$. If one attempts to differentiate the population of the first excited state from the ground state, the energy profile of the electron gun output must first be analyzed, and no such attempt is made in the present work. We have not found any reported experimental k-value in the literature for Kr⁺.

The least square fitting to the ionization efficiency curve of Xe⁺ is carried out over a 10 eV energy range beyond the threshold, leading to a k value of 1.5 and V_i value of 12.0 ± 0.2 eV, which is again in good agreement with the accepted value of 12.1 eV ^[29]. When k is fixed at 1.15, the extracted V_i is 12.9 eV, much higher than the accepted ionization potential. Both the fitting lines are shown in Figure 4-9. In the case of Xe⁺, the $5P_{3/2}$ and $5P_{1/2}$ splitting is

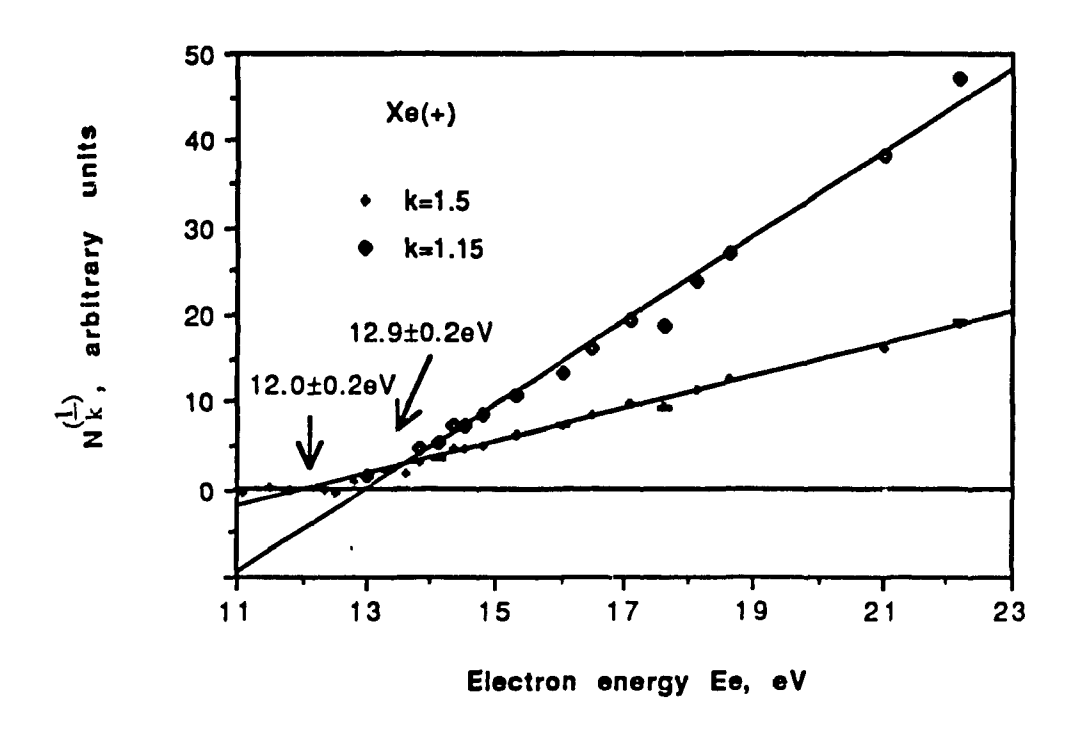


Fig. 4-9. Ionization potential extracted from the linear fit of the 1.5th and 1.15th root of the experimental data.

1.3 eV, and the $5S_{1/2}$ appears at 11 eV excitation energy. Such a large energy separation of the doublet might be the main factor affecting the analysis procedure and thereby yielding a k value much higher than expected.

The analysis of the first ionization efficiency curves of the noble gases is summarized in Table 4-1. Using the least square fitting method, the extracted ionization potentials are all within 0.3 eV of the accepted spectroscopic data. The extracted k values are generally different for different gases, and with the exception of the case of Xe+, they are all very close to the theoretical value of 1.127. In fact, if a k of 1.15 is used, the deduced V_i values (except for Xe⁺) are all in agreement with the accepted ionization potentials within the experimental uncertainties. This weak dependence of the V_i value on the power law coefficient explains why, in many of the earlier investigations, the V_i value extracted from the simple linear extrapolation approach are quite close to the currently accepted values. The variation of k for different noble gases may reflect the detailed effect of the electronic configurations. In particular, the result for the ionization of Xe suggests that perhaps the 1.3 eV energy separation of the 5P_{3/2} and 5P_{1/2} states is sufficiently large that it would be possible to actually study the power law leading toward the individual state. However, to carry out such analysis, more careful characterization of the instrument would be required.

Table 4-1. Threshold power law coefficients (k) and ionization potentials (Vi in eV) for the single ionization of noble gases

Ion	This experimental results		$V_i^{(b)}$	k-values from
	k ^(a)	Vi(a)	V ₁ ` '	other work
He ⁺	1.15	24.6±0.1	24.58	1.15 (c) (d)
Ne ⁺	1.1 (1.15	21.8±0.2 21.7±0.2)	21.6	1.06 ^(c)
Ar+	1.0	16.0±0.2	15.8	1.3 ^(d)
Kr ⁺	(1.15 1.0	15.8±0.2) 14.1±0.3	14.0	
	(1.15	13.8±0.3)		
Xe ⁺	1.5 (1.15	12.0±0.2 12.9±0.2)	12.1	

⁽a) This work

⁽b) Determined from optical spectra, C. E. Moore (1971).

⁽c) H. Lebius (1989)

⁽d) P. Marchand (1969)

4.3.3 The Second Ionization Potentials of Noble Gases

With increasing incident electron energy beyond the first ionization potential threshold, the ionization efficiency generally increases initially following a certain power law relation as observed above. With further increase in energy, more excited states in the resultant ion could be populated, and eventually, with sufficient incident energy, a second electron can be ejected, resulting in the production of a doubly charged ion. The threshold of this reaction is defined as the second degree ionization potential.

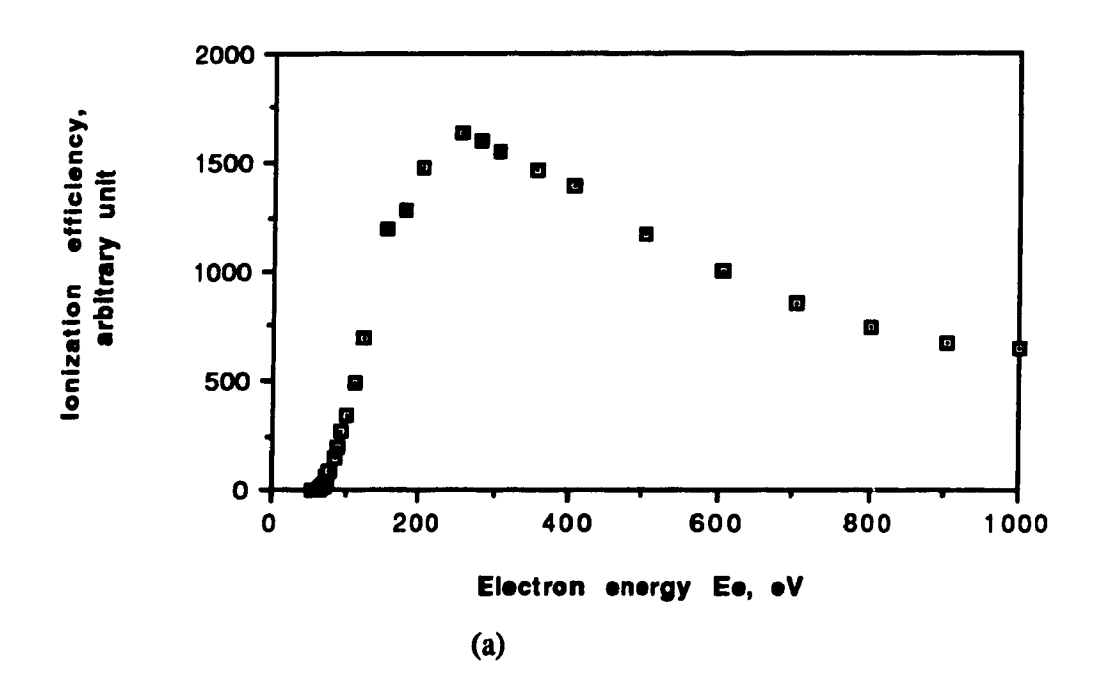
For helium, the second degree ionization will represent the complete stripping of the two s-electrons, while for the other noble gases, the lowest energy required corresponds to the ejection of two p-shell electrons. The coupling of the two electrons splits the configuration of s²p⁴ state into ³P₂, ³P₁, ³P₀, ¹D₂ and ¹S₀ states. The next group has the configuration corresponding to the ejection of one s-shell and one p-shell electron, resulting in the splitting into the triplet ³P₂, ³P₁, ³P₀ states. Table 4-2 shows the excitation energies for the first few levels of doubly ionized noble gases. Those excited energy states corresponding to the configuration of s²p⁴ are close to the ³P₂ ground state, while the next group of excited states, which correspond to the ionic configuration of s¹p⁵, lies at energies more separated from the previous group.

In principle, the production of He^{2+} should be an ideal case for the study of of the behavior of the ionization efficiency curve near the threshold since there can be no interference from the possible population of any excited states. However, in practice, this is not the case since He^{2+} has the same m/e ratio as H_2^+ . At an incident electron energy near the threshold of He^{2+} , the production of H_2^+ is sufficiently high so that it is difficult to carry out a meaningful detailed analysis of the ionization efficiency curve. Therefore, such study, carried out in the same manner as for He^+ , is being applied to the case of Ne^{2+} instead.

The ionization efficiency curve for the formation of Ne²⁺ is shown in Figure 4-10(a). It has the general shape of any ionization efficiency curve, with an initial increase in ionization cross section with incident electron energy, reaching a maximum, and then decrease monotonously. The behavior of the curve near the ionization threshold is shown in Figure 4-10(b), and it is obvious that the

Table 4-2. The first few energy levels (eV) of doubly ionized noble gases

Electronic configuration		Ion			
		Ne ²⁺	Ar ²⁺	Kr ²⁺	Xe ²⁺
	$^{3}P_{2}$ 0	0	0	0	0
s ² p ⁴	3P ₁	0.08	0.14	0.56	1.21
	3P ₀	0.11	0.19	0.66	1.01
	¹ D ₂	3.20	1.74	1.82	2.12
	¹ S ₀	6.91	4.12	4.10	4.64
s ¹ p ⁵	3P ₂ °	25.33	14.11	14.37	12.18
	3P ₁ ^o	25.40	14.23	14.80	12.83
	3P ₀ °	25.44	14.29	15.07	13.57



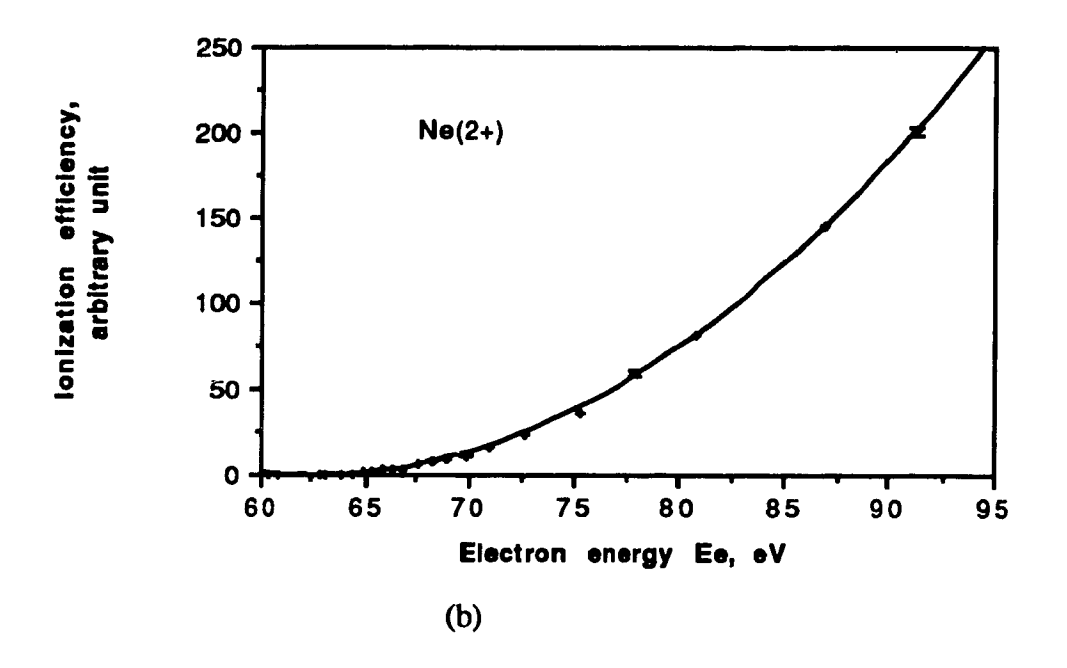


Fig. 4-10. Ionization efficiency curve for Ne²⁺: (a) over a 1000 eV energy range, and (b) near the ionization threshold.

extrapolation process must be carried out using a power law other than a linear function. With the same approach as before, we first restrict our analysis to an energy region about 10 eV beyond the threshold, and by using a fixed k a linear fit is carried out to extract the ionization potential V_i. Varying k between 1.9 and 2.4, V_i values between 63.2 and 61.8 eV are obtained. Figure 4-11 shows these fits. It can be seen that the extremes of these k values are not good fits to the experimental data, and the dependence of V_i on k shows about 0.3 eV for a

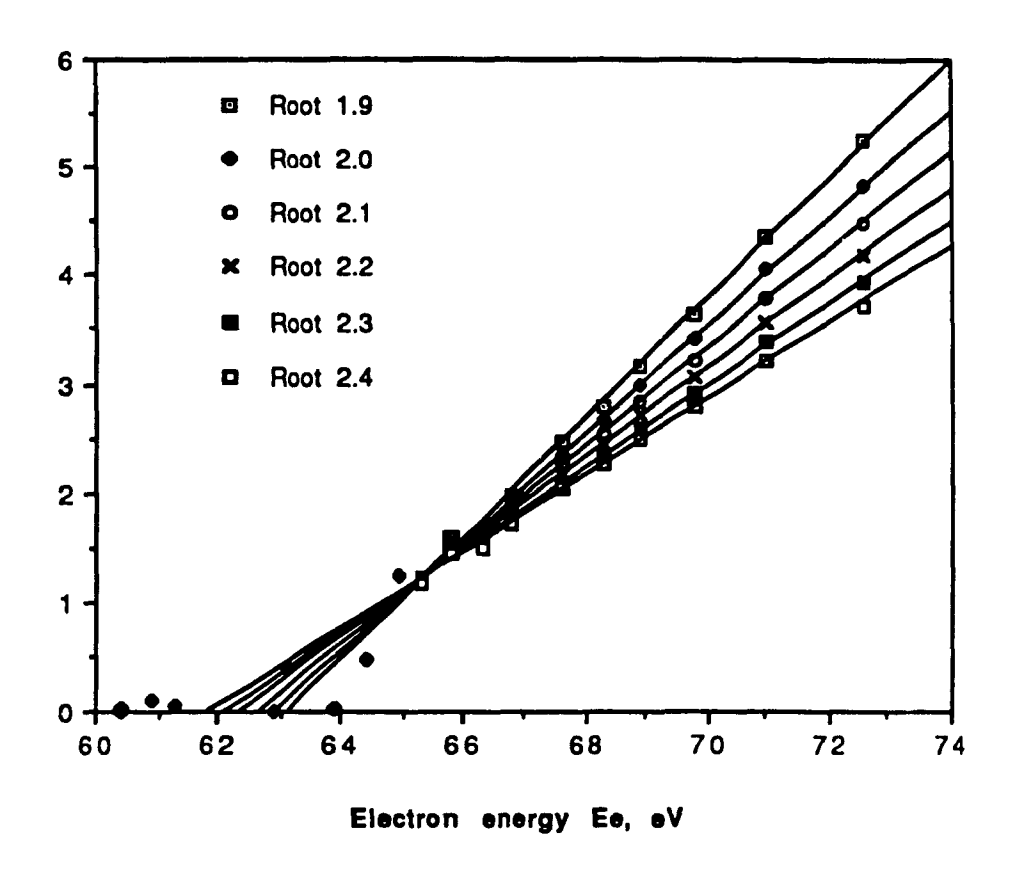


Fig. 4-11. Linear fitting of the kth roots of the experimental data for Ne^{2+} . k = 1.9, 2.0, 2.1, 2.2, 2.3 and 2.4.

variation of k 0.1. These V_i values are shown as one group of data points indicated by the arrows in Figure 4-12. Following the same procedure as in the case of He⁺, the analysis has been applied over different energy ranges, and the resultant V_i values extracted with different k are all shown in the same figure. Generally, the behavior is similar to the case of He⁺. The range of V_i values

converges when the analysis is applied to a smaller energy fitting range. However, the rate of convergence is slower than the case of He⁺, and in particular, it is difficult to extract a reliable V_i when the energy fitting range falls below 5 eV. These characteristics are due to the low ionization cross-section and particularly to the slow increase of the ionization efficiency above the threshold. On the other hand, the extracted V_i is relatively independent of the energy fitting range analyzed, and for k = 2, V_i is practically the same when the analysis is extended to a 30 eV range.

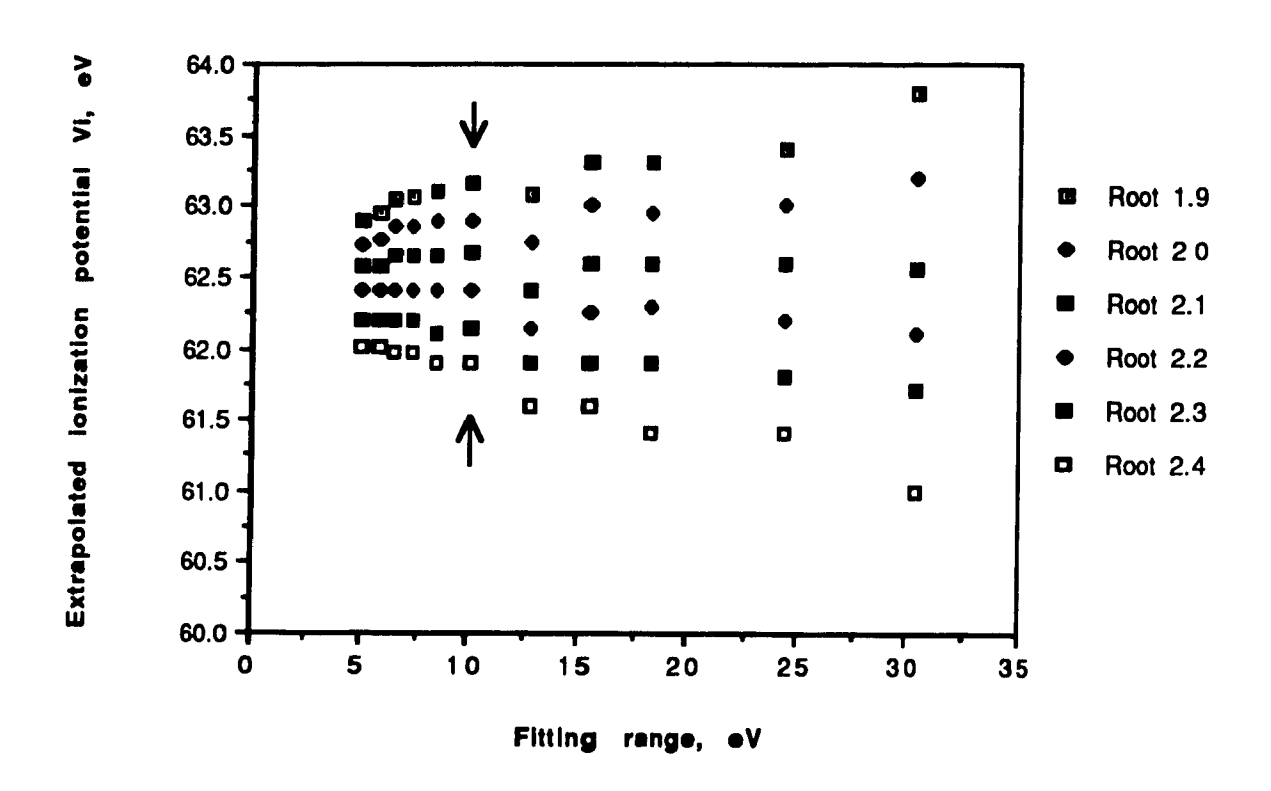
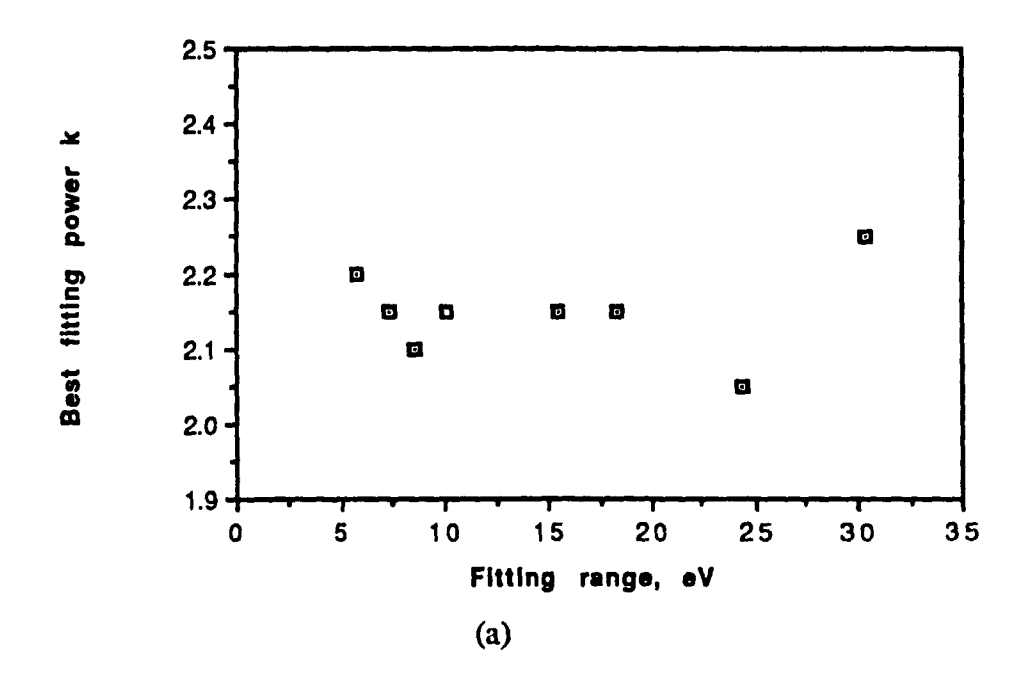


Fig. 4-12. Extracted ionization potential V_i varying with both the length of the fitting range above threshold and the fitting power law coefficient k-value.

Finally, we allow both k and V_i to vary to produce the best least square fit over different energy ranges. The results are shown in Figure 4-13. Within an analysis region of 20 eV above the threshold, k = 2.15 and $V_i = 62.5 \pm 0.3$ eV are obtained. This k value should be compared to the theoretical prediction of



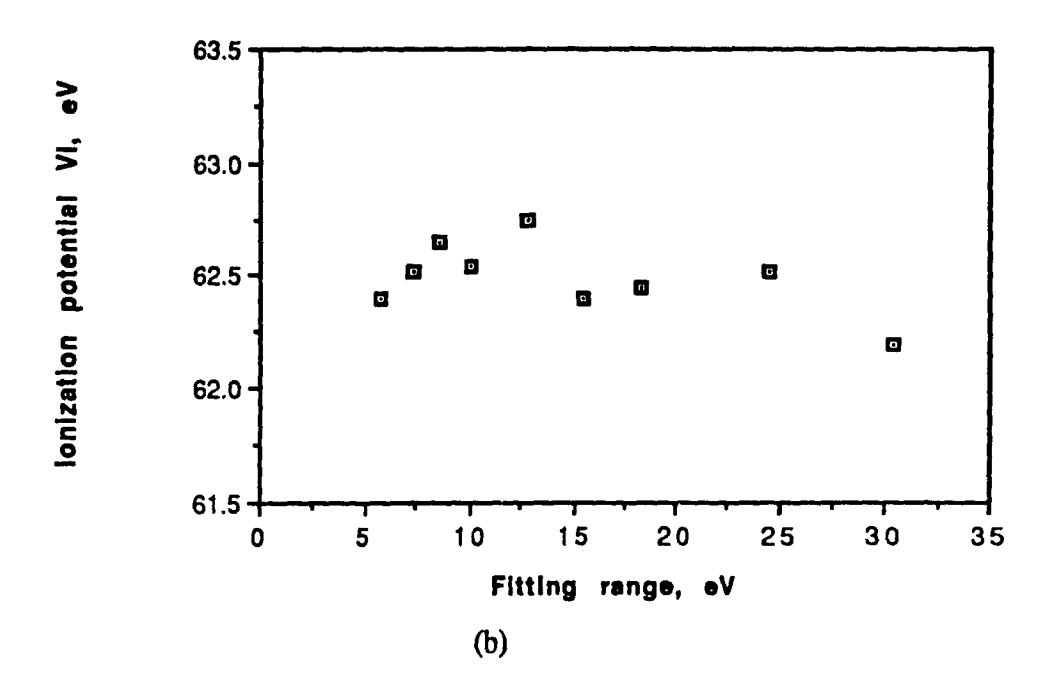


Fig. 4-13. (a) The best fitting power law coefficient k and (b) the extrapolated ionization potential V_i varying as a function of the energy range above threshold for Nc^{2+} .

2.270 [38]. A previous reported experimental k-value for Ne²⁺ is 2.04 from Lebius ^[44] in 1989, which is close to our result. The extracted ionization potential of $62.5 \, \text{eV}$ for k = 2.15 is in good agreement with the spectroscopic value of $62.7 \, \text{eV}$ ^[29]. These results indicate that the same least square fit approach is also valid for the analysis of the second ionization potential.

Although there exist some excited states within the fitting range in the above analysis, the influence from these excited states on the fitting results does not seem very significant. In the following study of other noble gases, caution will be taken in selecting the fitting range so that high level excited states corresponding to the ejection of s-shell electrons will not be included.

The least square fitting for the He²⁺ ionization efficiency curve extending over a 20 eV range yielded k = 2.0 and $V_i = 79.2 \pm 0.5$ eV, as shown in Figure 4-14. The second ionization potential thus extracted is in good agreement with the accepted value of 79.0 eV [29]. In earlier work, the second ionization potentials were often extracted using square root extrapolation (i.e. k = 2) of the ionization efficiency curves. In our work, this is also the case. As a comparison, when k = 2.15 is adapted, $V_i = 78.5 \pm 0.5$ eV is obtained. This discrepancy demonstrates the necessity of having a good knowledge of the k value. In the present work, the magnitude of the background is due to the H₂ impurity, and it should be possible to reduce by using the sample gas of ³He. In this case, a precise determination of the power law will be possible.

The least square fitting to the ionization efficiency curve for Ar^{2+} is carried out over a 10 eV range, yielding k = 1.95 and $V_i = 43.6 \pm 0.3$ eV, which is in good agreement with the spectroscopic ionization potential of 43.4 eV ^[29]. For k = 2.15, the extracted V_i is 43.2 ± 0.3 eV. Both the fitting lines are shown in Figure 4-15. Recently, Koslowski ^[41] reported a k value of 2.6 for Ar^{2+} also using a fitting range of 10 eV. If this k-value of 2.6 is applied to the present data, the extracted V_i would be 1.5 eV lower than the accepted ionization potential.

For the Kr^{2+} ionization efficiency curve, the least square analysis is carried out over a 12 eV range beyond the threshold, leading to a k value of 2.0 and V_i value of 38.6 ± 0.4 eV, which agrees with the spectroscopic ionization potential of 38.6 eV ^[29]. Again as a comparison, k is fixed at 2.15 and a resultant V_i of 38.2 ± 0.4 eV is obtained. Figure 4-16 shows these two fitting lines. Earlier work by Lebius ^[44] in 1989 has resulted in a k-value of 1.97, quite consistent with the result from this work.

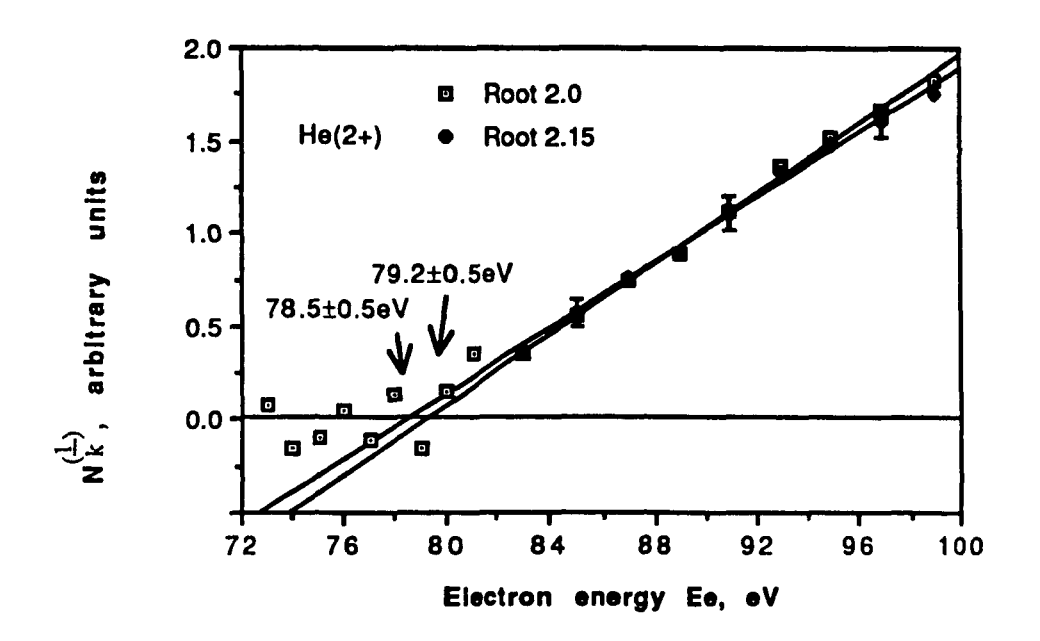


Fig. 4-14. Ionization potential of He²⁺ extracted from the linear fit of the 2.0th and 2.15th root of the experimental data.

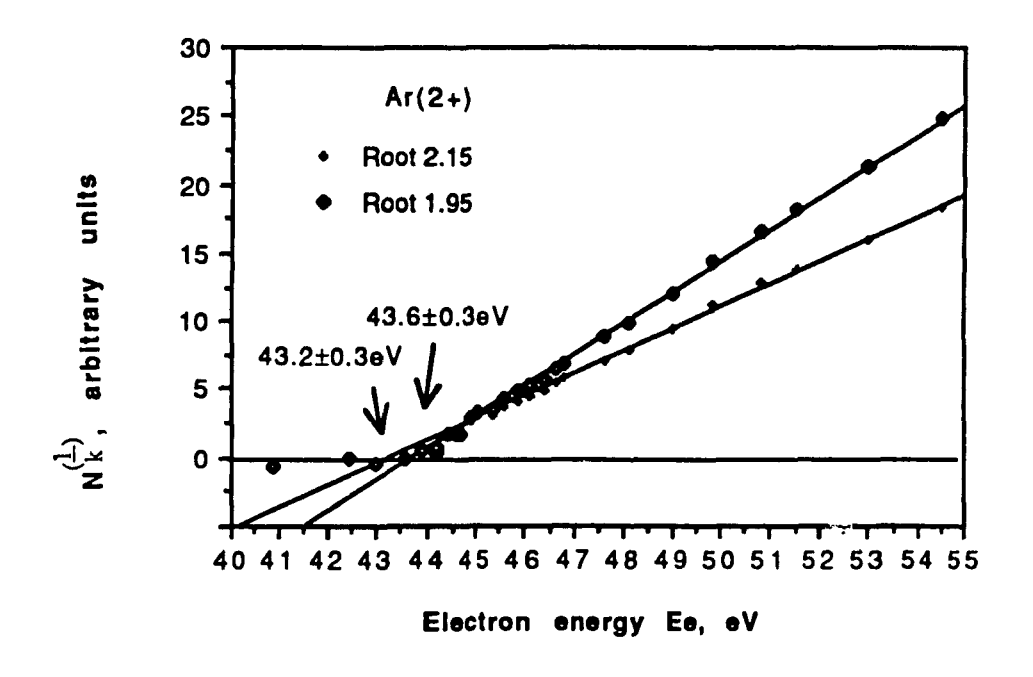


Fig.4-15. Ionization potential of Ar²⁺ extracted from the linear fit of the 1.95th and 2.15th root of the experimental data.

In the case of Xe^{2+} , the excited states from the s^1p^5 configuration are situated at energy level slightly higher than $12\,eV$. To avoid their interference, the least square fitting to the ionization efficiency curve is carried out over a $10\,eV$ range, yielding a k-value of 2.05 and V_i value of $33.6\pm0.3\,eV$. For k=2.15, the extracted V_i is $33.5\,eV$. Both the extracted V_i values agree with the spectroscopic ionization potential of $33.3\,eV^{[29]}$ within the experimental uncertainty range. As a comparison, Lebius $^{[44]}$ reported his result of k=1.85 in 1989. His fitting to the ionization efficiency curve was limited to a $6\,eV$ range, which might be a factor causing the difference in the resultant k values.

4

For the second degree of ionization of the noble gases, the same approach as the analysis of the first ionization efficiency curves using least square fitting has been employed. To avoid the interference from high excited states, attention has been paid to the setting of the fitting range, so that only those very low excited energy states corresponding to the ejection of two p-shell electrons are included. The k-values obtained for different gases are generally slightly different from each other, and all of them are close to the ionization degree (2), but lower than the theoretical prediction of 2.270. Table 4-3 summarizes all the experimental k-values for the second degree of ionization of the noble gases obtained from this work together with the extracted V_i values. Currently accepted ionization potentials are also listed in the table. It can be seen that the 1-values from this work are generally in agreement with others except that for Ar2+, and the extracted second ionization potentials for noble gases are all within 0.5 eV of the well accepted ionization potentials. The theory about the power law coefficient k-value for the second ionization was only developed recently [38], and the experimental data on the k-value are still very limited. Therefore, further comparison on the experimental results is difficult to make.

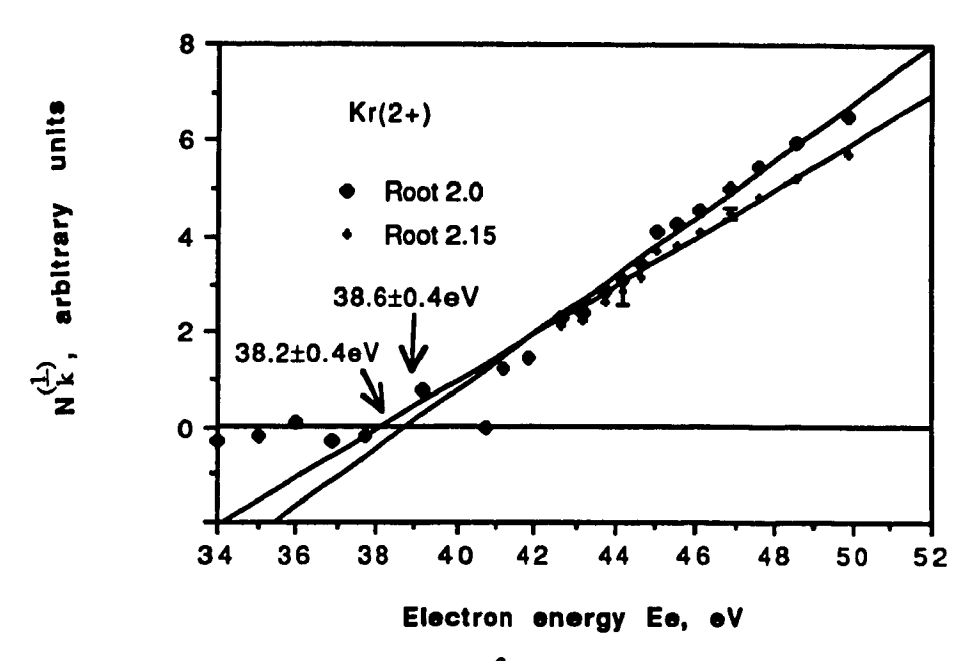


Fig. 4-16. Ionization potential of Kr^{2+} extracted from the linear fit of the 2.0th and 2.15th root of the experimental data.

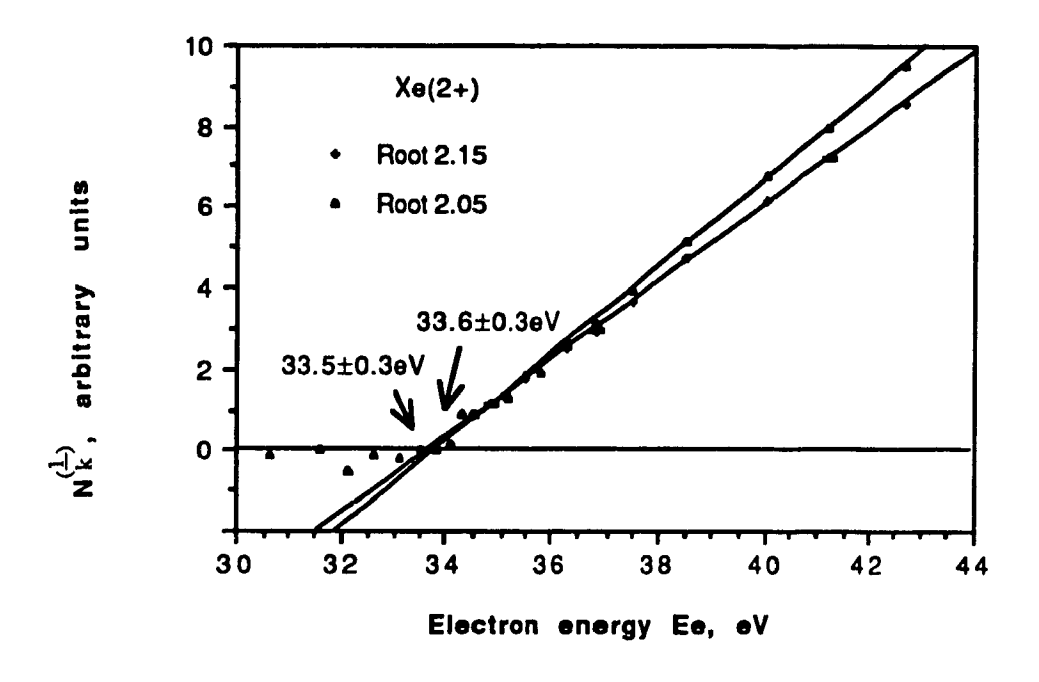


Fig. 4-17. Ionization potential of Xe^{2+} extracted from the linear fit of the 2.05th and 2.15th root of the experimental data.

Table 4-3. Threshold power law coefficients (k) and ionization potentials (Vi in eV) for the double ionization of noble gases

Ion	k ^(a)	$V_i^{(a)}$	V _i (b)	k-values from other work
He ²⁺	2.0	79.2±0.5	79.0	2.14 ^(c)
	(2.15	78.5±0.5)		
Ne ²⁺	2.15	62.5±0.3	62.7	2.04 ^(c)
Ar ²⁺	1.95	43.6±0.3	43.4	2.6 ^(d)
	(2.15	43.2±0.3)		
Kr ²⁺	2.0	38.4±0.4	38.6	1.97 ^(c)
	(2.15	38.2±0.4)		
Xe ²⁺	2.05	33.6±0.3	33.3	1.85 ^(c)
	(2.15	33.5±0.3)		

⁽a) This work

⁽b) Determined from optical spectra, C. E. Moore (1971).

⁽c) H. Lebius (1989)

⁽d) H. R. Koslowski (1987)

4.3.3 The Third and Higher Degrees of Ionization Potentials of Noble Gases

For the third and higher degrees of ionization of noble gases, the ionization cross-sections become progressively lower, so it is generally more difficult to obtain a good ionization efficiency curve. Also the resultant ions have complicated electronic configurations, with many levels spread over a wide energy range, and the analysis is hampered by the ionization process leading to many widely spread excited states. Theoretically, the ionization efficiency curve just above the threshold will have a k-value close to the degree of ionization [34]. More recently, a k-value of 3.525 for the third degree of ionization has been proposed [40], but no similar work has been done for the higher degrees of ionization processes. As a result, little detailed experimental work in this area has been carried out. In the present work, third and high degrees of ionization efficiency curves for the noble gases Ne to Xe have been obtained, and the results are analyzed using the same approach as before, i.e., applying the least square analysis of the data above the threshold by varying both k and V_i.

For neon, ion species up to Ne⁴⁺ have been observed, and Figure 4-18 shows the ionization efficiency curves obtained for the formation of Ne³⁺ and Ne⁴⁺. The shape of the two curves are in the general form of arriving a broad maximum and then decreasing monotonously, and the relative amplitudes of the two curves are a valid indication of the ionization efficiencies from the two species. Figure 4-19 shows the least square fitting lines for Ne³⁺ and Ne⁴⁺. The extracted ionization potential V_i for Ne³⁺ is 137 ± 3 eV with a k-value of 3.3 [Figure 4-19(a)], and the V_i value for Ne⁴⁺ is 231 ± 10 eV with a fitting of the k-value of 2.1 [Figure 4-19(b)]. Both the V_i values are in agreement with the spectroscopic results [29].

The ionization efficiency curves for Ar³⁺, Ar⁴⁺, Ar⁵⁺ and Ar⁶⁺ are shown in Figure 4-20. Again, their relative ionization efficiencies are represented by their relative counting rates. The general shape of the ionization efficiency curves for Ar³⁺, Ar⁵⁺ and Ar⁶⁺ have the normal form, but for Ar⁴⁺ the curve seems to consist of two superimposed ionization efficiency curves located about 100 eV apart. In fact, earlier investigators with less sensitive techniques detected only the second threshold potential of 259 eV [53], and this result has been quoted in many articles published in the 1950s. Later in 1960, Fox [54] identified the lower

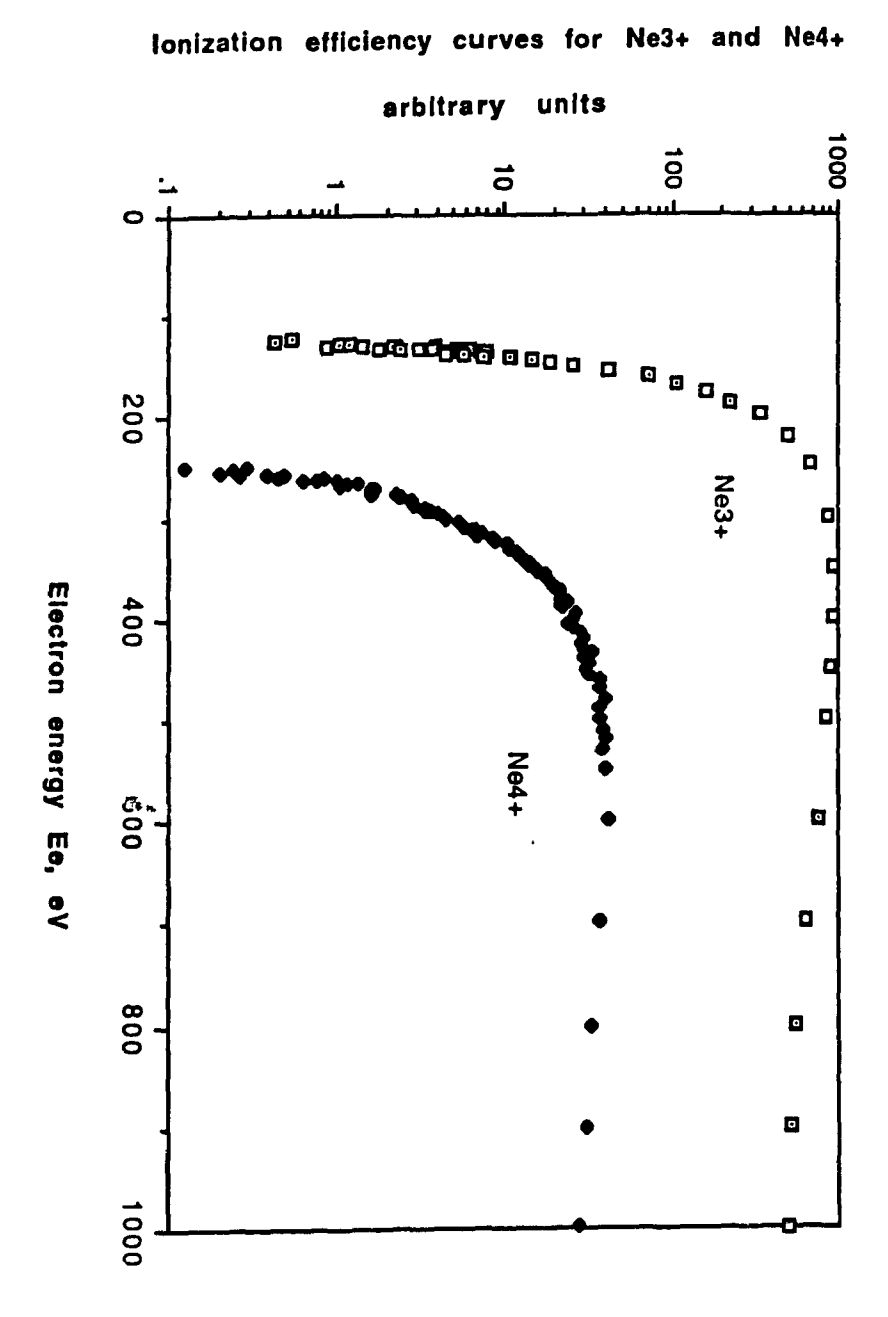


Fig. 4-18. Ionization efficiency curves for Ne³⁺ and Ne⁴⁺.

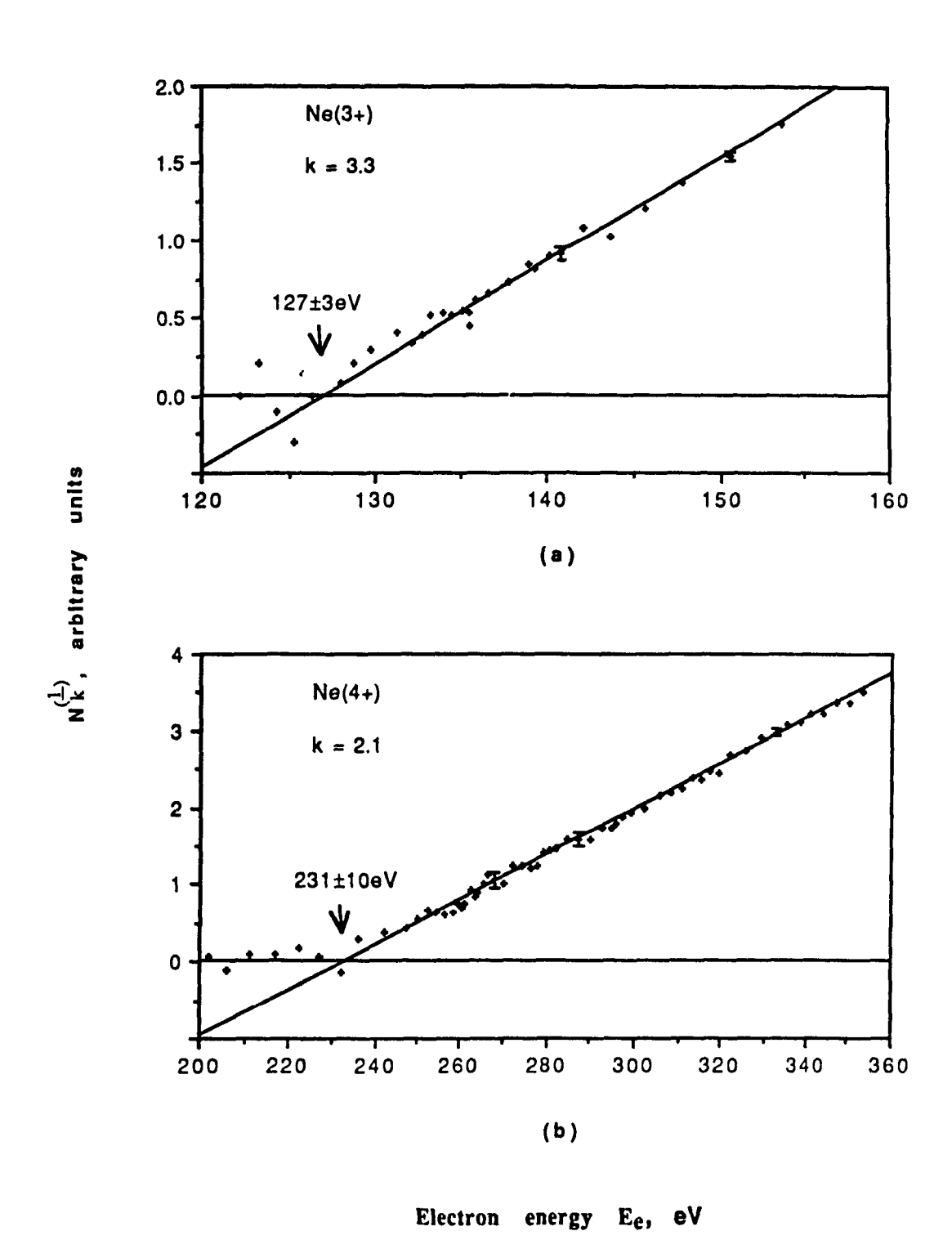


Fig. 4-19. Ionization potentials of Ne³⁺ (a) and Ne⁴⁺ (b) extracted from the linear fit of the kth root of the experimental data.

Ionization efficiency curves for Ar(3+), Ar(4+), Ar(5+) and Ar(6+), arbitrary units

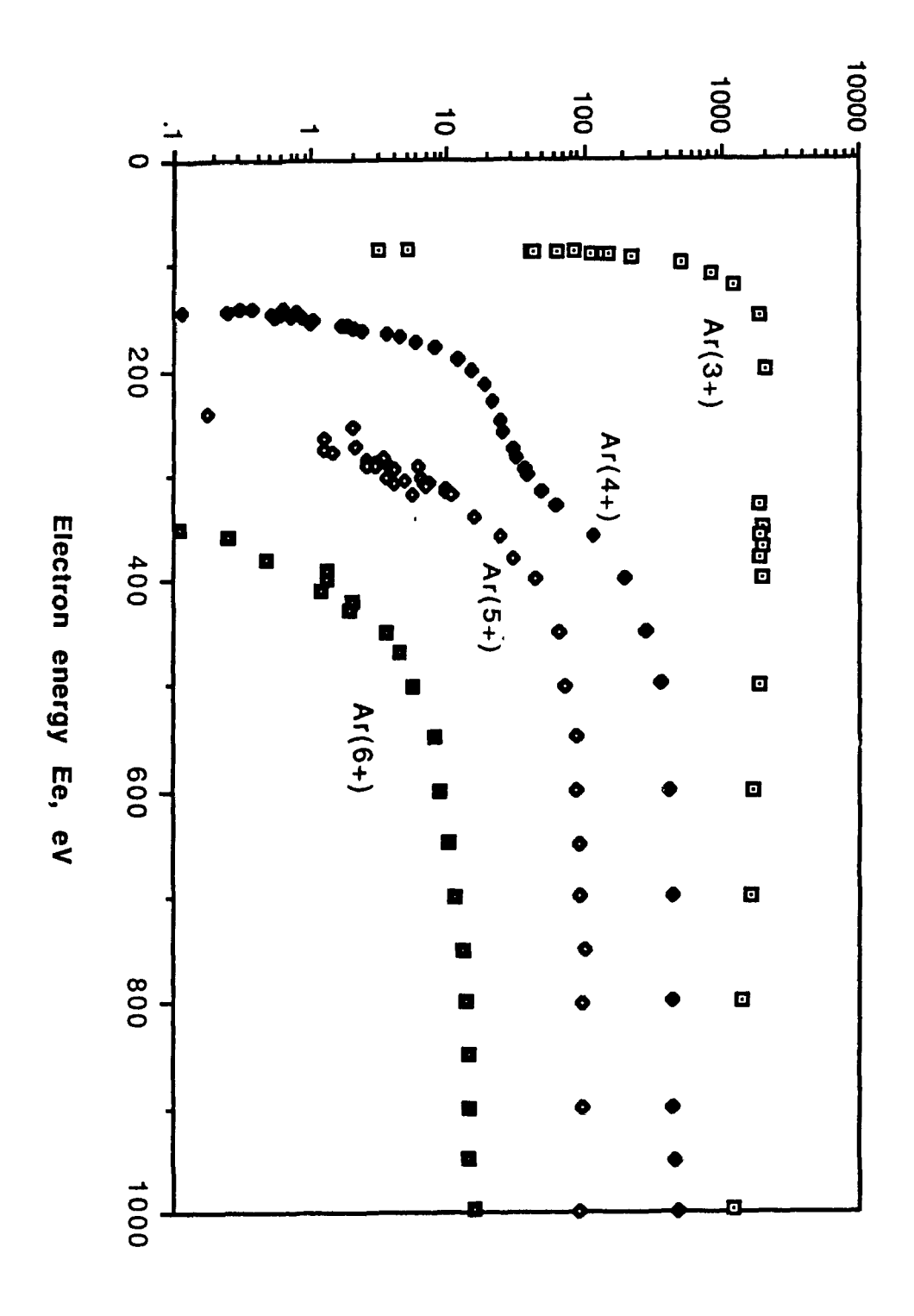
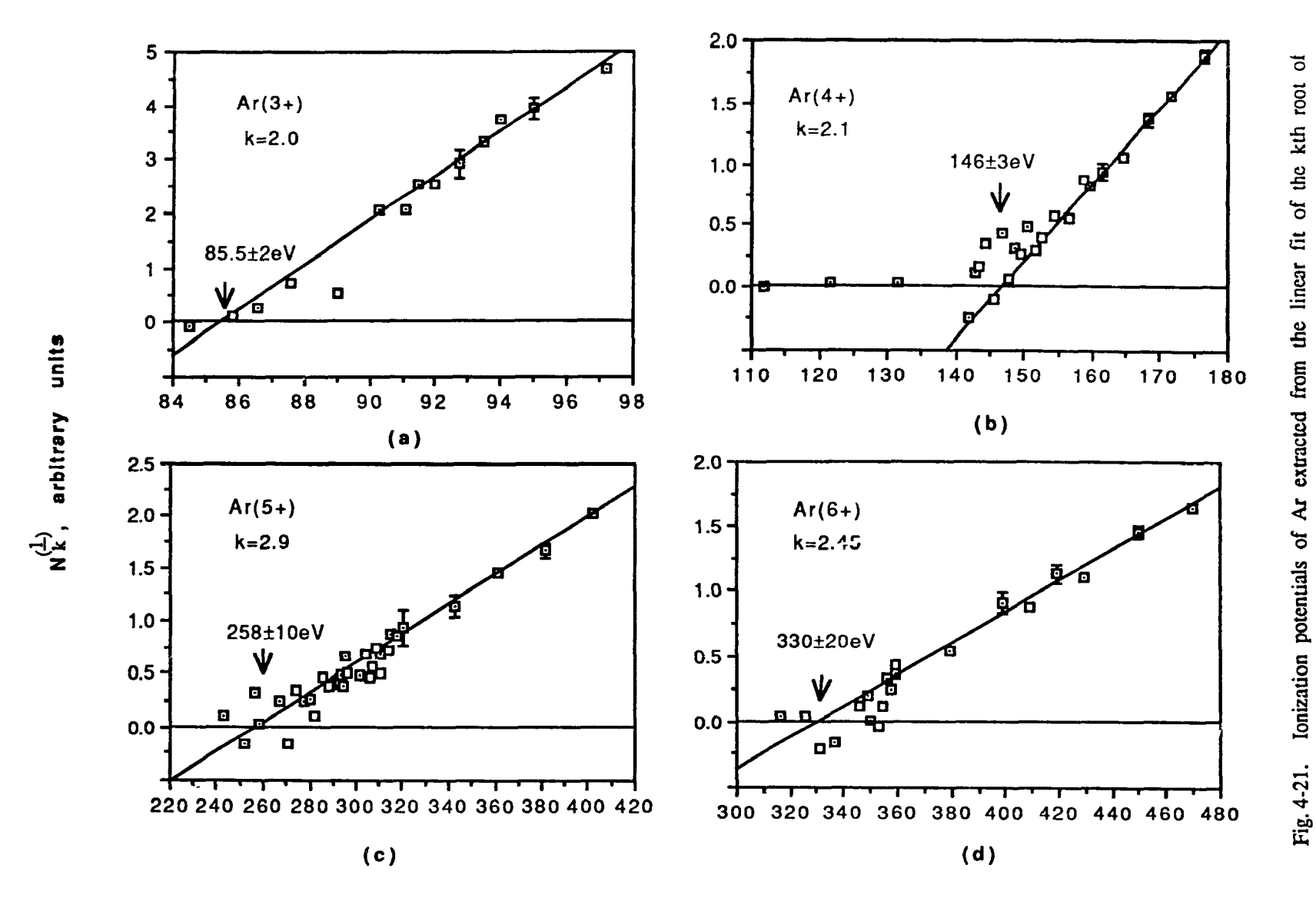


Fig. 4-20. Ionization efficiency curves for Ar^{3+} , Ar^{4+} , Ar^{5+} and Ar^{6+} .

(d) for Ar⁶⁺.

the experimental data: (a) for Ar3+, (b) for Ar4+, (c) for Ar5+ and



Electron energy Ee, eV

4 3

.

ionization threshold and obtained a Vi of 145 eV, which is more in line with what is expected from the spectroscopic data. He attributed the second threshold to the excitation of the inner electron core. In the present work, the ionization efficiency curve covers over 5 orders of magnitude for the cross-section and the double threshold is clearly observed. The ionization efficiency curves for Ar3+, Ar4+, Ar5+ and Ar6+ are analyzed by the least square fitting and the resultant k values are 2.0, 2.9, 2.1 and 2.45, respectively. The fitting lines are shown in Figure 4-21. For Ar³⁺, Ar⁴⁺ and Ar⁶⁺, the extracted ionization potentials are 85.5 ± 2 eV, 146 ± 3 eV and 330 ± 20 eV respectively, and they are in agreement with the values from spectroscopic data within the experimental uncertainties. While for Ar⁵⁺, the resultant V_i of $258 \pm 10 \,\text{eV}$ is much higher than the spectroscopic result of 219.1 eV. This 258 eV threshold is very close to the second threshold obtained in the formation of Ar4+. It is quite possible that the Ar4+ is produced at such a highly excited state that it has a non-negligible branching ratio to decay into Ar5+ with the ejection of another electron. If this is the case, then there should be another threshold in the fifth degree ionization efficiency curve. We have attempted to locate this lower threshold, but failed to detect an observable threshold near 220 eV region. This is due to the fact that Ar5+ has the same m/e ratio as O2+, which exists abundantly in the residual gas of the chamber. The present value of 258 eV should therefore be taken with caution.

The ionization efficiency curves for the formation of Kr^{3+} , Kr^{4+} and Kr^{5+} are shown in Figure 4-22. With the least square fitting approach, the best fitting powers are found to be 2.1 for Kr^{3+} , 2.9 for Kr^{4+} , and 4.7 for Kr^{5+} . These k values yield $V_i = 75.1 \pm 1 \, \text{eV}$, $130 \pm 2 \, \text{eV}$ and $211 \pm 3 \, \text{eV}$, as shown in Figure 4-23. The extracted V_i for Kr^{3+} agrees with the well accepted value. There is no spectroscopic data for the ionization potentials of Kr^{4+} and Kr^{5+} . The results from other measurements are listed in Table 4-7. It can be seen that large discrepancy exists in the resultant V_i values for Kr^{4+} and Kr^{5+} , indicating the difficulty in extracting these values reliably from the data.

Figure 4-24 shows the ionization efficiency curves for Xe^{3+} , Xe^{4+} Xe^{5+} , Xe^{6+} and Xe^{7+} . The best fitting powers are determined to be 2.2, 2.0, 2.95, 2.85 and 2.4, respectively. The fitting lines, shown in Figure 4-25, yield V_i values of 65.9 ± 0.5 eV for Xe^{3+} , 112 ± 2 eV for Xe^{4+} , 169 ± 3 eV for Xe^{5+} , 250 ± 5 eV for Xe^{6+} and 365 ± 10 eV for Xe^{7+} . Similar to the case of Kr, there are no spectroscopic data for the ionization potentials of Xe^{4+} , Xe^{5+} , Xe^{6+} and Xe^{7+} . The spectroscopic result for Xe^{3+} is 65.4 eV [29], which agrees with the

1

lonization efficiency curves for Kr(3+), Kr(4+) and Kr(5+), arbitrary units

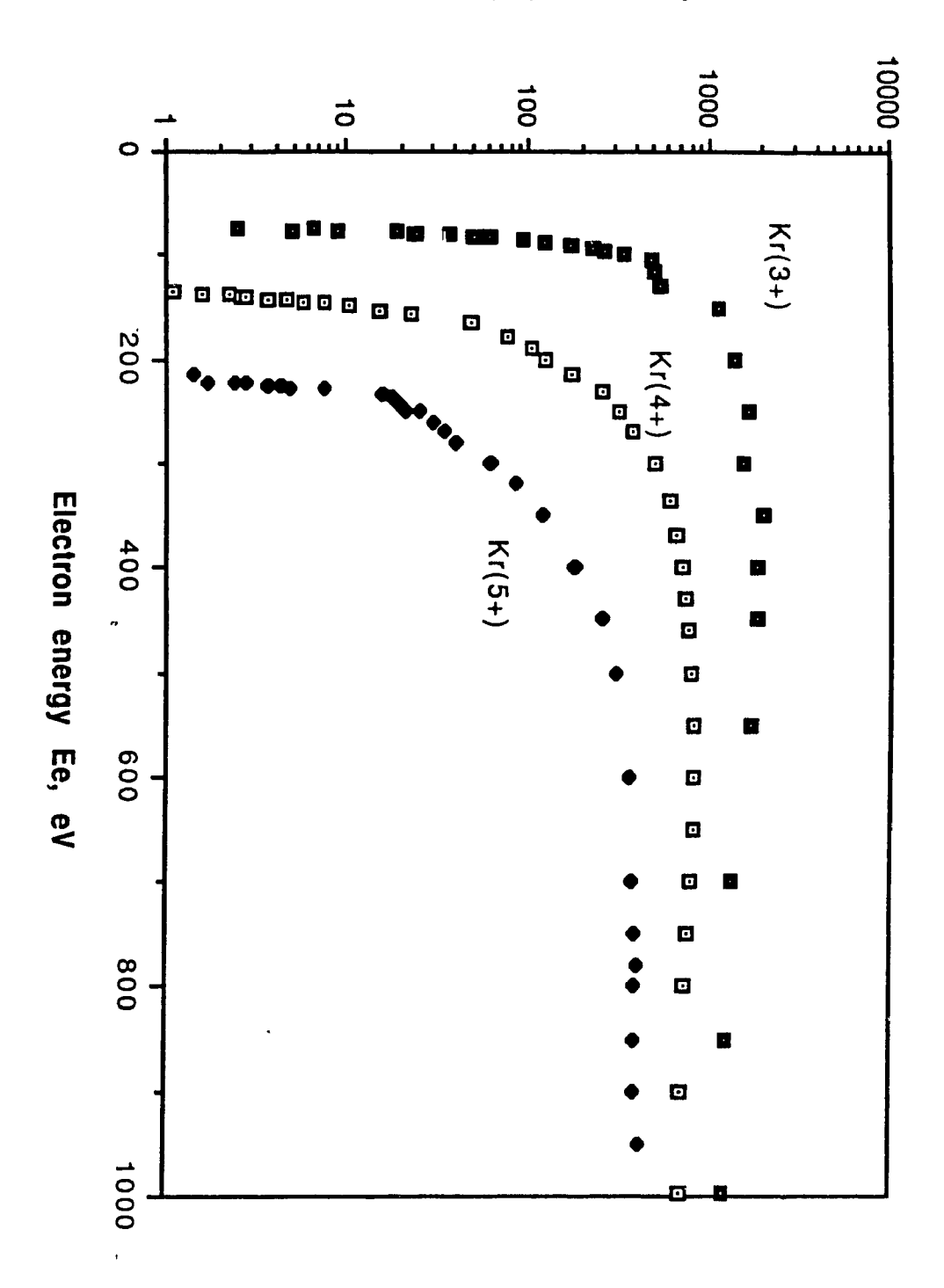


Fig. 4-22. Ionization efficiency curves for Kr^{3+} , Kr^{4+} and Kr^{5+} .

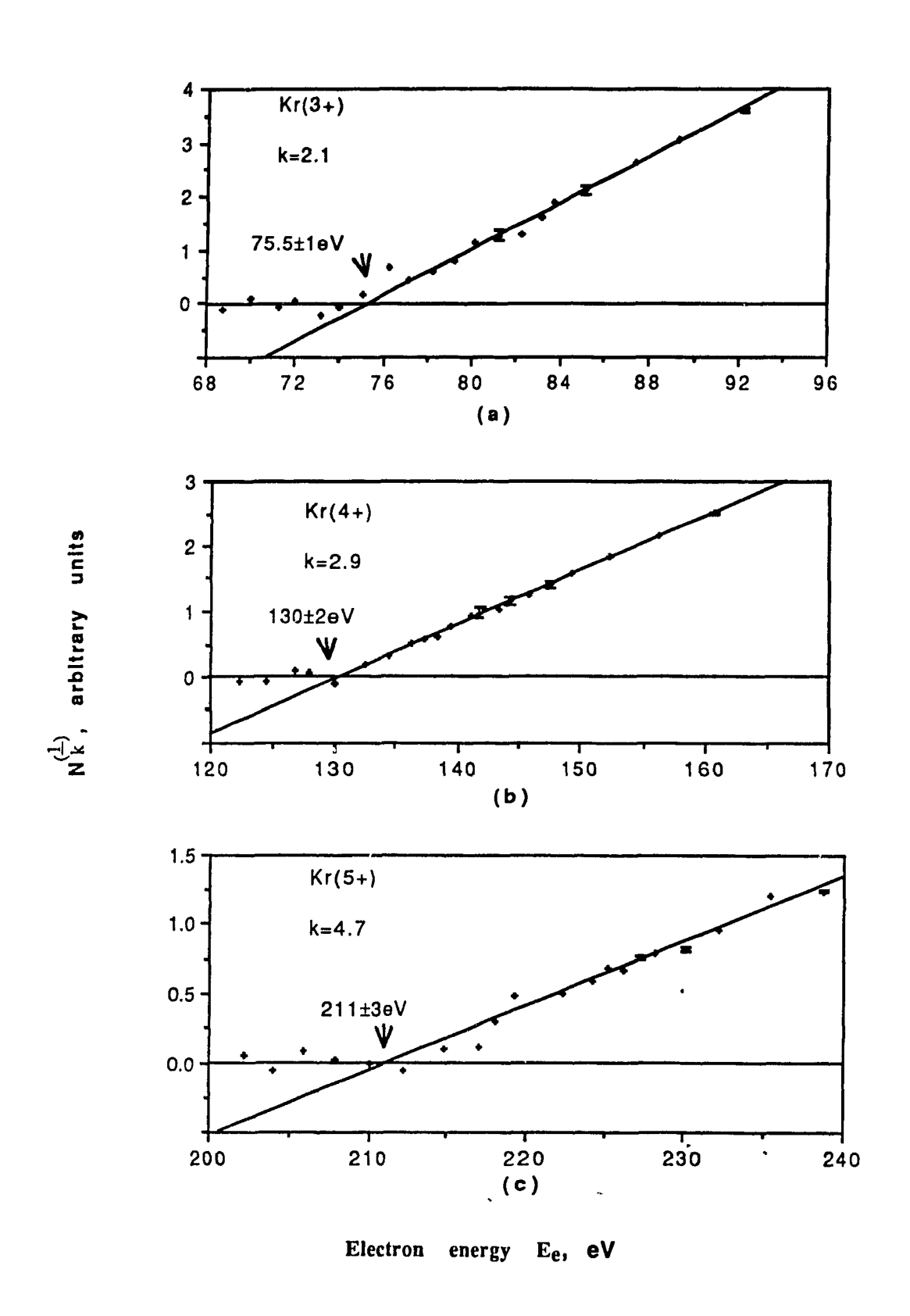


Fig. 4-23. Ionization potentials of Kr extracted from the linear fit of the kth root of the experimental data: (a) for Kr^{3+} , (b) for Kr^{4+} and (c) for Kr^{5+} .

Ionization efficiency curves for Xe(3+),Xe(4+), Xe(5+),Xe(6+) and Xe(7+), arbitrary units

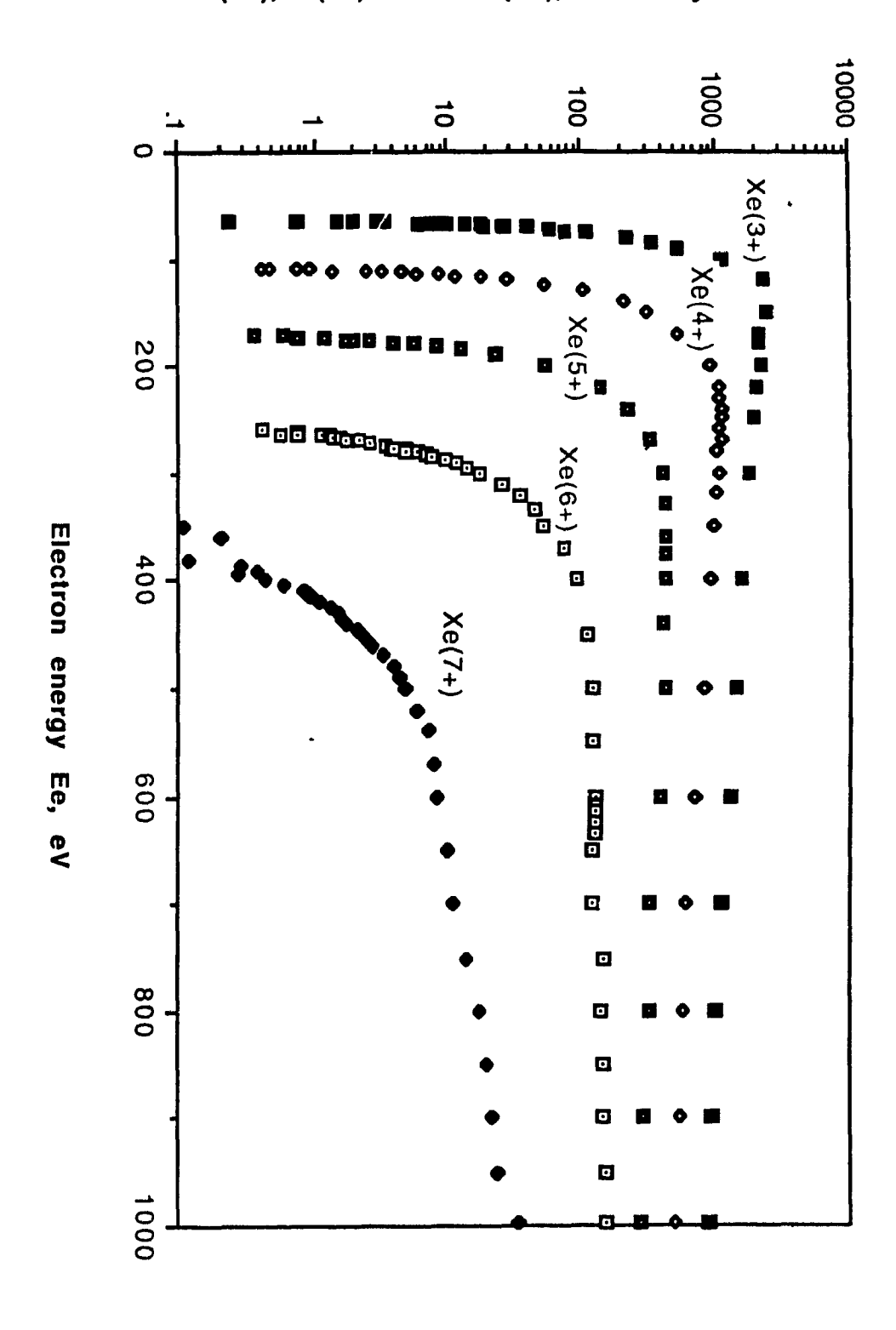
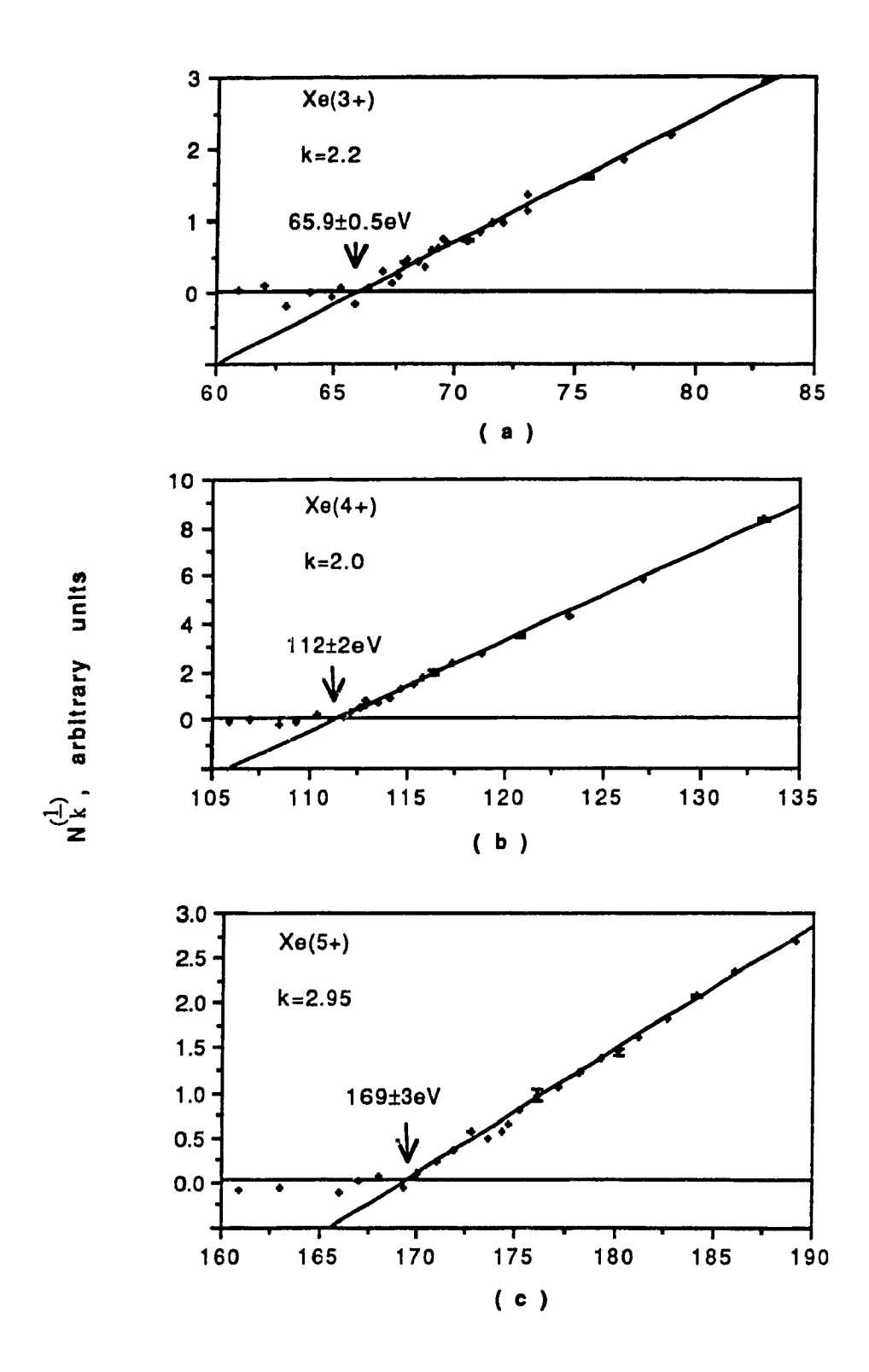


Fig. 4-24. Ionization efficiency curves for Xe³⁺, Xe⁴⁺, Xe⁵⁺ Xe⁶⁺ and Xe⁷⁺.



Electron energy Ee, eV

4

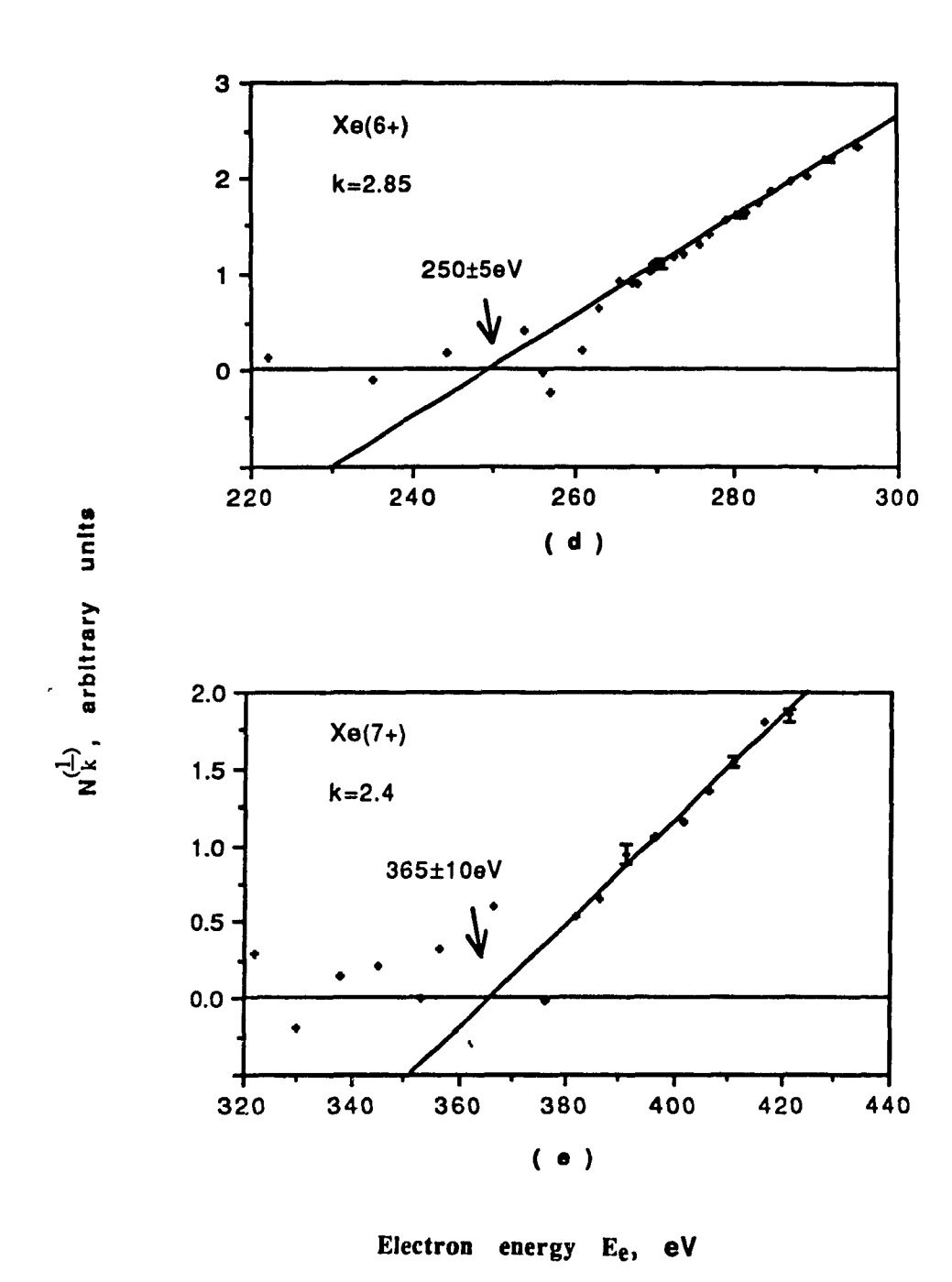


Fig. 4-25. Ionization potentials of Xe extracted from the linear fit of the kth root of the experimental data: (a) for Xe^{3+} , (b) for Xe^{4+} , (c) for Xe^{5+} , (d) for Xe^{6+} and (e) for Xe^{7+} .

extracted value from this work.

The power law coefficients for the third and higher degrees of ionization of the noble gases are listed in Table 4-4. The k-values extracted vary from 2.0 to 4.7, but they show no systematic trend at all, and their comparison with the few reported values exhibits little correlation. One of the main reasons for these discrepancies is the different analyzing procedure applied in each case. As mentioned earlier, the electronic configuration for each ion is very complicated and many excited states contribute to the overall ionization efficiency curve. The extracted power law coefficient must then be dependent on the energy range of the fit. Without knowing the exact approach used by the other analysis. it is difficult to make detailed comparisons. In this work, we have attempted to examine the validity of extracting the ionization potentials from the power law approach. In general, the energy range used is quite wide and the resultant k value may not represent the true k value just above the threshold. In the cases of high degrees of ionization, the signal-to-noise ratio becomes very low. Therefore, a large fitting range is needed to determine the power law. In this kind of fitting range, there always exist many excited state ionizations or inner shell ionizations instead of those theoretically defined ground state - ground state transitions. Generally, when too wide an energy range is used, the fitting of the power law coefficient results in a much lower value than that expected from an ideal model. As a consequence, the extracted ionization potentials can also be affected. From the trends observed for the first and second degree ionization processes, too low a k-value will result in a higher V_i.

The resultant ionization potentials are listed in Table 4-5, together with the values obtained from spectroscopic measurements and from other experiments. It can be seen that the resultant ionization potentials from the present work are higher than the spectroscopic values. As mentioned above, the possible reason for this might be that the fitting powers are much lower than expected. Therefore, the extracted V_i values should be considered as upper limits of the "real" ionization potentials. Compared to the results from other experiments, large discrepancies also exist. Up to now, the number of reports on the ionization potentials for high degree ionization of noble gases is still very limited, hence, judgement of the results is difficult. There is clearly a need for further investigation into both the theoretical and experimental aspects of this subject.

Table 4-4. Threshold power law coefficients (k) for third and higher degrees of ionization of noble gases

Ion	Experiment	Other work	
Ne ³⁺	3.3	3.16 ^(c)	
Ne ⁴⁺	2.1	4.15 ^(c)	
Ar ³⁺	2.0	3.0 ^(d)	
Ar ⁴⁺	2.1	2.5 ^(d)	
Ar ⁵⁺	2.9		
Ar ⁶⁺	2.45		
Kr ³⁺	2.1	2.63 ^(c)	
Kr⁴+	2.9		
Kr ⁵⁺	4.7		
		(4)	
Xe ³⁺	2.2	2.80 (c)	
Xe ⁴⁺	2.0	2.6 ^(c)	
Xe ⁵⁺	2.95		
Xe ⁶⁺	2.85		
Xe ⁷⁺	2.4		

⁽c) H. Lebius (1989)

⁽d) H. R. Koslowski (1987)

Table 4-5. Third and higher degrees of ionization potentials (Vi in eV) of noble gases

Ion	$V_i^{(a)}$	V _i ^(b)	V i ^(c)	۷ _i (d)
Ne ³⁺	127±3	127	126	129
Ne ⁴⁺	230±10	224	220	240
Ar ³⁺	85.5+2	84.3	81	85
Ar ⁴⁺	147±5	144.1	136	147
Ar ⁵⁺	258±10	219.1	209	285
Ar ⁶⁺	320±20	310.4	298	430
Kr ³⁺	77±3	75.5	71	76
Kr ⁴⁺	131±5		119	134
Kr ⁵⁺	211±10		181	204
Xe ³⁺	65.9±0.5	65.4	61	65
Xe ⁴⁺	112±2		101	110
Xe ⁵⁺	169±3		151	172
Xe ⁶⁺	250±5		216	248
Xe ⁷⁺	365±10		308	362

⁽a) This work

⁽b) Spectroscopic results of C. E. Moore (1971)

⁽c) P. A. Redhead (1967)

⁽d) F. A. Stuber (1965)

CHAPTER 5

SUMMARY AND CONCLUSIONS

A quadrupole mass filter with cylindrical rod assembly has been constructed. The radius and the spacing of the rods have been properly designed to approximate the ideal electric field pattern. The associated electronics and an ionization chamber have also been built to complete the experimental apparatus.

The operating characteristics of the quadrupole mass filter were examined by using ions created by electron impact of residual gases. The effects of the RF frequency, the RF scanning voltage amplitude, the U/V ratio and the ion injection energy on the mass resolution as well as on the ion transmission efficiency have been studied and compared to the properties predicted with a stability diagram. With an increase of the RF frequency and the RF scanning voltage, both the mass resolution and the ion transmission efficiency can be improved. In contrast, the increase of the U/V ratio will improve the mass resolution but reduce the ion transmission efficiency. The ion injection energy also affects the operating characteristic of the quadrupole mass filter, particularly when the ion injection energy is high. The resolving power of the quadrupole mass filter is tested with xenon gas under typical experimental conditions. The resolved isotope peaks showed a mass resolution of 130, compared to the theoretical limit of 180 under those conditions. In addition, the absolute ion transmission efficiency under typical operating conditions is estimated to be about 10%.

The electron-impact ionization of noble gases has been studied using this experimental set-up. Measurements of the ionization efficiency curves for various charge states of all the noble gases have been carried out. Multiple charged species up to 2+ helium ions, 4+ neon ions, 6+ argon ions, 5+ krypton ions and 7+ xenon ions have been observed. Special attention has been paid to the behavior of the ionization efficiency curve near the ionization threshold, and a power-law model has been used to fit the curve in an energy range above

threshold. For the first ionization of helium, the linear fitting of the kth root of the ionization efficiency curve as a function of impact electron energy leads to a k = 1.15 power law, compared to a theoretical k = 1.127 power law. For the other noble gases, the k values obtained vary from 1.0 to 1.5. The first ionization potentials, which are extrapolated from these k values, have been found to depend only weakly upon the exact k values, and are in good agreement with those ionization potential values determined by the spectroscopic method.

The ionization efficiency curve for Ne²⁺ has been found to fit a 2.15 power law near the threshold. For the 2+ ions of other noble gases, the k values are equal or close to 2.0, which is slightly lower than the k-value of 2.270 predicted by the theory. The fitting power law coefficients for those other noble gases vary from 1.95 to 2.05. The second ionization potential values extrapolated by these experimental power laws also agree well with the spectroscopic data.

For the third ionization, the k values are generally much lower than the value of 3 525 predicted by the theory, but the extrapolated ionization potentials are still consistent with the spectroscopic results. For higher ionization, general theories suggest a k-value of the order of the charge state of the ion. However, our k-values are generally much lower than the charge state of the ions. This is likely due to the influence of the excited states located near the ionization threshold. Therefore, the power law fitting method used here might only extract the upper limits of ionization potentials for multiply charged ion species.

To improve the experimental results, a mass filter system with better mass resolution and higher ion transmission efficiency should be used. Also, much more sophisticated theoretical treatment could take into account the overlapping ionization processes. It is hoped that these work can be performed in the future.

REFERENCES

- 1. J. E. Campana, Int. J. Mass Spectrom. Ion Phys., 33, 101 (1980).
- 2. J. F. J. Todd, Dynamic Mass Spectrometry, Volume 5, edited by D. Price, Heyden & Son Ltd., 1978.
- 3. P. H. Dawson and N. R. Whetten, Dynamic Mass Spectrometry, Volume 2, edited by D. Price, Heyden & Son Ltd., 1972.
- 4. J. H. Batey, Vacuum, 37, No. 8/9, 659 (1987).
- 5. J. V. Seggern, et al., J. Vac. Sci. Technol., A2(4), 1516 (1984).
- 6. F. Watanabe and H. Ishimaru, J. Vac. Sci. Technol., A4(3), 1720 (1986).
- 7. M. F. Finlan, et al., Nucl. Instr. and Meth., 195, 447 (1982).
- 8. R. Dutil and P. Marmet, Int. J. Mass Spectrom. Ion Phys., 35, 371 (1980).
- 9. A. Hashizume and N. Wasada, Int. J. Mass Spectrom. Ion Phys., 36, 291 (1980).
- 10. P. H. Dawson (Ed.), Quadrupole Mass Spectrometry ans its Application, Elsevier, Amsterdam, 1976.
- 11. M. D. N. Lunney, Dynamics of Ions in Radio frequency Quadrupole Traps, Master Thesis, McGill University, Montreal, 1986.
- 12. S. L. Gulick, Ion Injection into Radio Frequency Quadrupole Field Devices, Master Thesis, McGill University, Montreal, 1986.
- 13. C. M. Moroney, Theory and Construction of a Quadrupole Mass Filter, Project Report, McGill University, Montreal, 1990.

- 14. F. A. White and G. M. Wood, Mass Spectrometry Applications in Science and Engineering, John Wiley & Sons, New York, 1986.
- 15. M. E. Rose and R. A. W. Johnstone, Mass Spectrometry for Chemists and Biochemists, Cambridge University, Cambridge, 1982.
- 16. B. S. Middleditch, Practical Mass Spectrometry, Plenum, New York, 1979.
- 17. T. Tamir, Math. Computations, 16, 77 (1962).
- 18. P. H. Dawson, J. Vac. Sci. Technol., A4(3), 1709 (1986).
- 19. W. E. Austin, et al, J. Vac. Sci. Technol., A5(4), 2631 (1987).
- 20. T. D. Mark and G. H. Dunn (Ed.), Electron Impact Ionization, Springer-Veclag, Wien New York, 1985.
- 21. R. H. Vought, Phys. Rev., 71, 93 (1947).
- 22. R. E. Fox, Advances in Mass Spectrometry, edited by J. D. Waldron, Pergamon Press Inc., New York, 1959.
- 23. R. E. March and R. J. Hughes, Quadrupole Storage Mass Spectrometry, John Wiley & Sons, New York, 1989.
- 24. A. E. Holme and W. J. Thatcher, Int. J. Mass Spectrom. Ion Phys., 10, 271 (1972/73).
- 25. A. E Holme, S. Sayyid and J. H. Leck, Int. J. Mass Spectrom. Ion Phys., 26, 191 (1978).
- 26. B. Hu and J. Qiu, J. Vac. Sci. Technol., A5(4), 2657 (1987).
- 27. H. F. Dylla and J. A. Jarrell, Rev. Sci. Instrum., 47, No. 3, 1976.
- 28. F. M. Mao and J. H. Leck, Vacuum, 37, No. 8/9, 669 (1987).
- 29. C. E. Moore, Atomic Energy Levels, Natl. Bur. Stds. Circ. 467, Dec. 1971.

- 30. R. D. Levin, Ionization Potential and Appearance Potential Measurements. Natl. Bur. Stds., Washington DC, Oct. 1982.
- 31. F. H. Field and J. L. Frankin, Electron Impact Phenomena and the Properties of Gaseous Ions, Academic Press Inc., New York, 1957.
- 32. H. M. Rosenstock, Int. J. Mass Spectrom. Ion Phys., 20, 139 (1976).
- 33. E. P. Wigner, Phys. Rev., 73, 1002 (1948).
- 34. S. Geltman, Phys. Rev., 102, 1767 (1956).
- 35. G. H. Wannier, Phys. Rev., 90, 817 (1953).
- 36. G. H. Wannier, Phys. Rev., 100, 1180 (1955).
- 37. H. Klar and W Schlecht, J. Phys., **B9**, 1699 (1976).
- 38. P. Grujic, J. Phys., **B15**, 1913 (1982).
- 39. P. Grujic, J. Phys., **B16**, 2567 (1983).
- 40. P. Grujic, Phys. Lett., 96A, 233 (1983).
- 41. H. R. Koslowski, J. Binder, B. A. Huber and K. Wiesemann, J. Phys., **B20**, 5903 (1987).
- 42. L. P. Johnson and J. D. Morrison, Int. J. Mass Spectrom. Ion Phys., 18, 355 (1975).
- 43. A. Russek, Phys. Rev., 132, 246 (1963).
- 44. H. Lebius, et al., Journal de Physique, Col. C1, Sup. au nº 1, Tome 50, jan. 1989.
- 45. P. Marchand, C. Paquet and P. Marmet, Phys. Rev., 180, No. 1, 123 (1969).
- 46. H. M. Rosenstock, et al., J. Phys. Chem. Ref. Data, 6, Suppl. 1, 5 (1977).
- 47. P. A. Redhead, Can. J. Phys., 45, 1791 (1967).

- 48. F. A. Stuber, J. Chem. Phys., 42, 2639 (1965).
- 49. E. Krishnakumar and S. K. Srivastava, J. Phys., B21, 1055 (1988).
- 50. H. Lebius, et al., J. Phys., B22, 83 (1989).
- 51. A. R. P. Rau, Phys. Rev., A4, 207 (1971).
- 52. J. W. McGowan and E. M. Clark, Phys. Rev., 167, 43 (1968).
- 53. W. Bleekney, Phys. Rev., 36, 1303 (1930).
- 54. R. E. Fox, J. Chem. Phys., 33, 200 (1960).